SAINT PETERSBURG STATE UNIVERSITY

As manuscript

Tambovtsev Ivan Mikhailovich

LOCALIZED CHIRAL STATES IN LIQUID CRYSTALS AND MAGNETICS

Scientific Specialty 1.3.3. Theoretical Physics

Dissertation for the degree of
Candidate of Physical and Mathematical Sciences

Translation from Russian

Scientific Advisor:
Doctor of Physical and Mathematical Sciences, Professor
Uzdin Valery Moiseevich

Saint Petersburg
2024

Contents

Introduction

The development of modern technologies for storing, processing, and displaying information has raised a number of fundamental challenges related to reducing characteristic sizes, achieving fast dynamics, and implementing energy-efficient control of localized magnetic and liquid crystal (LC) structures. The issue of the stability of such structures against thermal fluctuations and random perturbations must be addressed simultaneously with the ability to control and manage the corresponding states through small, directed influences. Nanoscale magnetic systems are now being considered as candidates for information bits in racetrack memory systems [1]. Localized structures in LCs can serve as miniature, controllable, and reconfigurable optical elements. They can be used for beam shaping [2], creating unique diffraction gratings, and in the case of stable structures, for storing and processing information encoded in the director configuration [3]. Therefore, the problem of describing the stability and dynamics of localized magnetic and LC structures, in addition to its importance for fundamental science, is highly relevant for practical applications.

As the characteristic size of a structure decreases, ensuring its stability against random external influences becomes increasingly difficult. One possible approach involves the use of so-called topological protection. For a number of localized non-collinear structures in magnets and liquid crystals (LCs), topological indices can be introduced, which are integer values preserved under continuous changes in magnetization or LC director. In this case, continuous transformations do not alter the topological indices, making such structures stable against transitions that would require a change in these indices. Corresponding localized non-collinear structures in magnets or LCs, which have an index different from the homogeneous state, are called "topological solitons." These include quasi-two-dimensional skyrmions, anti-skyrmions, merons, three-dimensional torons, hopfions, heliknotons, and others [4,5]. For magnetic moments defined on the nodes of a discrete crystal lattice, strict topo-

logical protection does not apply. However, it should manifest indirectly through the magnitude of activation barriers that must be overcome for a magnetic transition, and in the limiting case, when the lattice constant is small compared to the size of the structure, the corresponding lifetimes of the states should significantly increase [6, 7].

Chiral interactions are often responsible for the formation and stability of topological solitons. This applies both to magnetic structures, where such interactions arise due to spin-orbit contributions to the energy, and to cholesteric-type LC systems. In the approximation of equal Frank modules, the energy functional of cholesteric LCs resembles that of micromagnetic systems with Dzyaloshinskii-Moriya interaction. In both magnets and LCs, the same localized topological structures can form. For magnets, one of the key questions is the estimation of the lifetimes of topological solitons, which serve as a quantitative measure of their stability. This estimation can be made within the framework of transition state theory, which involves constructing the energy surface of the system and finding the paths with minimal energy barriers between local minima corresponding to different states [8]. In the harmonic approximation, the lifetimes of states at arbitrary temperatures can be obtained based on the shape of the energy surface at the initial minimum and near the saddle point on the energy surface [9].

For LC systems, the issue of the temperature dependence of the stability of localized states is less significant. These structures exist within a relatively narrow temperature range, and it can be assumed that their stability does not change within this range. Nevertheless, the analysis of the system's energy surface remains a useful approach for describing equilibrium properties and transitions between topologically distinct states [10]. In LCs, the transformation of the energy surface, the emergence and disappearance of new minima leading to transitions between states, are usually induced by external factors such as electromagnetic fields and the anchoring conditions of the LC director on the surface [11].

The aim of this work is to study chiral topological states in liquid crystals (LCs) and magnetic films of a given thickness based on the analysis of the multidimensional energy surface of the system. The influence of external fields, finite sample sizes, and boundary conditions on the spatial structure of locally stable states will be demonstrated, and the most likely transition scenarios between them will be calculated. Calculations of topological solitons existing in different parts of the phase diagram of cholesteric liquid crystal films or chiral magnets will be presented.

Structure and Scope of the Work. The dissertation consists of an introduction, 4 chapters, a conclusion, acknowledgments, a bibliography, and an appendix. The work comprises 121 pages and 38 figures. The bibliography includes 82 references.

Reliability of the results obtained in the dissertation is determined, on the one hand, by the fact that the theoretical approach is based on well-established principles of statistical physics, and the calculations were performed using modern algorithms and methods of computational physics. On the other hand, the results obtained are in agreement with theoretical calculations made within alternative models and with the results of precision experiments. For example, the method proposed in this work for determining the Frank modules for lanthanide-based mesogens was tested on the liquid crystal 5CB, for which the Frank modules are already known. The two-dimensional structures such as the tilted spiral are close to the experimental results presented in [12]. All the main results of the dissertation research have been published in leading peer-reviewed journals and were presented at scientific seminars of St. Petersburg State University, ITMO University, and at Russian and international conferences.

Presentation of the Work

The results of the work were presented at the following conferences:

1. International Conference

"Mathematical challenge of quantum transport in nanosystems – Pierre Duclos

workshop", St. Petersburg, September 14-16, 2020.

2. All-Russian Conference "Science SPbU - 2020", St. Petersburg, December 24, 2020.

3. International Conference

   "Promising element base of micro- and nanoelectronics using modern achievements of theoretical physics", Moscow, April 20-23, 2020.

4. International Conference

   "15th European Conference on Liquid Crystals", Wrocław, June 30 - July 5, 2019.

List of publications related to the dissertation topic

1. Tambovtsev, I.M. Topological structures in chiral media: Effects of confined geometry / I. M. Tambovtsev, A. O. Leonov, I.S. Lobanov, et al. // Physical Review B. — 2022. — Vol. 105, no. 3. — P. 034701. **WOS, Scopus**.

2. Tambovtcev, I.M. Hysteresis and Fr'eedericksz thresholds for twisted states in chiral nematic liquid crystals: Minimum-energy path approach / S.S. Tenishchev, I.M. Tambovtcev, A.D. Kiselev, V.M. Uzdin // Journal of Molecular Liquids — 2021. — Vol. 325 — P. 115242. **WOS, Scopus**.

3. Tambovtsev, I.M. METHOD FOR CALCULATING FRANK MODULES OF A LIQUID CRYSTALLINE COMPLEX BASED ON ERBIUM / I.M. Tambovtsev, L.A. Dobrun, A.P. Kovshik, E.V. Aksenova, E.I. Ryumtsev // Bulletin of MGOU. — 2020. — Vol. 3. — P. 6–12. **VAK**.

4. Tambovtcev, I.M. Magnetic field-induced macroscopic alignment of liquid-crystalline lanthanide complexes / E.V. Aksenova, L.A. Dobrun, A.P. Kovshik, E.I.

Ryumtsev, I.M. Tambovtcev // Crystals — 2019. — Vol. 9, no. 10 — P. 499. **WOS, Scopus**.

5. Tambovtcev, I.M. Stability of in-plane and out-of-plane chiral skyrmions in epitaxial MnSi (111)/Si (111) thin films: Surface twists versus easy-plane anisotropy / A.O. Leonov, I.M. Tambovtcev, I.S. Lobanov, V.M. Uzdin, // Physical Review B — 2020. — Vol. 102, no. 17 — P. 174415. **WOS, Scopus**.

Russian and International Grants Supporting the Research conducted in the dissertation:

1. "Study of topological magnetic textures as a basis for artificial neural networks," Russian Science Foundation (RSF), 19-42-06302.

2. "The nature of topological stability in chiral magnetic and liquid crystal systems," Foundation for the Advancement of Theoretical Physics and Mathematics "BASIS," 19-1-1-12-2.

Main Scientific Results

1. An analysis of the phase diagram of thin films of cholesteric liquid crystal has been conducted. The primary and metastable states of the system have been determined for various values of boundary anchoring and external magnetic fields (work [13], pp. 4 – 8, personal contribution 80%).

2. It has been shown how localized chiral structures in magnetic and liquid crystal films, including torons, fingers, and skyrmion tubes, transform under the influence of external magnetic and electric fields (work [13], pp. 8 – 10, personal contribution 90%).

3. An analysis of the phase diagram of thin films of cubic helimagnets has been carried out. It has been demonstrated that the stabilization of skyrmion and

spiral structures depends on anisotropy and the orientation of the magnetic field (work [14], pp. 1 – 7, personal contribution 60%).

4. Transitions between locally stable spiral states with different numbers of spiral turns have been identified in thin films of cholesteric liquid crystals and layered magnetic nanosystems. The barriers of these transitions depend on the tension and anchoring parameters with the substrates (work [15], pp. 1 – 3, personal contribution 60%).

5. A method for determining the Frank modules for lanthanide-based liquid crystals has been developed, enabling the calculation of their elastic properties based on the analysis of the influence of the magnetic field (work [16], p. 3, personal contribution 80%).

6. Hysteresis effects have been identified during the change of external electric field in cholesteric liquid crystals, allowing for improved control of such systems in practical applications (work [15], pp. 5 – 7, personal contribution 60%).

7. Studies of liquid crystal complexes based on gadolinium and erbium have been conducted. Frank modules for these complexes have been determined, taking into account their high anisotropy in magnetic susceptibility (work [16], pp. 8 – 12, personal contribution 80%, work [17], p. 3, personal contribution 90%, and [18], pp. 4 – 5, personal contribution 90%).

Theses to be Defended.

1. Using the developed method for processing and interpreting experimental data on the dielectric permittivity dependence of a liquid crystal cell based on lanthanide mesogen on an applied magnetic field in directions parallel and perpendicular to the cell plates, it is possible to determine the Frank modules of the liquid crystal, which is challenging to achieve by other methods.

2. In thin films of cholesteric liquid crystals (and layered magnetic nanosystems similar to them) with planar anchoring at the surface, transitions between locally stable spiral states with different numbers of spiral turns are possible. Depending on the applied voltage and the anchoring parameters with the substrates, the energy barrier between these states can significantly change. In cholesteric liquid crystals, a hysteresis of the energy barrier change is observed depending on the history of the applied voltage changes.

3. In thin films of cholesteric liquid crystals (and layered magnetic nanosystems similar to them) with planar anchoring at the surface, various equilibrium and metastable phases can form, including spiral and conical structures, tilted spiral states, as well as localized topological solitons such as skyrmion tubes, torons, and fingers. Topological solitons can integrate into larger domain patterns and transform from one type to another as external conditions and system parameters change.

4. In thin films of cubic helimagnets, the stabilization of skyrmion and spiral structures depends on the anisotropy and orientation of the magnetic field. For in-plane magnetic fields, skyrmions exhibit elliptical instability and exist only in a narrow parameter range. When the field is oriented perpendicular to the surface, various magnetic structures can exist, including skyrmion tubes with axes perpendicular to the plane, at significantly larger film thicknesses.

Chapter 1

Energy Surfaces of Chiral Magnetic and Liquid Crystal Systems

Cholesteric liquid crystals (LCs) and magnetic systems with Dzyaloshinskii-Moriya interactions can be described by formally identical free energy functionals. This leads to the possibility of forming the same localized chiral states in both systems, some of which belong to "topological solitons." In this chapter, the free energy functional of such systems is introduced, and the procedure for constructing the corresponding multidimensional energy surfaces, which can be used to determine the energy barriers between states, is described. At the end of the chapter, a method for determining the Frank modules for LC complexes based on lanthanides is presented, using experimental data on the dependence of the dielectric permittivity on an external electric field.

1.1. Free Energy of Chiral Magnets and Liquid Crystals

Magnetic and liquid crystal structures are configurations of magnetic moments or directors in condensed (solid or liquid) media with long-range order. The order parameter in magnets is a vector field of magnetization. Magnetic moments can be localized at the nodes of a crystal lattice or distributed continuously throughout the volume of the system. In a liquid crystal, the ordered state is determined by the distribution of the director field, which defines the orientation of molecules relative to a preferred direction. One can speak of a continuous distribution of the director within the medium or a director associated with individual elements into which the entire volume of the liquid crystal is divided. Although magnetically ordered and liquid crystalline states have many fundamental differences, the ordered structures

that arise in both are often similar, and formally, in a certain approximation, they can be described by the same energy functionals. Both in LCs and in magnets, interactions can exist that lead to the formation of chiral states and topological solitons, which are of great interest for both fundamental physics and applications.

Let us first consider a continuum model describing a thin film of a chiral magnet or LC. The energy functional can be written as:

$$F[\mathbf{m}] = \int_V \left(\mathcal{A}(\nabla \mathbf{m}(\mathbf{r}))^2 - \mathcal{D}\, \mathbf{m}(\mathbf{r}) \cdot [\nabla \times \mathbf{m}(\mathbf{r})] - \mathcal{K}_b (\mathbf{m}(\mathbf{r}) \cdot \mathbf{z})^2 \right) dV - \\ - \mathcal{K}_s \int_S (\mathbf{m}(\mathbf{r}) \cdot \mathbf{z})^2 \, dS, \quad (1.1)$$

where the first integral is taken over the system volume V, and the second is over the bounding surface S, which consists of two planes normal to the z axis. The order parameter is defined by the vector field $\mathbf{m}(\mathbf{r})$. For magnetic systems, $\mathbf{m}(\mathbf{r})$ is a unit vector along the magnetization at point $\mathbf{r}$, and for liquid crystals, it is the LC director at that point. $\mathbf{z}$ is a unit vector along the anisotropy axis, which is assumed to be orthogonal to the surfaces S.

In magnetic systems, the first term in ((1.1)) describes the exchange interaction with the exchange stiffness parameter $\mathcal{A}$, which is assumed to be uniform throughout the film. The second term corresponds to the chiral Dzyaloshinskii-Moriya interaction (DMI), with its intensity determined by the parameter $\mathcal{D}$. The third term in the first integral and the second integral represent magnetic anisotropy energies. The anisotropy values inside the film, $\mathcal{K}_b$, and at its boundaries, $\mathcal{K}_s$, may differ: $\mathcal{K}_s \neq \mathcal{K}_b$.

For liquid crystal systems, the values of $\mathcal{A}$ and the constant of chiral interaction $\mathcal{D}$ are expressed in terms of the Frank elastic moduli [19] K_1, K_2, K_3. In the one-constant approximation, where all the elastic constants are assumed equal,

$K_1 = K_2 = K_3 = K$: $\mathcal{A} = K/2$ and $\mathcal{D} = Kq_0$, where q_0 is the wave number of the helical state in an unbounded liquid crystal. In liquid crystal systems, $\mathcal{K}_b$ plays the role of the interaction constant with an external magnetic field, while $\mathcal{K}_s$ is determined by the anchoring at the surface of the liquid crystal cell (anchoring conditions are assumed to be homeotropic unless otherwise specified).

To determine the ground state and metastable states corresponding to the local energy minima, it is convenient to transition from the continuous model to a discrete lattice model on a three-dimensional cubic grid of size $N_x \times N_y \times N_z$ and use the method of nonlinear conjugate gradients in Cartesian coordinates with constraints that fix the unit length of the vectors $\mathbf{m}$ at the lattice nodes.

If the system under consideration is a thin film, periodic boundary conditions are applied in the xy plane.

The model obtained through discretization corresponds to a generalized Heisenberg model, commonly used in magnetism theory, particularly for describing topological magnetic structures [20].

It is important to note that, at the nanoscale, magnetic moments are often localized at atoms in the nodes of the crystallographic lattice. In this case, the continuous model can be considered as the limiting case of a real discrete model when the lattice constant is small compared to the characteristic sizes of the magnetic structures. It is also worth mentioning that structures with different crystal lattices and exchange interaction parameters may correspond to the same continuum model.

The energy for the discrete lattice model can be written as:

$$E[\mathbf{S}] = -\sum_{\langle i,j \rangle} \left(J\mathbf{S}_i \cdot \mathbf{S}_j + \mathbf{D}_{i,j} \cdot [\mathbf{S}_i \times \mathbf{S}_j] \right) - \sum_i K_i (S_i^z)^2, \tag{1.2}$$

where $\mathbf{S}_i \equiv \mathbf{m}_i$ are unit vectors along the magnetic moment or the LC director at node i. For brevity, we will sometimes refer to these vectors as spins. The summation $\langle i, j \rangle$ in (1.2) is performed over the nearest neighbor nodes. The param-

eter J represents the Heisenberg exchange interaction, and the vector $\mathbf{D}_{i,j}$ is the Dzyaloshinskii-Moriya vector, describing the symmetric and antisymmetric interactions between spins localized at nodes i and j. We assume that the vector $\mathbf{D}_{i,j}$ is directed along the segment connecting nodes i and j, which facilitates the stabilization of spiral structures and Bloch-type domain walls. The magnitude of the vector $|\mathbf{D}_{i,j}| = D$ and the parameter J are assumed to be the same for all neighboring node pairs.

The last term in the energy expression ((1.2)) represents the contribution of uniaxial magnetic anisotropy with the anisotropy axis normal to the substrate planes (the z axis). In the systems considered below, it is assumed that the values of the anisotropy parameter K_i at the boundaries and for the internal nodes of the sample may differ. We will assume that the anisotropy parameter contains a bulk contribution K^b, which is the same for all lattice layers, but at the boundary, a surface contribution K^s is added. Thus, $K_i = K^b$ for the internal layers, and $K_i = K^b + K^s$ for the boundary layers.

In magnetic systems, an additional Zeeman interaction term is added to the bulk part of (1.1) to describe the interaction with an external magnetic field:

$$w_Z = -\mu_0 M \mathbf{m}(\mathbf{r}) \cdot \mathbf{H}, \tag{1.3}$$

where μ_0 is the vacuum permeability, M is the magnetization, $\mathbf{m}(\mathbf{r})$ is the unit vector of magnetization at position $\mathbf{r}$, and $\mathbf{H}$ is the external magnetic field.

There is a correspondence between the parameters of the continuous model ((1.1)) and the discrete lattice model ((1.2)) [7]. For a simple cubic lattice, this correspondence is as follows:

$$2a\mathcal{A} = J, \quad a^2\mathcal{D} = D, \quad a^3\mathcal{K}(\mathbf{r}) = K_i, \tag{1.4}$$

where a is the lattice constant.

For liquid crystals, the parameters of the discrete model J and D are determined by the Frank elastic moduli, with the expression ((1.2)) derived in the one-constant approximation. The anisotropy parameters are related to external fields and the interaction of the LC with the boundaries of the cell in which it is placed.

"Easy-plane" anisotropy in the bulk corresponds to the interaction energy of an LC with negative magnetic susceptibility anisotropy $\Delta\chi < 0$ in the presence of a magnetic field applied perpendicular to the plates of the cell.

"Easy-axis" anisotropy in the bulk describes the interaction with a magnetic field in an LC with $\Delta\chi > 0$.

Surface anisotropy $\mathcal{K}_s > 0$ corresponds to homeotropic anchoring conditions, while $\mathcal{K}_s < 0$ corresponds to planar anchoring. Additionally, the rigid anchoring model should be mentioned, where the orientation of the liquid crystal at the surface is fixed according to the initial alignment.

The chirality of the LC is characterized by the equilibrium pitch of the helical structure, which represents the ground state in an unbounded sample, p_0, with the corresponding wave number given by $q_0 = 2\pi/p_0 = \arctan(D/J)$. In a nematic liquid crystal, $D = 0$, and thus $p_0 = 0$.

The formulation of the energy functional allows not only the determination of the system's equilibrium state but also its dynamics. In the case of magnetic systems, the dynamics are governed by the Landau-Lifshitz-Gilbert equation, where the effective magnetic field acting on each magnetic moment is determined by the derivative of the energy with respect to the magnetization.

For liquid crystal systems, when describing the dynamics of localized structures, such as in the case of an inhomogeneous distribution of D in the system, the one-constant approximation may be insufficient. In such cases, a more general expression for the energy of the LC must be used. Let us explore this topic in more detail.

The Frank free energy density ω of a liquid crystal, assuming different values for the Frank moduli, is given by [19]:

$$\omega[\mathbf{n}] = \frac{1}{2}\Big[K_1(\operatorname{div}\mathbf{n})^2 + K_2(\mathbf{n}\cdot\operatorname{rot}\mathbf{n} + q_0)^2 + \\ + K_3(\mathbf{n}\times\operatorname{rot}\mathbf{n})^2 - \Delta\chi(\mathbf{n}\cdot\mathbf{H})^2\Big], \quad (1.5)$$

where K_1, K_2, K_3 are the Frank elastic constants, $q_0 = 2\pi/P$ is the wave number, P is the pitch of the cholesteric helix, $\mathbf{H}$ is the external magnetic field, and $\Delta\chi = \chi_\parallel - \chi_\perp$ is the difference in magnetic susceptibility along the direction of the director $\mathbf{n}$ ($\chi_\parallel$) and perpendicular to it ($\chi_\perp$) [21]. Typical values of the Frank constants [22–26] are:

$$0.5 < \frac{K_2}{K_1} < 0.8, \quad 0.5 < \frac{K_3}{K_1} < 3.0. \quad (1.6)$$

The wave number q_0 (a function of position $\mathbf{x}$) can be positive, negative, or zero. A positive q_0 corresponds to a right-handed helix, and a negative q_0 corresponds to a left-handed helix. The value of $\Delta\chi$ depends on the properties of the liquid crystal and can be either positive or negative.

As noted earlier, the expression for the energy density can be significantly simplified if all the Frank constants are equal. Let us explicitly write the energy density corresponding to this approximation, considering the other contributions in (1.3) as perturbations. For this, we use the identity:

$$(\operatorname{div}\mathbf{n})^2 + (\operatorname{rot}\mathbf{n})^2 + \nabla\cdot((\nabla\cdot\mathbf{n})\mathbf{n} - \mathbf{n}(\nabla\cdot\mathbf{n})) = (\operatorname{grad}\mathbf{n})^2. \quad (1.7)$$

The last term on the left describes surface interaction, and under rigid boundary conditions, it does not contribute to the result due to the divergence theorem. The remaining part, written with explicit indices and denoting $n_{i,j} = \partial n_i/\partial x_j$, takes the

following form:

$$\left(\sum_i n_{i,i}\right)^2 + \sum_i \left(\sum_{j,k} \varepsilon_{ijk} n_{k,j}\right)^2 = \sum_{i,j} (n_{i,j})^2. \tag{1.8}$$

We use another identity, which represents the Pythagorean theorem for $\operatorname{rot}\mathbf{n}$:

$$\mathbf{n}^2(\nabla \times \mathbf{n})^2 = (\mathbf{n} \cdot (\nabla \times \mathbf{n}))^2 + (\mathbf{n} \times (\nabla \times \mathbf{n}))^2, \tag{1.9}$$

where the terms on the right-hand side are the squares of the projections of $\operatorname{rot}\mathbf{n}$ onto the direction of $\mathbf{n}(x)$ and the orthogonal direction $\mathbf{n}(x)^\perp$. Taking into account (1.8), (1.9), and the condition $\mathbf{n}(x)^2 = 1$, we can write the energy density as follows:

$$\omega = \frac{1}{2}\Big[K_1(\nabla\mathbf{n})^2 - K_1(\nabla \times \mathbf{n})^2 + K_2(\mathbf{n} \cdot \nabla \times \mathbf{n})^2 + 2K_2 q_0(\mathbf{n} \cdot \nabla \times \mathbf{n}) + K_2 q_0^2 + \\ + K_3(\nabla \times \mathbf{n})^2 - K_3(\mathbf{n} \cdot (\nabla \times \mathbf{n}))^2 - \Delta\chi(\mathbf{n} \cdot \mathbf{H})^2\Big]. \tag{1.10}$$

The constant term can be omitted. By collecting like terms, the energy density can be written as:

$$\omega = \frac{1}{2}\Big[K_1(\nabla\mathbf{n})^2 + (K_3 - K_1)(\nabla \times \mathbf{n})^2 + (K_2 - K_3)(\mathbf{n} \cdot \nabla \times \mathbf{n})^2 + \\ + 2K_2 q_0(\mathbf{n} \cdot \nabla \times \mathbf{n}) - \Delta\chi(\mathbf{n} \cdot \mathbf{H})^2\Big]. \tag{1.11}$$

The last term appears if the LC is in an external magnetic field [27, 28]. The chiral ordering is governed by the penultimate term containing q_0. The second and third terms in (1.11) are nonzero only if the corresponding Frank constants are different. It is worth noting that all terms in the energy density expression, except for $(\mathbf{n}\cdot\nabla\times\mathbf{n})^2$, are quadratic in $\mathbf{n}$. If one is primarily interested in processes like the compression of cholesteric fingers [29–31], which are controlled by the K_3 parameter, the expression

can be simplified by setting $K_2 = K_3$, making the energy quadratic. Moreover, if $K_1 = K_3$ (the one-constant approximation), the expression reduces to the integrand in equation (1.1).

1.2. Ground and Metastable States of Magnetic and Liquid Crystal Systems in Thin Films

Locally stable states correspond to minima on the energy surface of the system. These can be determined numerically, starting from an arbitrary magnetic configuration by shifting the state on the energy surface in the direction opposite to the energy gradient. The surface may contain several local minima with different energy levels, each corresponding to its own magnetic configuration. In this case, a non-collinear magnetic structure may be localized in a small region of space or may occupy the entire sample.

For magnetic systems, in a sufficiently strong magnetic field, the ground state corresponds to a homogeneous ferromagnetic state. In the presence of antisymmetric exchange interaction, the energy minimum in weak magnetic fields corresponds to a spiral magnetic structure. In addition to these delocalized states, compact metastable structures can form, corresponding to shallower minima on the energy surface.

In confined samples, boundary conditions can significantly influence the shape of the energy surface. Periodic boundary conditions allow the modeling of structures that repeat in space in one, two, or three directions. However, the spatial size of such structures does not exceed the size of the simulated cell.

At the boundaries of the considered computational domain, the system's parameters may change, allowing the description of interfaces and free surfaces in magnetic systems or interactions with the surface of the cell in liquid crystals. In the latter case, for boundary layers, an additional term is usually introduced into

the energy functional, representing uniaxial anisotropy [13].

As an example, let us consider a structure whose ground state is non-collinear and inhomogeneous in one direction, but for which the corresponding minimum on the energy surface can be found analytically.

Let us examine a magnet or liquid crystal in a half-infinite space $z \geqslant 0$ with rigid boundary conditions at the surface, where the magnetic moments or director are fixed orthogonally to the plane of the boundary. The z-axis is chosen in this same direction. We seek an equilibrium configuration that is homogeneous in the xy plane.

The direction of each magnetic moment (or director) can be described by the polar and azimuthal angles $\theta(z)$ and $\phi(z)$, where θ is the angle between the magnetic moment (or director) and the z-axis.

$$n_x = \cos\varphi \sin\theta, \quad n_y = \sin\varphi \sin\theta, \quad n_z = \cos\theta. \tag{1.12}$$

For a state that is homogeneous in the xy plane, we have $\mathbf{n} = \mathbf{n}(z)$, and the free energy functional is given by

$$F = S \int\limits_{\mathbb{R}_+} \omega \, dz, \tag{1.13}$$

where $\mathbb{R}_+$ denotes the region $z \geqslant 0$, and S is the area of the cell.

In this case, according to (1.11), the free energy can be rewritten as:

$$F = \frac{V}{2} K_2 q_0^2 + \frac{S}{2} \int\limits_{\mathbb{R}_+} \left[A(\theta)(\theta')^2 + B(\theta)(\varphi')^2 - C(\theta)\varphi' + D(\theta) \right] dz, \tag{1.14}$$

where

$$A(\theta) = K_1 \sin^2\theta + K_3 \cos^2\theta, \tag{1.15}$$

$$B(\theta) = \sin^2\theta(K_2 \sin^2\theta + K_3 \cos^2\theta), \tag{1.16}$$

$$C(\theta) = q_0 K_2 \sin^2\theta, \tag{1.17}$$

$$D(\theta) = -\Delta\chi H^2 \cos^2\theta. \tag{1.18}$$

The first variation of the free energy can be written as:

$$\delta F = \frac{S}{2}\int\limits_{\mathbb{R}_+} \Big(A'(\theta')^2\delta\theta + 2A\theta''\delta\theta + B'\varphi'^2\delta\varphi + 2B\varphi'(\delta\varphi)' - \\ - 2C'\varphi'\delta\theta - 2C(\delta\varphi)' + D'\delta\theta \Big) dz. \tag{1.19}$$

By setting the coefficients of $\delta\theta$ and $\delta\varphi$ under the integral to zero, we obtain two equations:

$$A'\theta'^2 + 2A\theta'' = B'\varphi'^2 - 2C'\varphi' + D', \tag{1.20}$$

$$\frac{d}{dz}(B\varphi' - C) = 0. \tag{1.21}$$

In the one-constant approximation $K = K_1 = K_2 = K_3$:

$$2K\theta'' = 2K \sin\theta\cos\theta\varphi'^2 - 4q_0 K \sin\theta\cos\theta\varphi' - \Delta\chi H^2 \sin\theta\cos\theta \tag{1.22}$$

and

$$\frac{d}{dz}(K\sin^2\theta(\varphi' - q_0)) = 0. \tag{1.23}$$

Let us write the boundary conditions for θ:

$$\theta(z)\big|_{z=0} = 0, \qquad \theta(z)\big|_{z=\infty} = \frac{\pi}{2}. \tag{1.24}$$

In the absence of an external field, from equation (1.23), we get:

$$\varphi = q_0 z + \varphi_0, \tag{1.25}$$

and the solution for θ:

$$\theta(z) = 2\arctan\exp(q_0 z) - \frac{\pi}{2}, \tag{1.26}$$

where φ_0 is the value of the angle φ at $z = 0$. This solution describes a helical ordering of magnetic moments (or director orientations), in which, as z increases, the moments uniformly rotate around the z-axis, with their projection onto this axis gradually decreasing.

In thin films of finite thickness with a finite value of surface anisotropy K^s, the solution can be obtained numerically. Figure 3.2 shows the dependence of the z-projection (the distance from the lower boundary along the normal) and the corresponding configuration.

The solutions discussed will be used later when analyzing the phase diagram of a magnet with anisotropic exchange or a cholesteric LC in thin films or LC cells.

1.3. Determination of Frank Moduli for Liquid Crystals Containing Lanthanide Complexes

For the theoretical description of liquid crystal properties based on the energy functional , knowledge of the Frank moduli is necessary. Therefore, determining these values from experimental data is crucial for developing a quantitative theory. The most common methods for determining Frank moduli involve studying the dependence of the refractive index on the orientation of molecules in liquid crystals using techniques such as Raman and dynamic light scattering spectroscopy [19].

Determining these parameters for liquid crystals containing lanthanide complexes with organic ligands (lanthanidomesogens) requires a different, non-optical approach. The liquid crystalline phase temperature for such compounds is around 130°C, and they are not transparent in the optical range. The anchoring of these compounds in liquid crystal cells is such that the angle between the normal to the surface and the director differs from 0 or $\pi/2$.

Interest in these materials stems from their combination of highly efficient luminescence with abnormally large anisotropy in magnetic susceptibility $\Delta\chi = \chi_{\parallel} - \chi_{\perp}$, where $\chi_{\parallel}$ and $\chi_{\perp}$ are the components of magnetic susceptibility along and perpendicular to the preferential orientation axis of the molecules [21]. These properties of nematic lanthanidomesogens allow the creation of optical media with linearly polarized luminescence, suitable for use in optoelectronic devices controlled by magnetic and electric fields [32]. Some liquid crystal complexes based on gadolinium are also used as contrast agents in magnetic resonance imaging (MRI) [33].

For the effective practical use of lanthanidomesogens, it is crucial to understand the orientational processes occurring in the material under the influence of magnetic and electric fields. Below, we will discuss the determination of Frank moduli in such systems, taking into account the spatial inhomogeneity of the orientation of lanthanidomesogens.

To address this task, one can use a method based on measuring the dielectric permittivity of a cell as a function of the external fields applied to it. This experiment was conducted for LC molecules $Gd(CPDk_{3-5})_3Bpy_{17-17}$ and $Er(DDk_{3-5})_3Bpy_{17-1}$. These LC complexes exhibit a large anisotropy in magnetic susceptibility: $\Delta\chi = 1805{\cdot}10^{-6}$ cm^3/mol for the gadolinium-based complex and $\Delta\chi = 9894{\cdot}10^{-6}$ cm^3/mol for the erbium-based complex [34,35]. The positive sign of $\Delta\chi$ was determined based on an analysis of optical birefringence in LCs in a magnetic field (Cotton-Mouton effect) [36]. The chemical structures of the LC molecules are shown in Figures 1.1 (a, b).

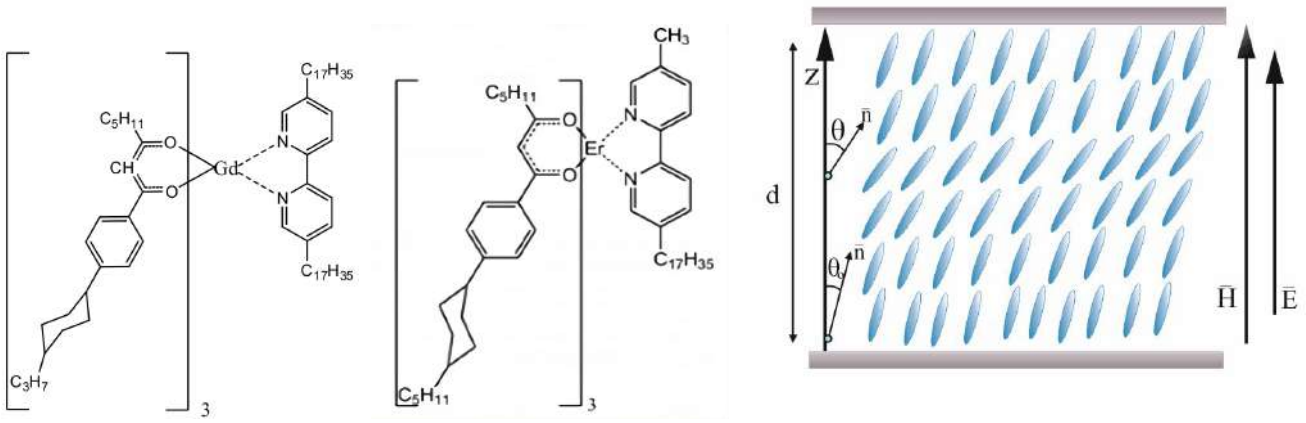

(*а*) (*б*) (*в*)

Figure 1.1. Chemical structure of the liquid crystal based on a) gadolinium and b) erbium. c) Orientation of nematic liquid crystal molecules in a sample cell with the magnetic field applied perpendicular to the cell plates. Here **n**) is the director, θ is the angle between the director and the z-axis, and θ_0 is the pre-tilt angle of the director at the surfaces of the cell.

To analyze the orientation of the liquid crystal in a magnetic field, the capacitance of a capacitor filled with the liquid crystal was measured as a function of the external magnetic field applied both in-plane and perpendicular to the cell [37, 38]. Figure 1.1 (c) schematically shows the director distribution inside the capacitor, which is formed by the surfaces of the cell. The change in the orientation of the LC director in external fields is accompanied by a change in the cell's capacitance. Measuring the capacitance of the liquid crystal cell under various magnetic field strengths

H provides information about the orientation of the director in the sample. The maximum magnetic field strength during the measurements reached 7500 Oe.

Measuring the capacitance allows the effective value of the dielectric permittivity $\bar{\varepsilon}$, characterizing the material inside the capacitor, to be obtained:

$$\bar{\varepsilon} = \frac{C \cdot d}{S}, \tag{1.27}$$

where: C is the capacitance of the capacitor, d is the distance between the plates, and S is the area of the capacitor plates.

The experimentally obtained dependencies of the effective dielectric permittivities on the magnetic field applied in-plane and perpendicular to the plane are shown in Figure 1.2. Figure (a) corresponds to the LC complex with gadolinium, (b) to the erbium complex, and (c) to 5CB. It is noteworthy that the dielectric permittivity behavior in response to the applied magnetic field varies among the substances: for the field applied in-plane for the 5CB sample, $\bar{\varepsilon}$ decreases as the field increases, while for the gadolinium-based LC it increases. For both types of LC, the magnetic susceptibility anisotropy $\Delta\chi > 0$, and the director tends to align along the magnetic field at high field strengths. The effective dielectric permittivity of the LC approaches $\varepsilon_\perp$, as the director aligns perpendicularly to the electric field. For 5CB, $\varepsilon_\parallel > \varepsilon_\perp$, so $\bar{\varepsilon}$ decreases. For the gadolinium and erbium complexes, $\Delta\varepsilon = \varepsilon_\parallel - \varepsilon_\perp > 0$, so $\bar{\varepsilon}$ increases.

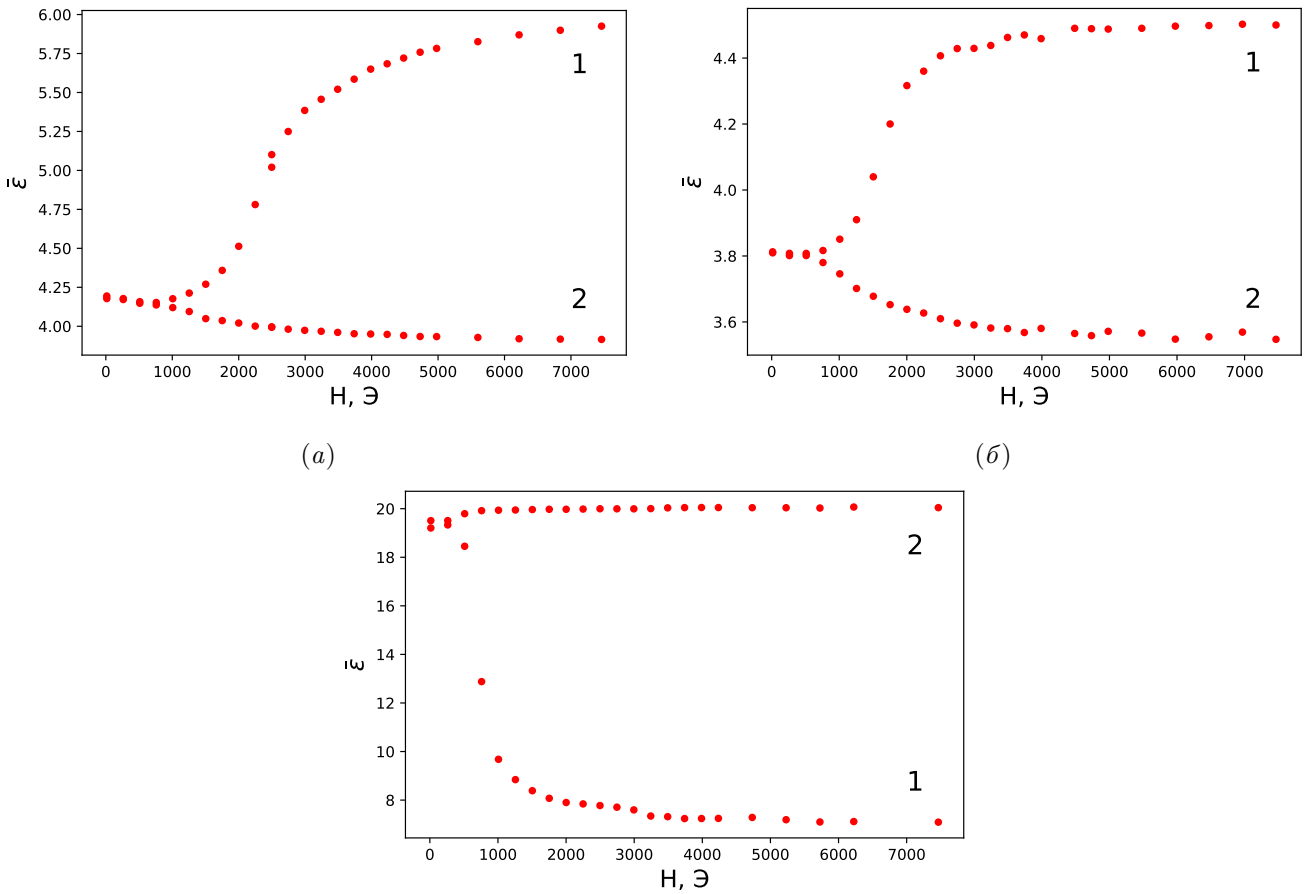

Figure 1.2. a) Dependence of the effective dielectric permittivity $\bar{\varepsilon}$ of the cell with the gadolinium-based LC complex (a), erbium-based complex (b), and 5CB (c) on the magnetic field strength for the field applied along the capacitor plates (1) and perpendicular to the plates (2).

The change in the orientation of the director in the systems under consideration is associated with the Fréedericksz transition. The classical Fréedericksz effect has been studied for a long time and is well described both theoretically and experimentally [19, 39, 40]. Recently, there has been significant interest in studying this effect in more complex systems and under more intricate conditions, where the system is inhomogeneous and its properties can change under the influence of external fields [41–48].

When theoretically describing the Fréedericksz transition, careful analysis of boundary conditions is required. In the literature, the anchoring of molecules to the aligning surface is most commonly described using the Rapini–Popoular potential

of Gaussian type [49]. In nematic liquid crystals with finite anchoring energy, the Fréedericksz transition is continuous, and the orientation of the director above the threshold changes throughout the volume, including at the boundary [39].

There is a significant difference between the description of the Fréedericksz effect in electric and magnetic fields. This difference is related, in particular, to the fact that the electric field inside a liquid crystal with an inhomogeneous director distribution is not spatially uniform [27,28]. The details of this issue and the choice of the thermodynamic potential that describes the system in the presence of an external field are discussed in the works [50–53].

Let us consider the change in the orientation of the director under strong and weak anchoring conditions in the presence of external electric and magnetic fields. To determine the type of equilibrium director configuration, we use a method based on the minimization of the free energy of the liquid crystal. In this case, the Frank elastic constants will be treated as unknown parameters to be obtained by minimizing the free energy functional.

To theoretically describe the results shown in Figure 1.2, we will use the expression (1.11) for the free energy. We assume that the orientation of the nematic liquid crystal molecules in the plane perpendicular to the cell boundaries and parallel to the electric field $\mathbf{E}$ and the aligning magnetic field $\mathbf{H}$ (in the case of their parallel alignment) corresponds to the configuration shown in Figure 1.1 (b).

Assuming that the director depends only on the coordinate z, we obtain the expression for the free energy:

$$F = S \int_0^d dz\, \omega(z), \tag{1.28}$$

where S is the area of the upper and lower surfaces of the cell, which act as the capacitor plates.

For calculating the dielectric permittivity of a material with $\Delta\chi > 0$, the

director orientation can be described by a single angle θ [39]. Then, expressing the contribution of the electric field through the voltage applied to the capacitor plates [54], we obtain the following expression for the energy density:

$$\omega = \frac{1}{2}\Bigg[\left(K_1 \sin^2\theta + K_3 \cos^2\theta\right)(\theta')^2 \mp \Delta\chi H^2 \sin^2\theta - \frac{\Delta\varepsilon}{4\pi} \frac{U^2 d}{\int\limits_0^d (\varepsilon_\perp + \Delta\varepsilon \cos^2\theta)^{-1}\, dz} \cos^2\theta \Bigg]. \tag{1.29}$$

The upper sign corresponds to $\mathbf{H} \perp \mathbf{E}$, while the lower sign corresponds to $\mathbf{H} \parallel \mathbf{E}$.

At a given magnetic field strength, the orientation of the liquid crystal director corresponds to the minimum of the free energy (1.28). For a given director orientation, the effective dielectric permittivity of the sample $\bar{\varepsilon}$ is determined through the angle θ:

$$\bar{\varepsilon} = \frac{d}{\int\limits_0^d (\varepsilon_\perp + \Delta\varepsilon \cos^2\theta)^{-1}\, dz}. \tag{1.30}$$

To determine the director orientation $\theta(z)$, we will minimize the free energy functional (1.28) with additional boundary conditions. In the following, we assume that the boundary conditions at the surfaces $z = 0$ and $z = d$ are identical. Two models will be considered: the strong anchoring model

$$\theta(0) = \theta(d) = \theta_0, \tag{1.31}$$

and the weak anchoring model, which reduces to adding the following term to the

energy density (1.29):

$$\omega_{sur} = k \, \sin^2(\theta - \theta_0), \tag{1.32}$$

where the coupling constant k and the angle θ_0 are phenomenological parameters. It should be noted that models with $\theta_0 = 0$ do not fit the experimental data. The weak anchoring model corresponds to the Rapini-Papoular model [49].

For the case $\mathbf{H} \perp \mathbf{E}$ under weak boundary conditions, we have

$$\theta[H \to \infty] \to \frac{\pi}{2} \Longrightarrow \bar{\varepsilon}[H \to \infty] \to \varepsilon_\perp. \tag{1.33}$$

In the case $H \to 0$, we get:

$$\theta[H \to 0] \to \theta_0. \tag{1.34}$$

Thus, using equation (1.30), we can derive

$$\bar{\varepsilon}[H \to 0] \to \varepsilon_\perp + \Delta\varepsilon \cos^2 \theta_0. \tag{1.35}$$

This, in turn, leads to a condition for θ_0:

$$\theta_0 = \theta(0) = \theta(d) = \arccos\left(\sqrt{\frac{\bar{\varepsilon}_0 - \varepsilon_\perp}{\Delta\varepsilon}}\right), \tag{1.36}$$

where $\bar{\varepsilon}_0$ is the dielectric permittivity of the sample in the absence of electric and magnetic fields. If the electric field strength is below the Fréedericksz threshold, the pre-tilt angle θ_0 can be estimated from measurements at $H = 0$.

The director profile, i.e., the dependence of $\theta(z)$, is determined by minimizing the free energy functional (1.28) with boundary conditions (1.31) or (1.32). This allows us to determine the dependence of $\bar{\varepsilon}$ on H for given parameters K_1 and K_3. This problem was solved numerically for various values of K_1 and K_3 corresponding to the magnetic field strengths used in the experiment.

The first step in the numerical procedure for calculating the Frank moduli was to determine the dependence of θ on z for the magnetic fields at which the capacitance of the LC cell was measured. It is worth noting that direct numerical minimization, unlike the solution using the Euler-Lagrange equation [40], does not require calculating the second derivative, which can demand additional precision in the calculations.

The second step was to find the values of the Frank moduli K_1 and K_3 that provide a theoretical dependence of $\bar{\varepsilon}$ on H that best matches the experimental data. For this, the least squares (LS) method was used, which involves minimizing the following quantity:

$$LS(K_1, K_3) = \frac{1}{|\Delta\varepsilon|N}\sqrt{\sum(\bar{\varepsilon}_{exp} - \bar{\varepsilon}(K_1, K_3))^2}, \tag{1.37}$$

where the summation is performed over all N points of the experimental dependence $\bar{\varepsilon}_{exp}$ on the field H, and $\bar{\varepsilon}(K_1, K_3)$ is the numerically calculated value for this field. According to the minimum criterion (1.37), the values of K_1 and K_3 that give the smallest root-mean-square deviation from the experimental data are found.

Thus, two minimization problems are solved sequentially: one for finding $\theta(z)$, and the second for determining the moduli K_1 and K_3 that provide results closest to the experimental data.

Figure 1.3 shows the calculated dependence of $\theta(\bar{z})$, where $\bar{z} = z/d$, for $K_1 = 2.5 \cdot 10^{-5}$ dyn and $K_3 = 1.7 \cdot 10^{-4}$ dyn for the gadolinium complex.

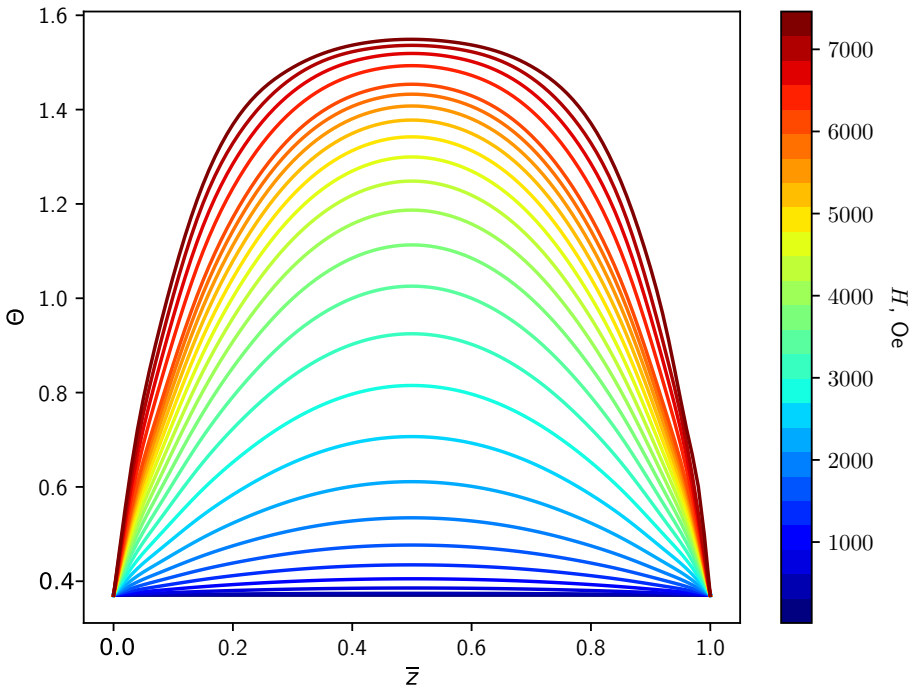

Figure 1.3. Profiles of the angle θ as a function of $\bar{z}$ for gadolinium-based LC complexes at various values of H, with $K_1 = 2.5 \cdot 10^{-5}$ dyn, $K_3 = 1.7 \cdot 10^{-4}$ dyn, $\theta_0 = 20.6°$.

Similar graphs were obtained for other values of the Frank moduli K_1 and K_3 for all substances.

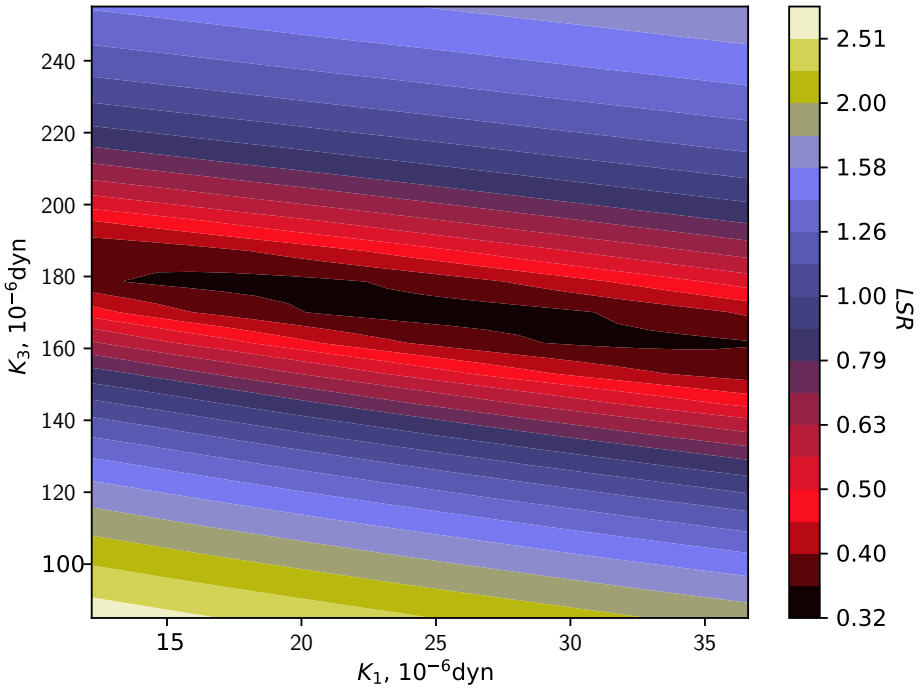

Figure 1.4. Map of the LS criterion for K_1 and K_3 for gadolinium-based LC complexes.

This allowed us to construct the map $LS(K_1, K_3)$ shown in Figure 1.4. This map was generated using 1681 evenly distributed points. The minimum was achieved at $K_1 = 2.5 \cdot 10^{-5}$ dyn and $K_3 = 1.7 \cdot 10^{-4}$ dyn, which correspond to the dependencies shown in Figure 1.3. Calculations were carried out for both strong and weak anchoring conditions (with various values of the coefficient k in equation (1.32)). The best agreement for lanthanidomesogens was achieved with strong boundary conditions.

To investigate the estimation error, the dependence $\bar{\varepsilon}(H)$ was calculated using equation (1.30) for the same set of magnetic fields H as in the experiment. The optimal values of the Frank moduli mentioned earlier, as well as $\theta_0 = 20.6°$, were used. Now, suppose that K_1 and K_3 for this dependence are unknown, and we aim to find them using the LS minimization criterion (1.37). The K_1, K_3 map obtained is shown in Figure 1.5. It can be seen that the minimum is found at the expected values of K_1 and K_3. For the erbium-based complex, the minimum was achieved at

$K_1 = 7 \cdot 10^{-6}$ dyn and $K_3 = 6.7 \cdot 10^{-4}$ dyn.

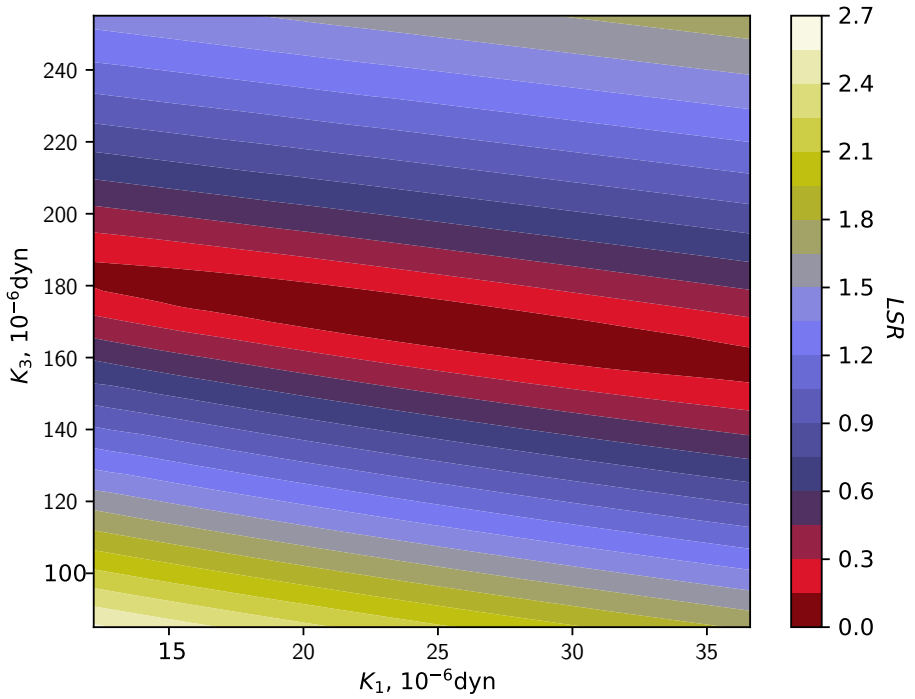

Figure 1.5. Map of the LS criterion for K_1 and K_3 for the test dependence of the gadolinium-based LC complex.

Figure 1.6 shows the relationship between the pre-tilt angle θ_0 and the angle of the long axis of the ellipses at a constant LS value for the gadolinium complex.

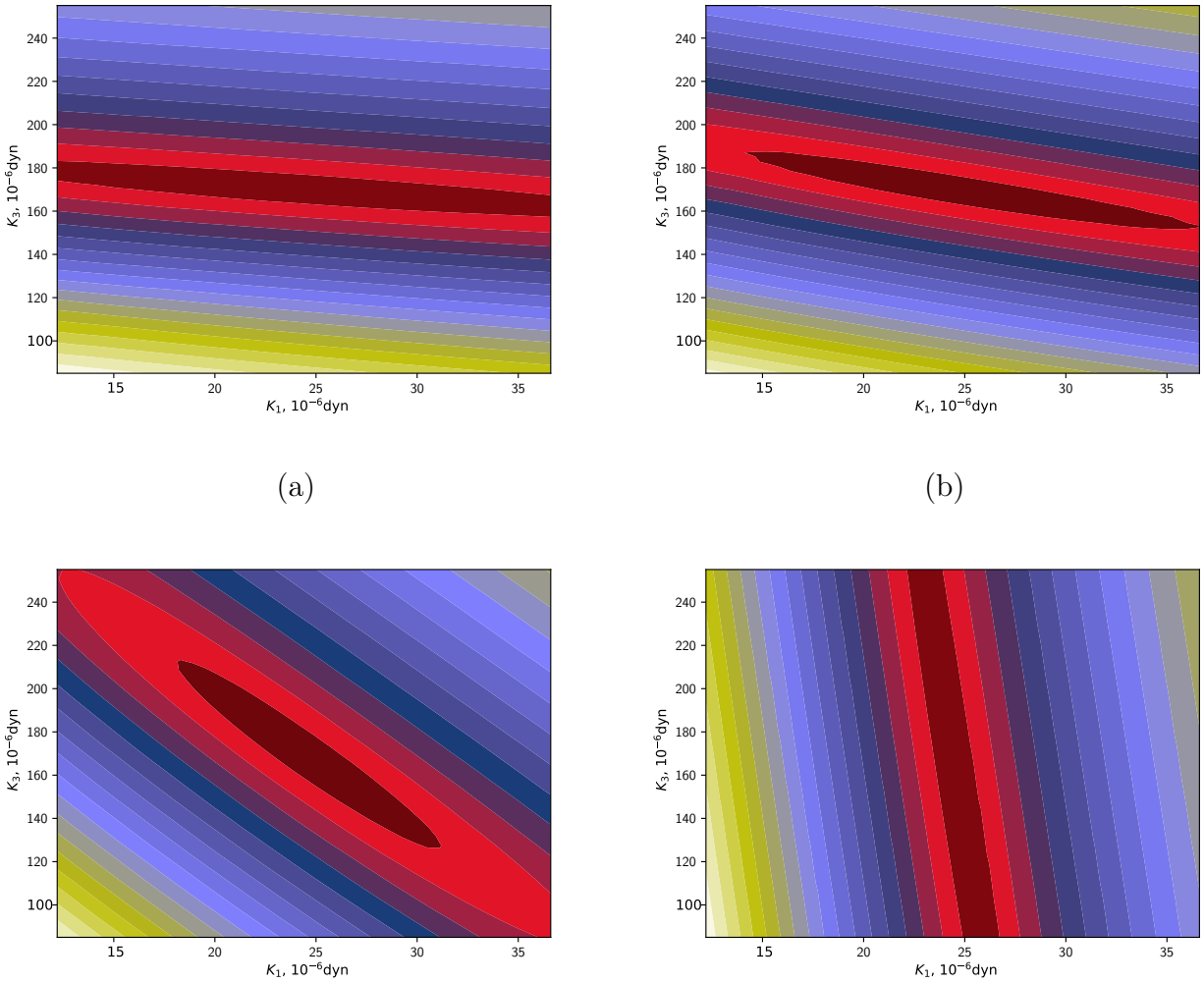

Figure 1.6. Map of the LS criterion for K_1 and K_3 for the test dependence of the gadolinium-based LC complex for different values of θ_0: 10° (a), 30° (b), 60° (c), 80° (d). Here, the values of K_1 and K_3 are plotted on the axes using the same scale as in Figure 1.5.

Another way to perform a self-check is to repeat the same measurements for a liquid crystal with known Frank moduli. The well-studied LC 5CB was used as such a system. The results of the 5CB measurements for the same cell and geometry are shown in Figure 1.7.

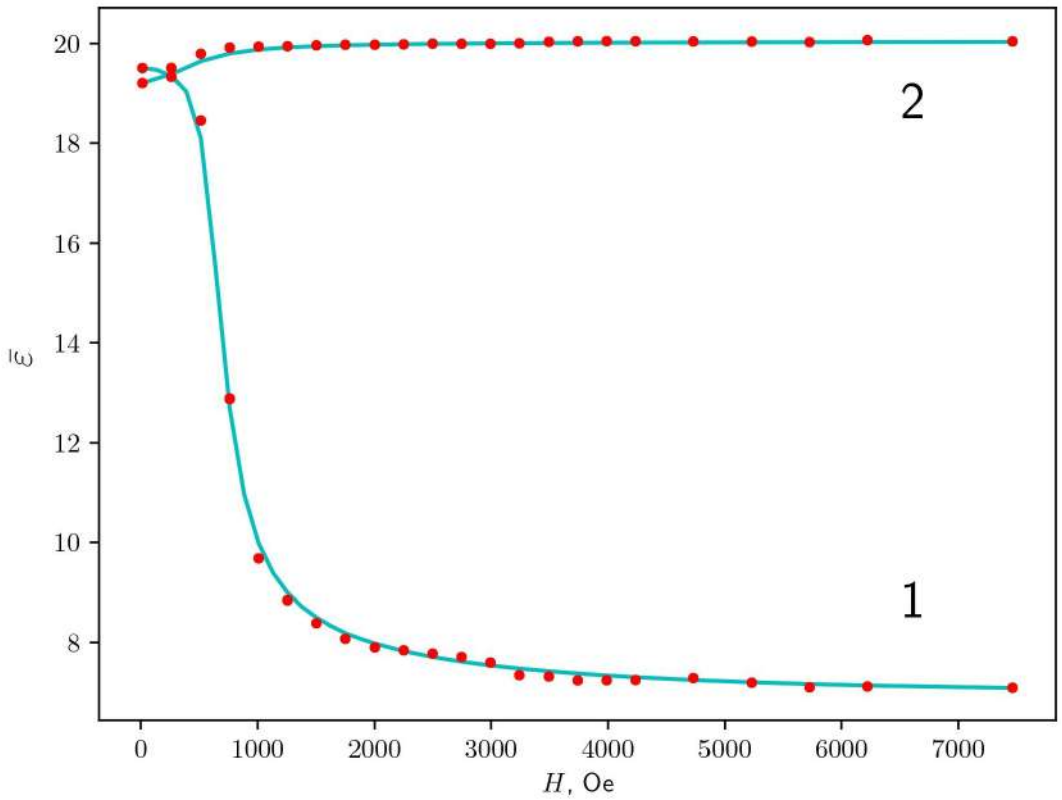

Figure 1.7. Dependence of $\bar{\varepsilon}$ on H for 5CB: experimental (points) and theoretical (solid line). The line and points marked with 1 correspond to the case $\mathbf{H} \perp \mathbf{E}$. The line and points marked with 2 correspond to the case $\mathbf{H} \parallel \mathbf{E}$.

The numerical procedure for finding the Frank moduli described earlier was applied. The corresponding LS map for K_1 and K_3 for 5CB is shown in Figure 1.8.

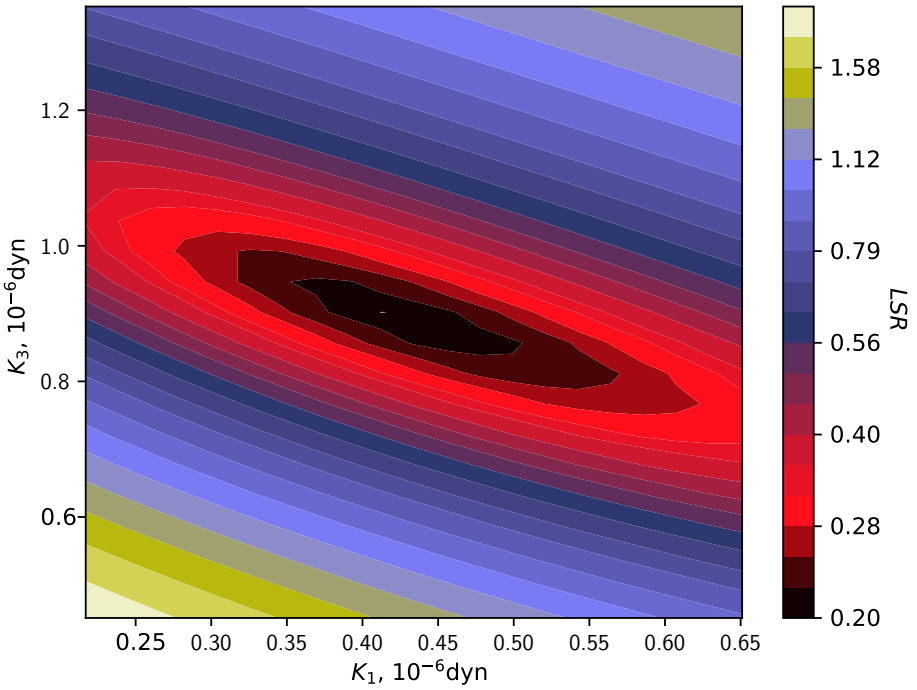

Figure 1.8. Map of the LS criterion for K_1 and K_3 for the LC 5CB.

The map shows a minimum at $K_1 = (0.4 \pm 0.2) \cdot 10^{-6}$ dyn and $K_3 = (0.8 \pm 0.1) \cdot 10^{-6}$ dyn. Comparing these results with the known values for 5CB [22–25] ($K_1 = 0.62 \cdot 10^{-6}$ dyn and $K_3 = 0.82 \cdot 10^{-6}$ dyn), we observe a good match for K_3 and a satisfactory match for K_1. The solid lines in Figure 1.7 were calculated based on the values of K_1 and K_3 obtained from the LS minimization map. The experimental data show good agreement with the calculated results.

Thus, the presented method allows the determination of Frank moduli for liquid crystals containing gadolinium complexes. A comparison of the experimental and theoretical values is shown in Figure 1.9. The solid lines correspond to the calculations based on the values of K_1 and K_3 obtained from the LS minimization map (Figure 1.4). The experimental data show good agreement with the calculated results. The Frank moduli for $Gd(CPDk_{3-5})_3Bpy_{17-17}$ were determined as $K_1 = (2.5 \pm 2) \cdot 10^{-5}$ dyn, $K_3 = (1.7 \pm 0.3) \cdot 10^{-4}$ dyn, and for $Er(DDk_{3-5})_3Bpy_{17-1}$ as $K_1 = (7 \pm 6) \cdot 10^{-6}$ dyn, $K_3 = (6.7 \pm 0.5) \cdot 10^{-4}$ dyn.

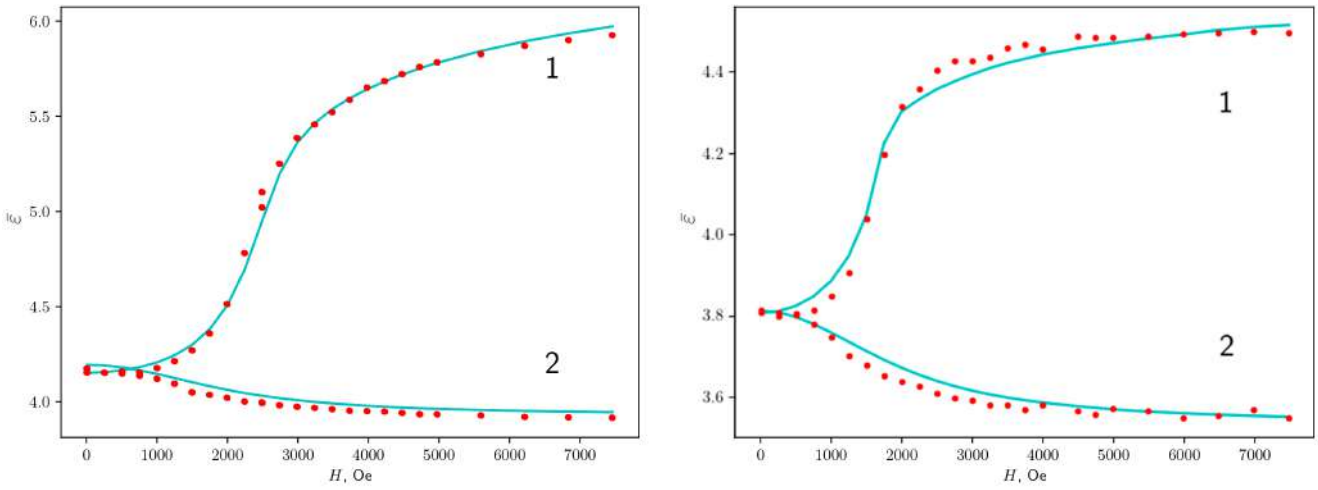

(*а*) (*б*)

Figure 1.9. Dependence of $\bar{\varepsilon}$ on H for gadolinium (a) and erbium (b) LC complexes: experimental (points) and theoretical (solid line). The line and points marked with 1 correspond to the case $\mathbf{H} \perp \mathbf{E}$. The line and points marked with 2 correspond to the case $\mathbf{H} \parallel \mathbf{E}$.

Conclusions for Chapter 1. The energy surfaces of cholesteric LCs in the one-constant approximation for the Frank moduli coincide with those of magnets with Dzyaloshinskii-Moriya interaction when the parameters of the models are appropriately chosen. This should lead to the formation of similar equilibrium non-collinear structures in these systems. In the general case, the energy surface of LCs is determined by their Frank moduli. A method for determining these moduli based on the dependence of the effective dielectric permittivity of LCs on the longitudinal and transverse magnetic fields relative to the plane of the LC cell has been proposed.

Chapter 2

Transitions between Locally Stable States in Chiral Systems

Defining the energy surface of magnetic and liquid crystal systems allows determining the ground and metastable states, which correspond to local energy minima. If there are several such minima, spontaneous transitions between states may occur due to thermal fluctuations and random external influences. This leads to a finite lifetime of the states, which, within the harmonic approximation of transition state theory, follows the Arrhenius law. To find the energy barrier between locally stable states and the pre-exponential factor in the Arrhenius law, a path with the minimal energy difference between the states is constructed. The maximum along the path determines the saddle point on the energy surface. The activation energy equals the difference in energies at the saddle point and the initial state. The pre-exponential factor depends on the shape of the energy surface at these points. If some parameters of the system change adiabatically slowly, we can talk about the evolution of the energy surface and the positions of the locally stable states caused by these changes. This chapter will consider such processes when the shape of the energy surface evolves with changes in the external electric field. In liquid crystals, this can lead to transitions between states with different director configurations, known as the Freedericksz effect. Cholesteric liquid crystals (CLC) in cells of different thicknesses will be studied.

2.1. Energy Surface and Locally Stable Spiral States in CLC Films of Different Thicknesses

Consider a thin CLC cell of thickness L, in which the liquid crystal is placed between two parallel bounding plates: $z = -L/2$ (bottom substrate) and $z = L/2$ (top substrate). The anchoring conditions on the substrates are planar, with a preferred orientation of the molecules on the bottom (top) plate determined by the easy axis vector $\hat{\mathbf{e}}_-$ ($\hat{\mathbf{e}}_+$)

$$\hat{\mathbf{e}}_\pm = \cos\psi_\pm\,\hat{\mathbf{e}}_\mathbf{x} + \sin\psi_\pm\,\hat{\mathbf{e}}_\mathbf{y}. \tag{2.1}$$

Here, hats are placed over unit vectors.

We write the free energy of the CLC, including both the bulk contribution F_b and the surface contribution F_s, associated with the anchoring energy on the substrates $W_\nu(\mathbf{n})$:

$$\begin{aligned} F[\mathbf{n},\mathbf{E}] &= F_b[\mathbf{n},\mathbf{E}] + F_s[\mathbf{n}], \\ F_s[\mathbf{n}] &= \sum_{\nu=\pm}\int_{z=\nu L/2} W_\nu(\mathbf{n})\,\mathrm{d}s, \end{aligned} \tag{2.2}$$

where $\mathbf{E}$ is the electric field. The surface contribution to the free energy is given by the Rapini-Papoular potential [49]:

$$\begin{aligned} W_\nu(\mathbf{n}) = {} & \frac{W_\varphi^{(\nu)}}{2}\Big[1 - \big(\mathbf{n}\cdot\hat{\mathbf{e}}_\nu\big)^2\Big]_{z=\nu L/2} \\ & + \frac{W_\vartheta^{(\nu)} - W_\varphi^{(\nu)}}{2}\big(\mathbf{n}\cdot\hat{\mathbf{e}}_\mathbf{z}\big)^2\Big|_{z=\nu L/2}, \end{aligned} \tag{2.3}$$

where $W_\varphi^{(+)}$ ($W_\varphi^{(-)}$) and $W_\vartheta^{(+)}$ ($W_\vartheta^{(-)}$) are the surface energy densities associated with the deviation of the polar and azimuthal angles, defining the director's direction,

from the preferred direction on the top (bottom) substrate. In the considered case, the director of the CLC is more conveniently parameterized by the angles $\vartheta = \vartheta(z)$ and $\varphi = \varphi(z)$ as follows:

$$\mathbf{n} \equiv \mathbf{n}(\vartheta, \varphi) = \cos\vartheta(\cos\varphi\,\hat{\mathbf{e}}_{\mathbf{x}} + \sin\varphi\,\hat{\mathbf{e}}_{\mathbf{y}}) + \sin\vartheta\,\hat{\mathbf{e}}_{\mathbf{z}}, \tag{2.4}$$

This parameterization is analogous to ((1.12)) with the substitution $\vartheta = \pi/2 - \theta$. The surface potential ((2.3)) now takes the following form:

$$F_s[\mathbf{n}]/S = \sum_{\nu=\pm}\left[\frac{W_\varphi^{(\nu)}}{2}\cos^2\vartheta_\nu \sin^2(\varphi_\nu - \psi_\nu) + \frac{W_\vartheta^{(\nu)}}{2}\sin^2\vartheta_\nu\right], \tag{2.5}$$

where S is the area of the substrates; $\vartheta_\nu \equiv \vartheta(\nu L/2)$ and $\varphi_\nu \equiv \varphi(\nu L/2)$.

The bulk part of the free energy functional ((2.2)) represents the sum of the elastic energy $F_{\mathrm{el}}[\mathbf{n}]$, defined by equation ((1.3)), and the interaction energy of the electric field $\mathbf{E}$ with the CLC molecules, $F_{\mathrm{E}}[\mathbf{n}, \mathbf{E}]$:

$$F_b[\mathbf{n}, \mathbf{E}] = F_{\mathrm{el}}[\mathbf{n}] + F_{\mathrm{E}}[\mathbf{n}, \mathbf{E}] \tag{2.6}$$

After substituting the CLC director ((2.4)) we have:

$$F_{\mathrm{el}}[\mathbf{n}]/S = \frac{1}{2}\int_{-L/2}^{L/2}\left\{K_1(\vartheta)[\vartheta']^2 + K_2(\vartheta)\cos^2\vartheta\,[\varphi']^2 - 2C(\vartheta)\varphi' + K_2 q_0^2\right\}\mathrm{d}z, \tag{2.7}$$

$$K_i(\vartheta) = K_i\cos^2\vartheta + K_3\sin^2\vartheta,\ C(\vartheta) = q_0 K_2\cos^2\vartheta, \tag{2.8}$$

where the prime denotes a derivative with respect to z. This expression corresponds to equation ((1.29)) for a nematic LC with a cholesteric term from expression ((1.3)). Note that for a nematic LC, the Frank module K_2 does not contribute to the energy in the considered geometry. We will assume that the electric field is normal to the substrates $\mathbf{E} = E_z(z)\hat{\mathbf{e}}_{\mathbf{z}}$; $E_z(z) = -V'(z)$, where $V(z)$ is the electrostatic potential.

If the applied voltage $U = V(-L/2) - V(L/2)$ is fixed, the electrostatic part of the energy can be written as

$$F_{\mathrm{E}} = -\frac{1}{2}\int_V \big(\mathbf{E}\cdot\mathbf{D}\big)\mathrm{d}v, \tag{2.9}$$

where $\mathbf{D} = \boldsymbol{\varepsilon}\,\mathbf{E}$ is the electric displacement, and $\boldsymbol{\varepsilon}$ is the dielectric permittivity tensor. Now F_{E} takes the form of a nonlocal functional:

$$F_{\mathrm{E}}/S = -\frac{U^2}{2E[\vartheta]}, \quad E[\vartheta] = \int_{-L/2}^{L/2}\frac{\mathrm{d}z}{\varepsilon_{zz}(\vartheta)}, \tag{2.10}$$

where $\varepsilon_{zz}(\vartheta) = \varepsilon_\perp + \varepsilon_a \sin^2\vartheta$, $\varepsilon_a = \varepsilon_\parallel - \varepsilon_\perp$; $\varepsilon_\perp$ and $\varepsilon_\parallel$ are the dielectric constants defining the dielectric permittivity tensor $\boldsymbol{\varepsilon}$. This expression is analogous to the contribution of the electric field in formula ((1.29)).

Further, for numerical calculations, the Frank modules typical for the LC 5CB [23] are used: $K_1 = 4.5$ pN, $K_2 = 3.0$ pN, $K_3 = 6.0$ pN. The analysis is carried out for the case of a symmetric CLC cell with a thickness of $L = 5$ μm with $W_\varphi^{(\pm)} \equiv W_\varphi = 0.05$ mJ/m^2 and $\hat{\mathbf{e}}_\pm = \hat{\mathbf{e}}_\mathbf{x}$ ($\psi_\pm = 0$).

Consider the state of a homogeneous helix with the twist axis perpendicular to the substrate, known as the planar Grandjean structure. In it, the liquid crystal molecules are uniformly ordered in layers, but the orientation of the molecules changes from layer to layer.

$$\begin{aligned} &\mathbf{n}_0 \equiv \mathbf{n}(0, u(z)) = \cos u\,\hat{\mathbf{e}}_\mathbf{x} + \sin u\,\hat{\mathbf{e}}_\mathbf{y}, \\ &u(z) = qz + \varphi_0, \end{aligned} \tag{2.11}$$

where $q = 2\pi/P$ is the wavenumber, and P is the pitch of the helix. We write the variation of the director:

$$\mathbf{n}(\delta\vartheta, u(z) + \delta\varphi) \approx \mathbf{n}_0 + \delta\mathbf{n}_0,\ \delta\mathbf{n}_0 = \delta\varphi\,\mathbf{n}_1 + \delta\vartheta\,\mathbf{n}_2, \tag{2.12}$$

where the angles $\delta\varphi$ and $\delta\vartheta$ describe the in-plane and out-of-plane deviations of the director from the equilibrium state, respectively; the quantities $\mathbf{n}_1$ and $\mathbf{n}_2$ are given by

$$\mathbf{n}_1 = -\sin u(z)\,\hat{\mathbf{e}}_\mathbf{x} + \cos u(z)\,\hat{\mathbf{e}}_\mathbf{y}, \quad \mathbf{n}_2 = \hat{\mathbf{e}}_\mathbf{z}. \tag{2.13}$$

The free energy ((2.12)) can now be expanded to second-order terms in small deviations (fluctuations) of the director $\boldsymbol{\psi} = \begin{pmatrix} \delta\varphi \\ \delta\vartheta \end{pmatrix}$. The vector ψ thus describes small in-plane and out-of-plane fluctuations of the liquid crystal director orientation. These fluctuations are important for the analysis of the stability and dynamics of CLCs. The second variation of the free energy $F^{(2)}[\boldsymbol{\psi}]$ represents a bilinear functional that describes the energy of director fluctuations in the harmonic (Gaussian) approximation.

$$F[\mathbf{n}] \approx F[\mathbf{n}_0] + F^{(2)}[\boldsymbol{\psi}], \tag{2.14}$$

$$F^{(2)}[\boldsymbol{\psi}] = \int_V f_b^{(2)}[\boldsymbol{\psi}]\,\mathrm{d}v + \sum_{\nu=\pm}\int_{z=\nu L/2} W_\nu^{(2)}(\boldsymbol{\psi})\,\mathrm{d}s. \tag{2.15}$$

Let us restrict ourselves to the case of states that are homogeneous in the plane of the substrate. In this case, $\boldsymbol{\psi} \equiv \boldsymbol{\psi}(z)$, and the expression for the fluctuation energy per unit area is

$$2F^{(2)}[\boldsymbol{\psi}]/S = \int_{-L/2}^{L/2} \boldsymbol{\psi}^\dagger\,\tilde{K}\boldsymbol{\psi}\,\mathrm{d}z + \sum_{\nu=\pm} \boldsymbol{\psi}^\dagger\,\tilde{Q}^{(\nu)}\boldsymbol{\psi}\Big|_{z=\nu L/2}, \tag{2.16}$$

where the operators $\tilde{K}$ and $\tilde{Q}^{(\nu)}$ can be represented as follows:

$$\tilde{K} = \begin{pmatrix} -K_2\partial_z^2 & 0 \\ 0 & -K_1\partial_z^2 + q^2K_q - \varepsilon_a E^2 \end{pmatrix}, \tag{2.17}$$

$$\tilde{Q}^{(\nu)} = \nu \begin{pmatrix} K_2\partial_z & 0 \\ 0 & K_1\partial_z \end{pmatrix} + \begin{pmatrix} W_\varphi^{(\nu)} \cos 2u_\nu & 0 \\ 0 & W_\vartheta^{(\nu)} - W_\varphi^{(\nu)} \sin^2 u_\nu \end{pmatrix}, \tag{2.18}$$

$E = U/L$, $u_\nu = u(\nu L/2) - \psi_\nu$ K_q is the effective elastic constant:

$$K_q = K_3 - 2K_2(1 - q_0/q). \tag{2.19}$$

The spectrum of $\tilde{K}$ is calculated by solving the boundary value problem:

$$\hat{K}\boldsymbol{\psi}_\lambda = \lambda\boldsymbol{\psi}_\lambda, \tag{2.20}$$

$$\tilde{Q}^{(\nu)}\boldsymbol{\psi}_\lambda\Big|_{z=\nu L/2} = 0, \tag{2.21}$$

where λ ($\boldsymbol{\psi}_\lambda$) are the eigenvalues (eigenmodes) of the operator. From equations ((2.17)-(2. it is seen that the operators $\tilde{K}$ and $\tilde{Q}^{(\nu)}$ are diagonal, so the contributions of $\delta\varphi$ and $\delta\vartheta$ are independent. This allows in-plane and out-of-plane fluctuations to be considered independently.

The helical configuration ((2.11)) is locally stable if all the eigenvalues of the second variation operator are positive. For a symmetric CLC cell, the stability analysis concerning in-plane fluctuations was conducted in the work [55]. Different branches of metastable helical states were found, differing in the number of director half-turns, $k \in \mathbb{N}$. The corresponding twist parameter q satisfies the inequality $(k - 1/2)\pi < qL \equiv \beta < (k + 1/2)\pi$. It is related to the wavenumber q_0 in the infinite medium as follows:

$$q_0 L \equiv \beta_0 = \beta + (-1)^k w_\varphi \sin\beta, \quad w_\varphi \equiv \frac{W_\varphi L}{2K_2}. \tag{2.22}$$

The branches with $0 \le k \le 3$ and $w_\varphi \approx 41.67$ ($W_\varphi = 0.05$ mJ/m^2) are shown in Figure 2.1.

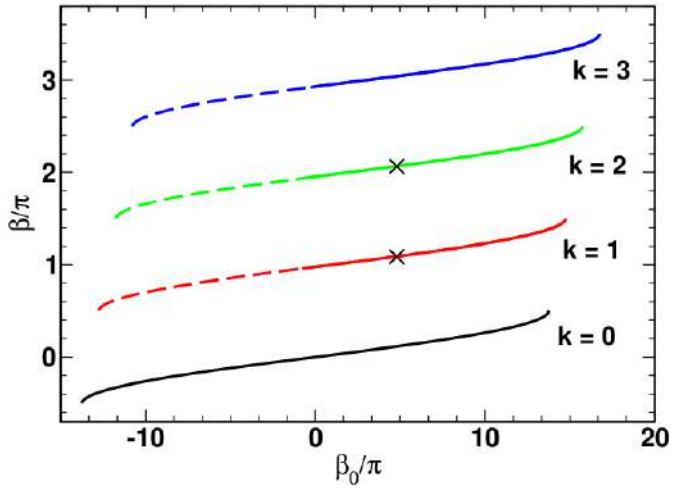

Figure 2.1. Twist parameter as a function of the parameter $\beta_0/\pi = q_0 L/\pi$ for different values of the number of half-turns, k. The dashed lines show states that are unstable with respect to out-of-plane disturbances. Crosses mark the values $\beta_0/\pi = 4.725$ on the curves $k = 1$ and $k = 2$.

Similarly, the stability of helical structures with respect to out-of-plane disturbances can be studied. For convenience, we switch from the variable λ to $K_1(2/L)^2\lambda$, denoting it by the same symbol, and write the eigenvalue problem ((2.20)-(2.21)) for ϑ as follows:

$$\left[\partial_\tau^2 + (-r_q + \varepsilon_a U^2/K_1)/4 + \lambda\right]\vartheta_\lambda(\tau) = 0, \tag{2.23}$$

$$\left[\pm\partial_\tau\vartheta_\lambda + w_\vartheta^{(\pm)}\vartheta_\lambda\right]_{\tau=\pm} = 0, \tag{2.24}$$

$$r_q = (qL)^2 K_q/K_1 = (r_3 - 2r_2)\beta^2 + 2r_2\beta_0\beta, \tag{2.25}$$

$$w_\vartheta^{(\nu)} \equiv \frac{(W_\vartheta^{(\nu)} - W_\varphi^{(\nu)}\sin^2 u_\nu)L}{2K_1},\ \beta = qL, \tag{2.26}$$

where $\tau \equiv 2z/L$, $r_i \equiv K_i/K_1$, and $\beta_0 = q_0 L$.

The stability condition $\lambda > 0$ can now be written as:

$$U < U_{\text{th}} = \sqrt{(4\lambda_{\min} + r_q)K_1/\varepsilon_a}, \tag{2.27}$$

where $\lambda_{\min}$ is the smallest eigenvalue of the problem ((2.23)), calculated at $r_q = 0$ and $U = 0$. The expression on the right side of the inequality ((2.27)) gives the critical Fredericksz transition voltage. Above this voltage, the applied electric field makes the vertically standing helix unstable with respect to out-of-plane disturbances of the director. When the polar anchoring is strong on both substrates, $W_\vartheta^{(\pm)} \to \infty$, a simple expression is obtained for the eigenvalue $\lambda_{\min}$:

$$\lambda_{\min} = (\kappa_{\min})^2 = \pi^2/4. \tag{2.28}$$

Otherwise, $\kappa_{\min}$ is less than $\pi/2$ and can be calculated as the root of the transcendental equation derived in the appendix of the work [55]

$$\tan 2\kappa_{\min} = \frac{\kappa_{\min}(w_\vartheta^{(+)} + w_\vartheta^{(-)})}{\kappa_{\min}^2 - w_\vartheta^{(+)} w_\vartheta^{(-)}}, \tag{2.29}$$

where $0 < \kappa_{\min} \leq \pi/2$.

The curves of the critical voltage as a function of the parameter β_0, representing the director twist angle in radians in a segment of this size in an infinite sample, are shown in Figure 2.2. The results obtained using the single-constant approximation (see Figure 2.2, *б*) can be compared with the critical field calculated for the elastic constants of the LC 5CB [23]: $K_1 = 4.5$ pN, $K_2 = 3.0$ pN, $K_3 = 6.0$ pN. It is seen that for non-zero k in both cases, the critical field (Fredericksz threshold) for each branch increases with the number of turns in the absence of boundaries q_0. For the branch with $k \geq 1$, the value of q_0 at which the threshold goes to zero determines the boundary point giving the smallest q_0 at which the formation of locally stable structures is possible. When q_0 is less than this value, helical states are unstable with respect to out-of-plane disturbances. In Figure 2.1, such structures are indicated by dashed lines. A comparison of the curves presented in Figure 2.2, *а* (5CB) and Figure 2.2, *б* (analytical analysis for the single-constant

approximation) also shows that elastic anisotropy strongly influences the dependence of the Fredericksz coefficient on q_0. The curves are calculated by formula ((2.27)) for the case of strong anchoring. The numerical estimate of the Fredericksz thresholds is in good agreement with theoretical predictions.

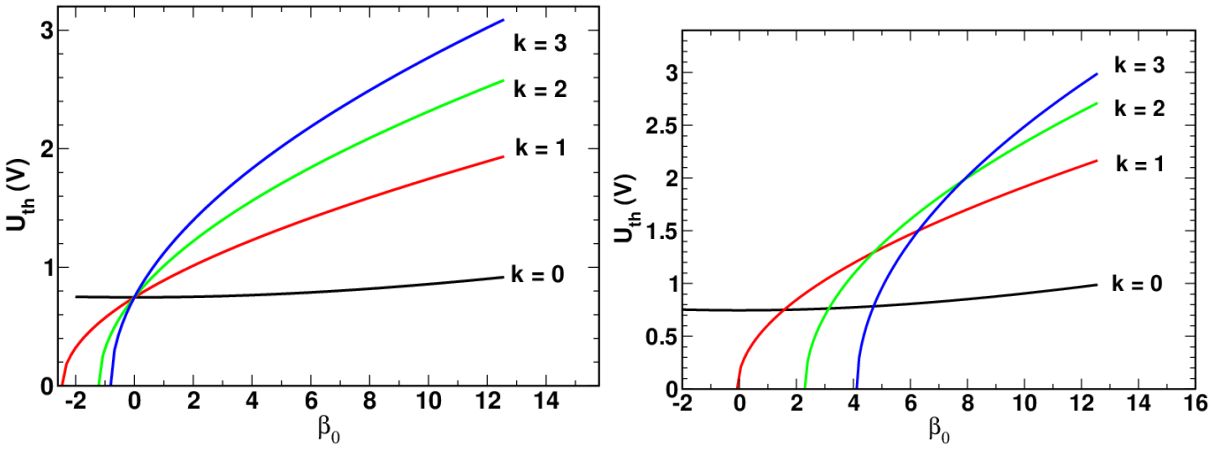

Figure 2.2. Critical Fredericksz transition voltage as a function of the parameter $\beta_0 = q_0 L$ for branches with half-turn numbers $0 \leq k \leq 3$ for (a) 5CB and (b) the single-constant approximation $K_i = K_1$

2.2. Paths with Minimal Energy Difference Between States with Different Numbers of Turns in Cholesteric Liquid Crystals

Let us consider the transition from a state with one half-turn ($k = 1$) to a state with two half-turns ($k = 2$), shown in Figure 2.1 at the parameter value $\beta_0 = 4.725$. The points on the curves corresponding to the states between which the transition occurs are marked with crosses. The equilibrium configurations of the CLC depend on the applied electric field, as the field affects the orientation of the director. This dependence can be obtained by minimizing the free energy functional of the system, including both bulk ((2.6)) and surface contributions ((2.3)), ((2.5)). The Euler-Lagrange equations determine the equilibrium director configurations,

taking into account the boundary conditions ((2.21)), ((2.24)).

Of particular interest is the Fredericksz effect, which occurs at certain values of the applied electric field when the CLC director begins to deviate from the plane parallel to the cell boundaries. This leads to a change in the system's energy and can either facilitate or hinder transitions between helical states with different numbers of half-turns.

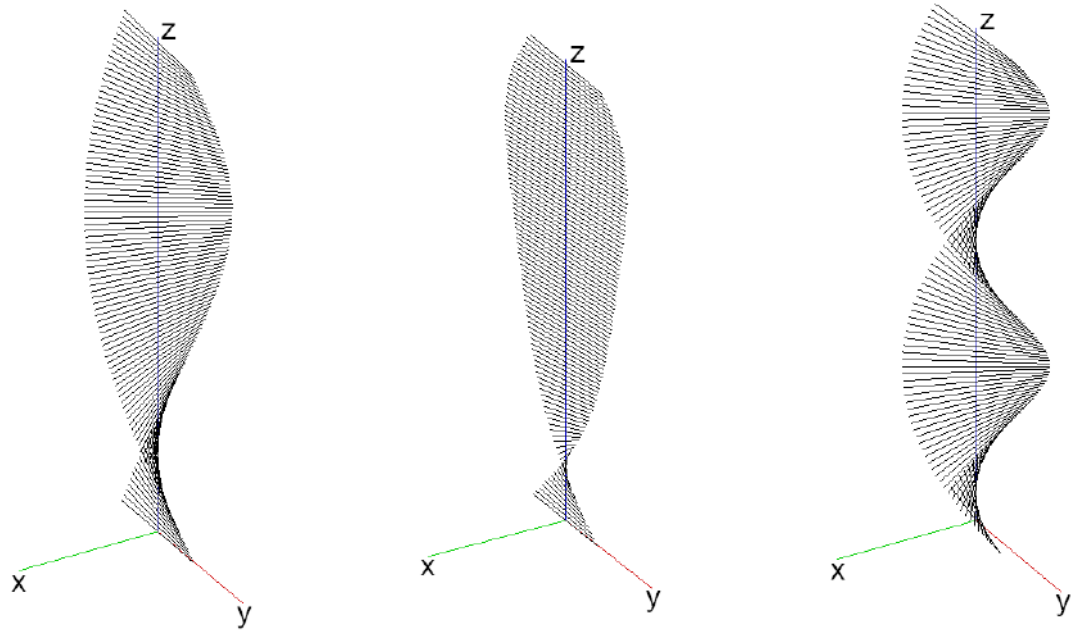

(*а*) (*б*) (*в*)

Figure 2.3. Metastable helical configurations with different numbers of half-turns k and various applied voltages U: (a) $k = 1$, $U = 0$ V (b) $k = 1$, $U = 1.4$ V; and (c) $k = 2$, $U = 0$ V; at anchoring energy coefficients $W_\varphi = 0.05$ mJ/m^2 and $W_\vartheta = 0.5$ mJ/m^2.

Figure 2.3 shows the equilibrium director configurations for the helical states of the CLC. Figure 2.3, *а* shows the state with one half-turn in the absence of an electric field ($U = 0$ V) with the director lying in the plane of the cell. At a voltage of $U = 1.4$ V, the structure begins to distort, coming out of the plane, corresponding to exceeding the Fredericksz threshold $U_{\text{th}}^{(1)} \approx 1.3$ V for the state with $k = 1$ (Figure 2.3, *б*). Figure 2.3, *в* illustrates the configuration with two half-turns, in which the director has already come out of the plane.

The estimation of the energy barrier for transitions between different helical states can be obtained by constructing a minimum energy path (MEP) between

these states. Studying the evolution of such a path with changing electric field allows for determining the field dependence of the energy barrier.

The MEP lies on the multidimensional energy surface of the system. Each point on it corresponds to a minimum energy in all directions except the direction along the path. Thus, the probability of finding the system near the MEP during the transition is maximum compared to nearby paths. At the saddle point, corresponding to the maximum energy value along the path, a minimum is reached in all directions except one, and a maximum is reached along the remaining direction. In the case of several MEPs, each of them is characterized by its saddle point, and multiple transition scenarios between the considered (meta)stable states are possible.

Two different initial approximations for the transition path between helical states with different numbers of half-turns were used to find the MEP. The first was chosen so that the director did not deviate from the plane parallel to the cell boundaries. The second involved deviation from the plane during the transition. For each of the initial paths, the MEP was found using the nudged elastic band method [20]. To investigate the effect of changing the electric field on the transition process between helical states, the MEPs found for the previous, slightly different field value were used as the initial approximation for each new field value. This accelerates the process of finding optimal paths.

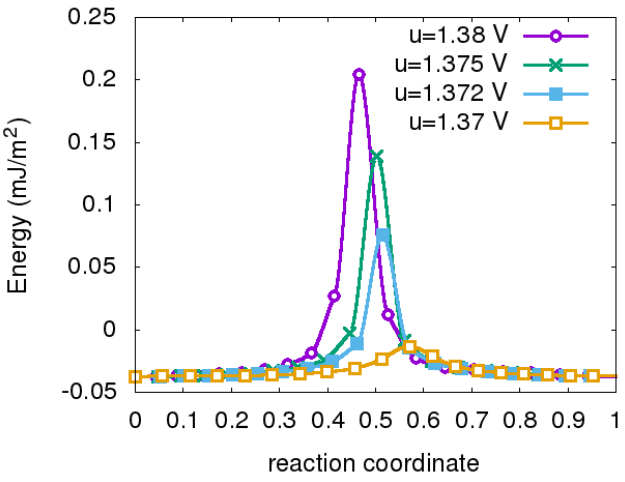

Figure 2.4. Energy per unit area along the minimum energy path from the state with one half-turn to the state with two half-turns at various voltages. The transition from the path through in-plane states to the path through out-of-plane states is observed. Parameters are listed in the caption of Figure 2.3.

Figure 2.4 shows the director configuration energies along the minimum energy path, calculated at the anchoring energy coefficients $W_\varphi = 0.05$ mJ/m^2 and $W_\vartheta = 0.5$ mJ/m^2 for the transition from the path through in-plane states to the path through out-of-plane states. A significant increase in the energy peak is observed as the voltage approaches $U = 1.38$ V. Figure 2.5 illustrates the development of out-of-plane deformations in the saddle structures during the transition, which can be interpreted as a change from director slipping to anchoring breaking. The tilt angle profiles for these configurations are shown in Figure 2.6.

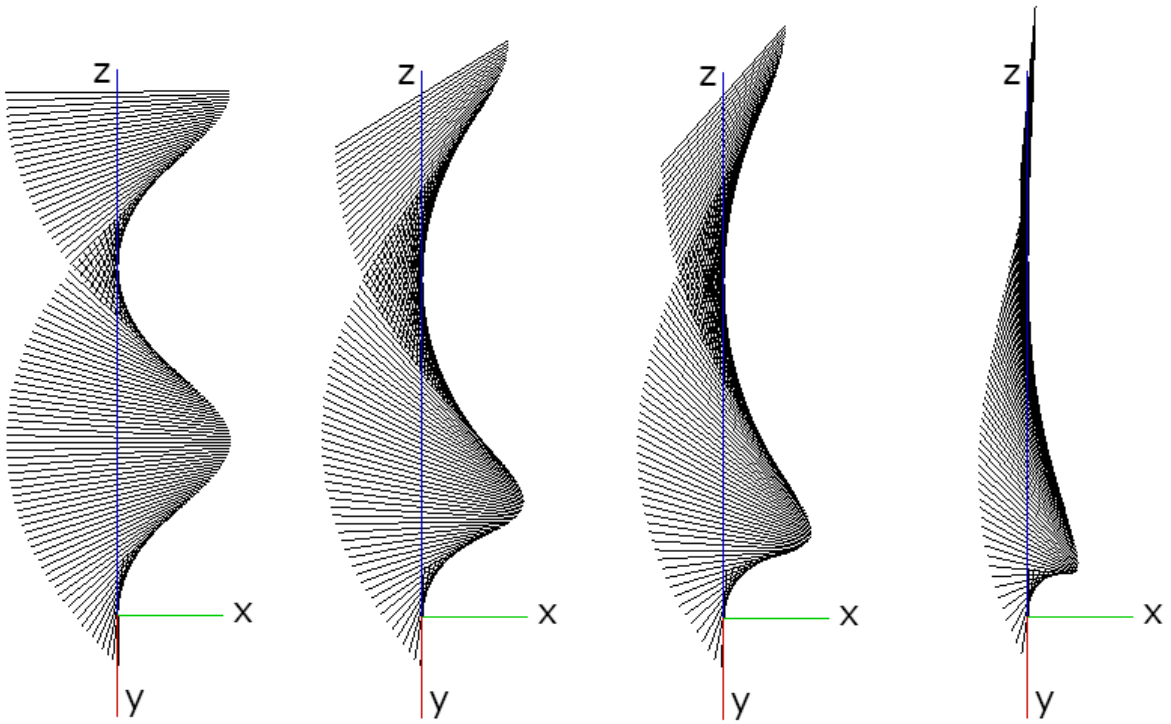

(*а*) (*б*) (*в*) (*г*)

Figure 2.5. Saddle structures for the minimum energy path shown in Figure 2.4. (a) $U = 1.37$ V, (b) $U = 1.372$ V, (c) $U = 1.375$ V, (d) $U = 1.38$ V. Parameters are listed in the caption of Figure 2.3.

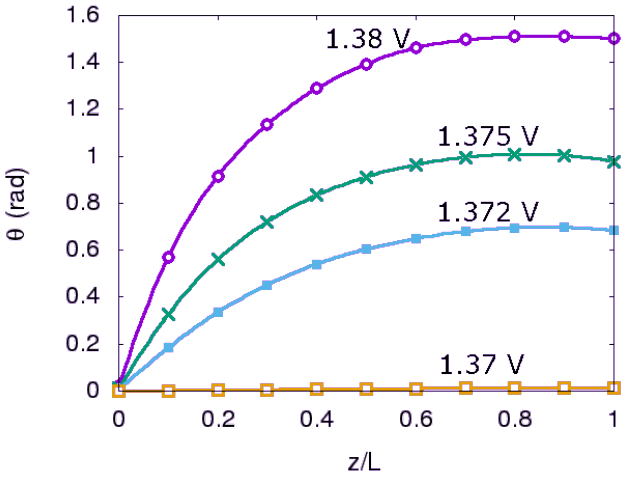

Figure 2.6. Tilt angle profiles for the saddle structures shown in Figure 2.5.

As an alternative initial approximation, a path with the director deviating from the plane was used, as described in detail in the work [11]. It is assumed that an out-of-plane deformation of the director is superimposed on the uniform twist from $\varphi_- = 0$ to $\varphi_+ = \pi/2$ with a change in the tilt angle ϑ from $\vartheta_- = 0$ to ϑ_+. In the

first half of the initial path, the tilt angle ϑ_+ on the upper substrate increases from zero to $\vartheta_+ \approx \pi/2$. Then, in the second half of the path, the angle ϑ_+ returns to the value $\vartheta_+ = 0$. Thus, for finding the MEP with anchoring breaking, it is assumed that in the transition state, the liquid crystal director on the upper substrate is almost perpendicular to the bounding surface.

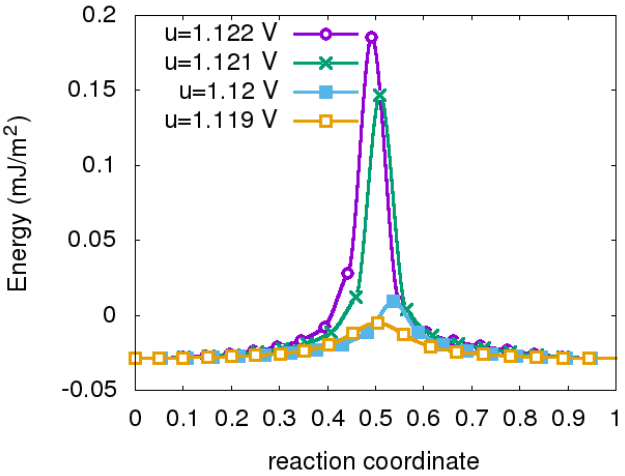

Figure 2.7. Energy per unit area along the MEP from the state with two half-turns to the state with one half-turn at various voltages. The transition from paths through out-of-plane states to paths through in-plane states is observed. Parameters are listed in the caption of Figure 2.3.

Figure 2.7 shows how the surface energy density of the LC changes along the MEP as the voltage decreases from $U = 1.122$ V to $U = 1.119$ V. Note that these voltages are below the Fredericksz transition, where the structure at the saddle point is characterized by noticeable tilt deformations. At high voltages, the approximation of director slipping and anchoring breaking leads to similar results for the MEP. These paths can be smoothly continued into the low voltage region. Note that as the voltage decreases, the energy barrier decreases. The observed changes in the MEP can be considered as a transition from a path with out-of-plane deviation to a path without out-of-plane deviation.

2.3. Hysteresis Effects with Changing Electric Field in Cholesteric Liquid Crystals

In the previous section, it was shown that with changing voltage, the MEP and the transition scenario can change their character. At low voltages, the initial director configuration along the path changes without deviating from the plane parallel to the cell boundary. As the voltage increases to a critical value $U_{c\uparrow} \approx 1.38$ V, a sharp increase in the energy barrier is observed, associated with the change in the transition mechanism from in-plane configurations to out-of-plane deviations. In the reverse process of decreasing the voltage from high values, the system follows a path from states with the director deviating out of the plane to in-plane states at a lower voltage. As a result, $U_{c\downarrow} \approx 1.12$ V becomes the threshold for the mechanism change. Thus, the dependence of the energy barrier on the voltage forms a hysteresis loop, illustrated in Figure 2.8.

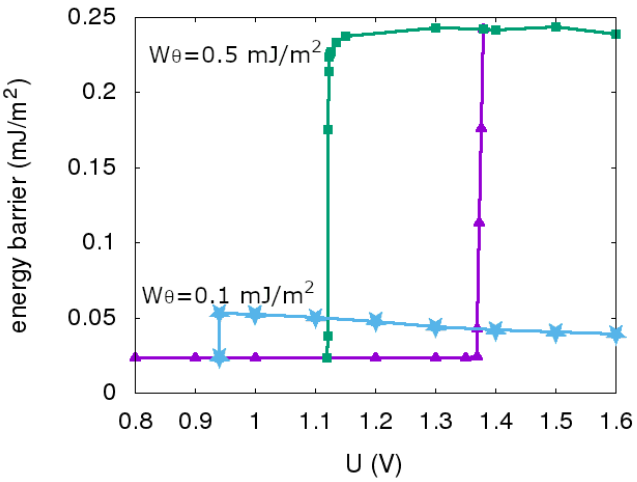

Figure 2.8. Dependence of the MEP barrier on voltage for different transitions: on the path with increasing voltage (purple triangles) and on the path with decreasing voltage (green squares and blue stars) at different values of polar anchoring strength. The anchoring parameter W_φ is 0.05 mJ/m^2.

It should be noted that the critical field $U_{c\downarrow}$ is lower than the Fredericksz thresholds for both the initial and final states, indicating the possibility of an anchoring breaking mechanism even for in-plane director configurations in the initial and final

states. The energy barriers obtained with sequentially increasing and decreasing voltage form a hysteresis loop, demonstrating a change in the transition mechanism depending on the voltage history. It is also observed that as W_φ decreases, the hysteresis loop expands, indicating the significant role of the director's interaction with the substrates in the dynamics of the transition processes.

Conclusions to Chapter 2. Transitions between locally stable helical states with different numbers of helical turns were studied in cholesteric LCs. The primary and metastable states of the CLC, corresponding to local energy minima, are determined depending on the applied electric field. It is shown that with changing external conditions, such as the electric field voltage, the shape of the energy surface and the positions of the minima change, which can lead to transitions between these states. The minimum energy paths between states were considered, as well as the conditions and mechanisms of their occurrence and changes depending on the system parameters and external influences. It was found that depending on the voltage and the anchoring parameters with the substrates, the energy barrier between states can significantly change. Hysteresis of the energy barrier change depending on the voltage history is observed in cholesteric liquid crystals.

Chapter 3

Topological LC and Magnetic Structures in Confined Geometries

Localized nano- and micro-sized states in liquid crystals and magnets are of great interest both from the perspective of fundamental theory and practical applications. The study of such structures in thin films is particularly important for the development of new magnetic memory technologies and LC devices. To predict their properties, stability, and dynamics, it is necessary to understand the ground state of the system, against which localized structures form. This chapter is dedicated to studying various ground states in thin films, analyzing their evolution as system parameters change, and constructing a phase diagram of possible states. Additionally, localized states and their existence domains will be considered.

3.1. Helical and Conical Chiral Structures in an External Field

Let us consider a system with energy given by equation ((1.2)). As noted earlier, in the absence of anisotropy, the state with minimal energy is a helical structure with a period

$$p_0 = 2\pi / \arctan \frac{D}{J}, \tag{3.1}$$

Hereafter, we will investigate the structure with thickness $d = p_0 = 20\,a$, where a is the lattice constant in the simulation, which in a magnetic system corresponds to the crystal lattice constant. Periodic boundary conditions will be used in the plane of the film, along the x and y axes, as before. First, we will consider states homogeneous along the y axis. This restriction will be lifted later.

By minimizing the energy ((1.2)), we can find configurations corresponding to the minimum energy. These states change with variations in anisotropy. Some of them may be completely unstable at certain values of the pair K^b and K^s and have the lowest energy (thus being the ground state) at others. To find the local energy minimum, the conjugate gradient method was used in Cartesian coordinates for the vectors $\mathbf{m}_k$, under the condition that $\mathbf{m}_k^2 = 1$ [20, 56].

Given certain values of anisotropy, the system may have, along with the global minimum, several local minima, which include non-localized states, such as domain walls, helices, etc., and localized states such as skyrmions, torons, hopfions [57, 58]. The confinement along the z axis provides greater diversity of metastable states and influences which one will be the ground state under given parameters.

In an unbounded space, as the anisotropy K^b decreases, the ferromagnetic (uniform) state with magnetic moments (directors) ordered along the z axis, which is the ground state at high anisotropies, transitions at a certain critical value $K^b > 0$ into a helical state with the rotation axis in the plane perpendicular to z. When K^b changes sign, the axis of the helix reorients along the axis of the easy-plane anisotropy.

A similar behavior occurs for skyrmion tubes in an external magnetic field. As the field decreases, the lowest energy state changes from tubes oriented along the field to tubes perpendicular to the field [58]. Note that in all the states described above, the projection of the moments on the axis of the helix remains zero.

In films of finite thickness, the presence of bounding surfaces introduces an additional preferential direction. The global minimum in a confined system (Figure 3.1) is determined by many factors, including the film thickness, anisotropy inside and on the surface of the film.

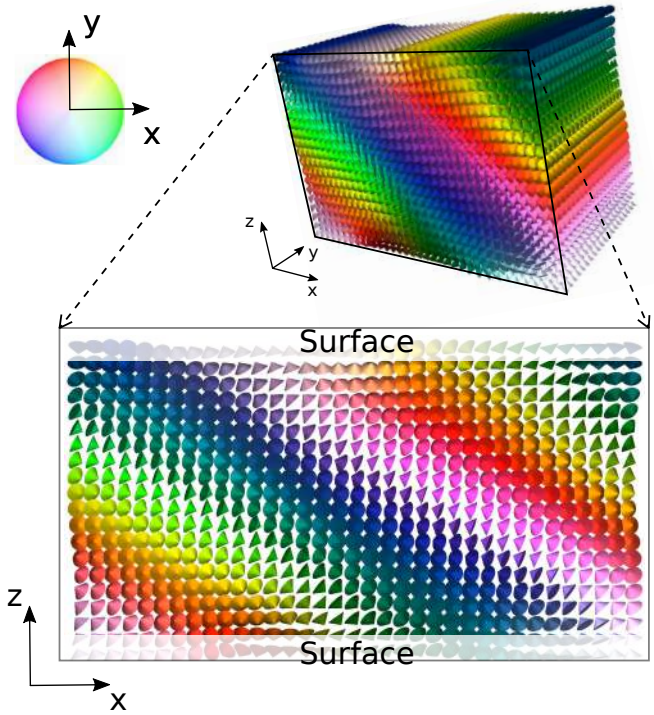

Figure 3.1. Cell of a chiral medium. The top image shows a three-dimensional system with a rectangular grid. The bottom image shows one layer of the grid in the xz plane. The top and bottom surfaces correspond to the boundaries of the cell, where additional anisotropy is added in the simulation for the orientation-dependent part of the surface energy (in colloidal liquid crystals, this corresponds to the surface anchoring energy). The color palette describes the x and y projections of the magnetic moments. Periodic boundary conditions are assumed in the xy plane.

In the considered system, with relatively small K^b, the global energy minimum is the z-helix ((1.25)) with a period close to p_0. In a semi-infinite space $z \geqslant 0$ with rigid boundary conditions, where the magnetic moments at the boundary are directed along the z axis, the global minimum can be found analytically. Such a solution must be homogeneous in the xy plane and can be described in terms of the polar and azimuthal angles $\theta(z)$ and $\phi(z)$, where θ is the angle between the magnetic moment (or director) and the z axis. We write the boundary conditions for θ:

$$\theta(z)\big|_{z=0} = 0, \qquad \theta(z)\big|_{z=\infty} = \frac{\pi}{2}, \tag{3.2}$$

and the solution:

$$\theta(z) = 2\arctan\exp\left|\frac{\mathcal{D}}{2\mathcal{A}}z\right| - \frac{\pi}{2}, \quad \phi(z) = \phi_0 + \frac{\mathcal{D}}{2\mathcal{A}}z, \tag{3.3}$$

where ϕ_0 is the value of the angle ϕ at $z = 0$. This solution represents such an ordering of the magnetic moments (director orientation), where they uniformly rotate around the z axis, and their projection on the z axis decreases with increasing z.

In finite-thickness films with a given value of surface anisotropy K^s, the solution can be obtained numerically. Figure 3.2 shows the dependence of the z-projection of the magnetization on the distance from the lower boundary of the film for two configurations, which we will call "cone-I" and "cone-II". For the first configuration, shown on the left, m_z is an even function of the distance to the middle of the sample. For the second, on the right, it is odd. The configurations themselves are also shown in the figure. The different curves correspond to different values of the parameter κ^s.

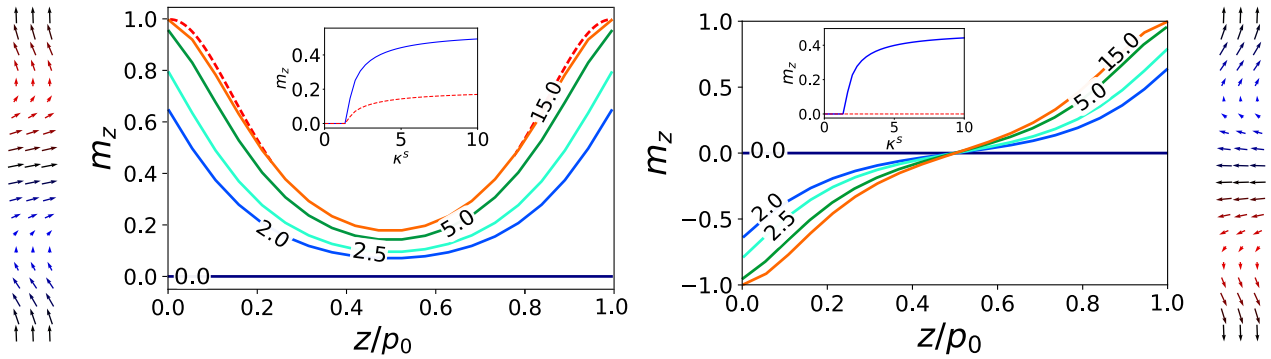

Figure 3.2. Z-projection of the normalized magnetization m_z for different values of surface anisotropy κ^s and bulk anisotropy $\kappa^b = 0$. The left and right panels show the cone-I and cone-II solutions, respectively. Insets show the average values of m_z for the entire film (blue solid line) and the middle layer (red dashed line) as a function of κ^s. For $\kappa^s < 1.4$, the magnetization lies in the plane of the film for both cone-I and cone-II. The dashed line represents the analytical solution for a semi-infinite space and $\kappa^s = \infty$.

For thin films, the cone-II state, in which the z-projection decreases and reaches zero as it approaches the center of the sample, is energetically unfavorable. However, this state, if formed, can be stable, analogous to one-dimensional domain walls in

magnets. In thick films, where the z-projection of the moment in the center is close to zero for both states, their energies are almost identical. Note that for LCs, the sign of the director projection is not important, so these states can be considered indistinguishable. However, these states are topologically nonequivalent.

For non-zero anisotropy $K^b < 0$, the transition from the z-helix (a state with zero projection on the z-axis) to the z-cone occurs at different values of κ^s, increasing with $|\kappa^b|$. The transition from the z-helix to the z-cone has much in common with the classic Fredericksz transition, which occurs in LCs under the influence of an electric or magnetic field. Note that both of these states exist, at least as metastable states, throughout the studied phase diagram. The following sections will show that the transition from the z-helix to cone-I, occurring with increasing K^s, can be more complex and pass through the tilted helix state.

In an unbounded sample with small anisotropy $K^b > 0$ along the z-axis, the global minimum is an x-helix with a pitch slightly larger than p_0. For $K^b < 0$, this is no longer the case. However, in thin films, boundary conditions with $K^s > 0$ stabilize x-helical structures, which can appear at various values of K^s, as long as K^b is not too large.

Figure 3.3 shows the results of the calculation of the magnetic/LC structure with periodic conditions along the x-axis, homogeneous in the y-axis direction. The surface anisotropy κ^s from left to right is 10, 20, and 30. The bulk anisotropy $\kappa^b = 0$. States with periods corresponding to the minimum energy per lattice site are shown. Calculations were performed with different periods l_x to determine these. Systems of different sizes differ in the helix pitch: $p_x = l_x/n$, where n is the number of structure periods in the modeled system. Thus, the energies of metastable states with different pitches p_x were determined for various κ^b and κ^s.

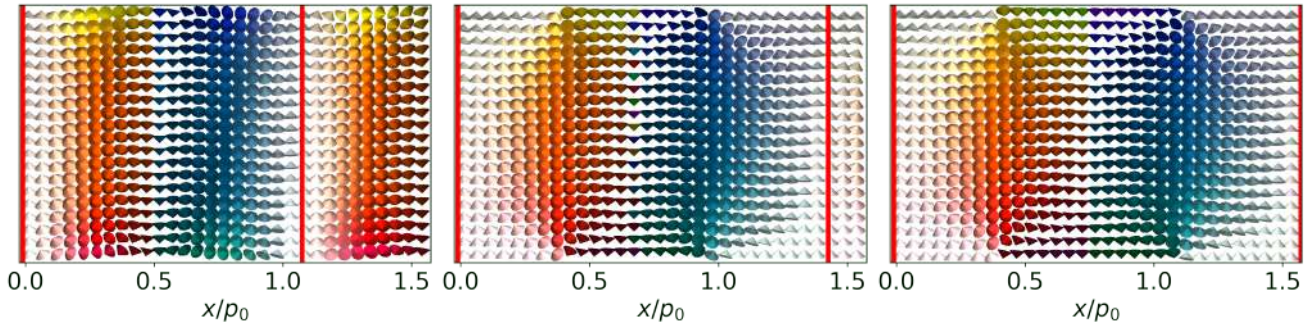

Figure 3.3. x-helix in the absence of bulk anisotropy $\kappa^b = 0$ and at different values of surface anisotropy κ^s: 0 (left), 10 (middle), 20 (right). One pitch of the x-helix in the magnetic film is shown between the red lines. For liquid crystal, the pitch is half as much.

Calculations showed that the pitch of the helix p_x depends on surface anisotropy, increasing with κ^s. For the presented structures, the helix pitch increased by more than one and a half times.

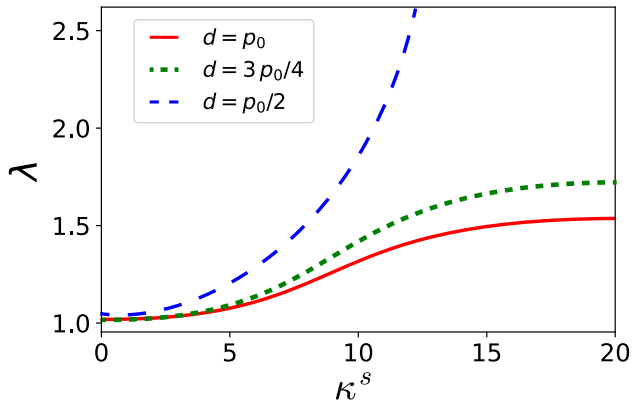

Figure 3.4. Ratio of the x-helix pitch in the film p_x and in the infinite medium p_0, $\lambda = p_x/p_0$, as a function of surface anisotropy κ^s for films of different thicknesses d. The bulk anisotropy $\kappa^b = 0$.

Figure 3.4 shows the dependence of the normalized helix pitch $\lambda \equiv p/p_0$ on surface anisotropy for films of different thicknesses d. For small surface anisotropies κ^s, the pitch is close to p_0 for all thicknesses. In thick films, the helix pitch increases with increasing κ^s and reaches a finite value as $\kappa^s \to \infty$. In thin films with $d < p_0$, the helix pitch increases indefinitely, leading to unwinding of the helix. This is consistent with the results of [59] on equilibrium configurations and the phase diagram in thin films with uniform boundary conditions.

It should be noted that similar structures were studied in the work [60], where an analytical solution was found for the case of rigid boundary anchoring. The analytical work was carried out assuming that the director is normal to the x-axis everywhere. However, numerical minimization showed that such an assumption could lead to significant discrepancies with the actual minimum. According to calculations for thick films with $\kappa^b = 0$, the x-projection of the magnetization initially decreases with κ^s because the magnetic moments near the boundaries are aligned along the normal to the surface. After reaching a minimum at $\kappa^s \simeq 5$, the projection on the x-axis begins to increase due to the rotation of moments in the boundary layer. Such structures were discussed in the work [61].

3.2. Tilted Helix State in Thin Chiral Films

Let us consider the z-helix and z-cone at various anisotropy parameters $\kappa^b < 0$, $\kappa^s > 0$. The transition between these two states occurs with increasing anisotropy κ^s. It is worth noting that the Fredericksz transition in cholesteric LCs under the influence of external electric and magnetic fields passes through similar states. Such a transition between "in-plane" and "out-of-plane" director states in LCs can be either continuous or discontinuous, depending on the system parameters [54].

Unlike the Fredericksz transition, in our model, the transition from the z-helix to the z-cone passes through a new state - the tilted helix, shown in Figures 3.1 and 3.5. Moreover, this state turns out to be the global energy minimum in a certain range of anisotropies κ^s. Note that similar structures can arise in an unbounded sample, driven by the competition between local cubic and exchange anisotropy [62].

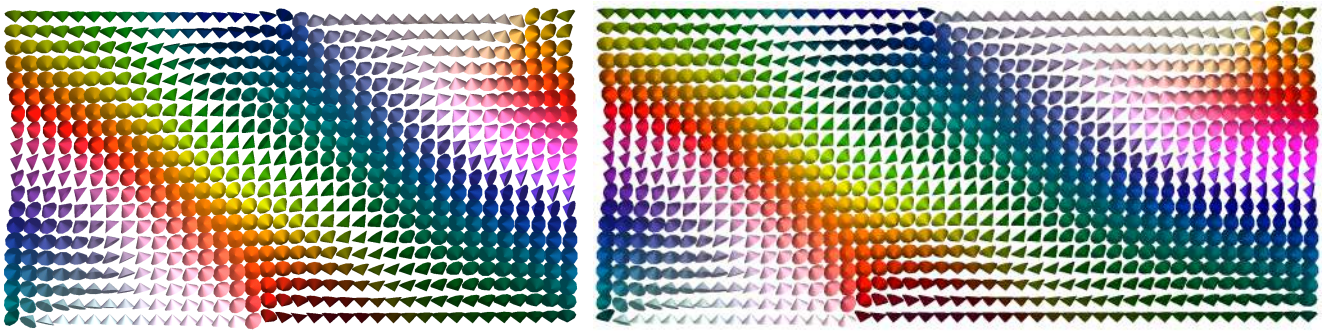

Figure 3.5. Tilted x-helix at $\kappa^b = 0$, $\kappa^s = 10$ (left panel) and $\kappa^b = 0$, $\kappa^s = 20$ (right panel).

The tilted helix state can be characterized by the period p and the tilt angle of its axis from the z axis. Both parameters depend on the anisotropies $\kappa^s > 0$ and κ^b. Figure 3.5 shows the tilted helix calculated in the absence of bulk anisotropy $\kappa^b = 0$, at two different values of surface anisotropy $\kappa^s = 10$ and $\kappa^s = 20$. It can be seen that with $\kappa^b = 0$, the tilt angle of the helix decreases with increasing surface anisotropy.

To estimate the tilt angle of the helix, note that the spatial dependence of the magnetic moment (LC director) in the volume will be determined by the projection $s = \mathbf{r} \cdot \mathbf{q}/q^2$ of the vector $\mathbf{r}$ onto the helix axis $\mathbf{q}$:

$$\mathbf{m}(\mathbf{r}) = \mathbf{m}(\mathbf{r}_0 + s\mathbf{q}) = \mathbf{m}(s), \tag{3.4}$$

for all s and any fixed $\mathbf{r}_0$. Therefore, the elements of the magnetization gradient matrix can be written as:

$$(\nabla \mathbf{m})_{ij} \equiv \nabla_i m_j = \frac{q_i}{\mathbf{q}^2} \frac{\mathrm{d}m_j}{\mathrm{d}s}. \tag{3.5}$$

In the discrete model with energy (1.2), the gradient matrix is represented by finite differences and has small deviations from this form. To reduce errors, $\mathbf{q}$ is approximated by the left singular vector of the gradient matrix corresponding to the largest singular value. As a result, the expression for the tilt angle α takes the

following form:

$$\alpha = \arccos \frac{\mathbf{q} \cdot \mathbf{z}}{\mathbf{q}^2}. \tag{3.6}$$

The tilted helix forms in a system with a confined geometry and exists as the ground state only at certain film thicknesses d. The tilt angle α and the period p_x also depend on the film thickness. Figure 3.6 shows the dependence of the dimensionless period $\lambda = p_x/p_0$ on the film thickness. It can be seen that the period is a monotonically increasing function of the thickness d, while the tilt angle decreases with thickness. Thus, the tilted helix transitions to the z-cone in the limit of a thick film. As the thickness decreases, the tilted helix approaches the x-helix down to a critical thickness of $d \approx 0.65\, p_0$.

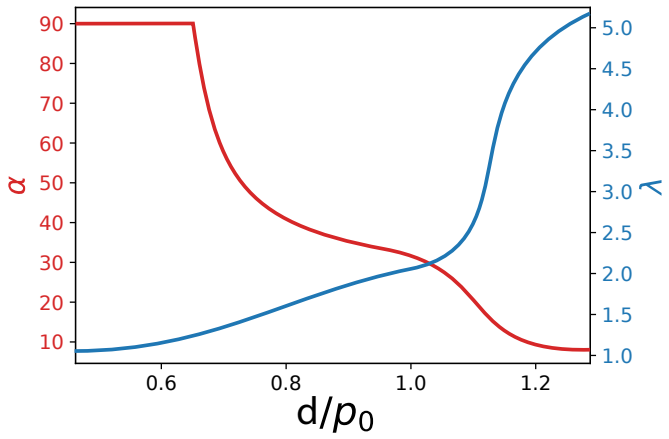

Figure 3.6. Tilt angle α and dimensionless period $\lambda = p_x/p_0$ (p_0 is the equilibrium helix pitch in a bulk sample) of the tilted cone as a function of film thickness d, calculated at $\kappa^b = -0.2$ and $\kappa^s = 0$.

Analogous to the x-helix, metastable configurations of the tilted helix were considered for different sizes of the modeled regions to find the period p_x corresponding to the minimum energy of the system. The x-helix and the tilted helix coexist as metastable states and differ in period and energy. To assess the stability of these states, it is useful to construct the energy surface of the system and find the MEP between these states. The energy maximum along this path will give the value of the energy barrier between the states. As mentioned earlier, the MEP can be found using the nudged elastic band method [63] or other specialized methods [64, 65].

This approach is used to study the stability of both magnetic systems [9,66,67] and liquid crystals [10,11,15].

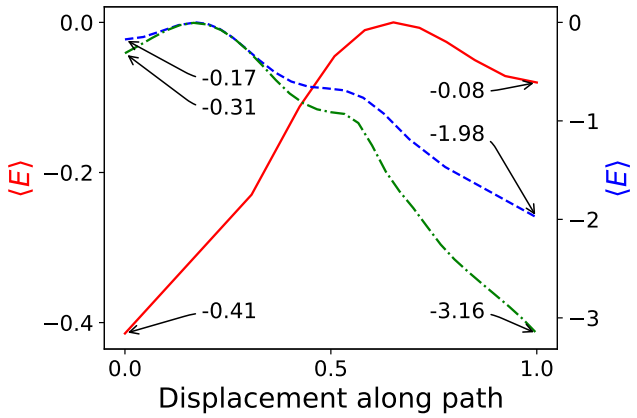

Figure 3.7. MEP between the tilted helix and the x-helix at $\kappa^b = -0.05$ (left axis, solid line) and $\kappa^b = -0.1$ (right axis, dashed line) for fixed surface anisotropy $\kappa^s = 5$ and helix pitch $\lambda = 1.1$. The dash-dotted line shows the MEP with helix pitch optimization along the path, as shown in Figure 3.8. The average energy per magnetic moment $\langle E \rangle$ is presented in units of $J \cdot 10^{-5}$ and is measured relative to the energy at the saddle point.

Figure 3.7 shows the MEPs between the states of the x-helix and the tilted helix for a fixed size of the modeled system with dimensionless pitch $\lambda = 1.1$ and surface anisotropy $K^s = 5$. Solid and dashed lines show results for different values of anisotropy within the sample: $\kappa^b = -0.05$ and $\kappa^b = -0.1$, respectively. Thus, the x-helix, which was the ground state at small values of $|\kappa^b|$, becomes metastable with increasing internal anisotropy.

The results marked by the dotted line with points in Figure 3.7 were obtained by minimizing the energy considering the change in pitch p_x. Figure 3.8 shows a heat map displaying the energy along the minimum energy path between the states of the x-helix and the tilted helix. The lines drawn at constant λ on the map correspond to MEPs in a system with a fixed cell size along the x-axis, and thus with a given pitch. The local coordinate (displacement along the MEP) is taken as 0 for the x-helix and 1 for the tilted helix. The pitch corresponding to the minimum energy of the x-helix is $\lambda = 1.10$, and for the tilted helix, it is $\lambda = 1.12$. Note that λ changes continuously along the path.

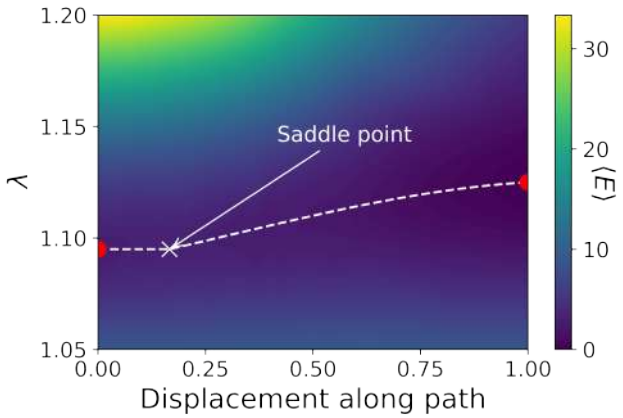

Figure 3.8. Energy as a function of the helix pitch λ and the reaction coordinate of the MEP from the x-helix (left boundary) to the tilted helix (right side) at $\kappa^b = -0.1$, $\kappa^s = 5$. The MEP is marked by the dashed line, and the cross marker indicates the transition state. The average energy per spin $\langle E \rangle$ is measured in units of $J \cdot 10^{-5}$ and is measured from the lowest energy.

Thus, the two-dimensional surface presented in Figure 3.8 introduces an additional degree of freedom in the form of the possibility of varying λ. The optimal MEP passes through chiral structures with different periods during the transformation from the x-helix to the tilted helix. Both the initial and final structures for this transition have the minimum possible energy for the given system parameters. The corresponding energy along this path is shown by the dashed line in Figure 3.8, as well as in Figure 3.7 by the dashed line with points.

The energy barriers obtained from the MEP can be used to assess the stability of the states. Real transitions between states may not occur throughout the entire volume but gradually, through local transitions of structures in the region of defects. Analogous to domain wall movement, such a transition would not require additional energy.

States associated with the tilted helix in the chiral medium have been observed experimentally in LCs [29,59]. They belong to the class of "cholesteric fingers". The behavior of such systems under changing external conditions and transitions between the corresponding states can be described using the model described above. Note that in LC systems, the anisotropy κ^b is caused by an external electric or magnetic field. In experiments with liquid crystals, the transition from the tilted helix to

the z-cone was observed when the value of the "easy-plane" anisotropy $\kappa^b < 0$ increased [12]. Figure 3.9 shows the evolution of states with changing external field. With increasing tilt angle, a transition to the z-helix occurs, which agrees well with the director distribution observed in experiments with cholesteric liquid crystals [12].

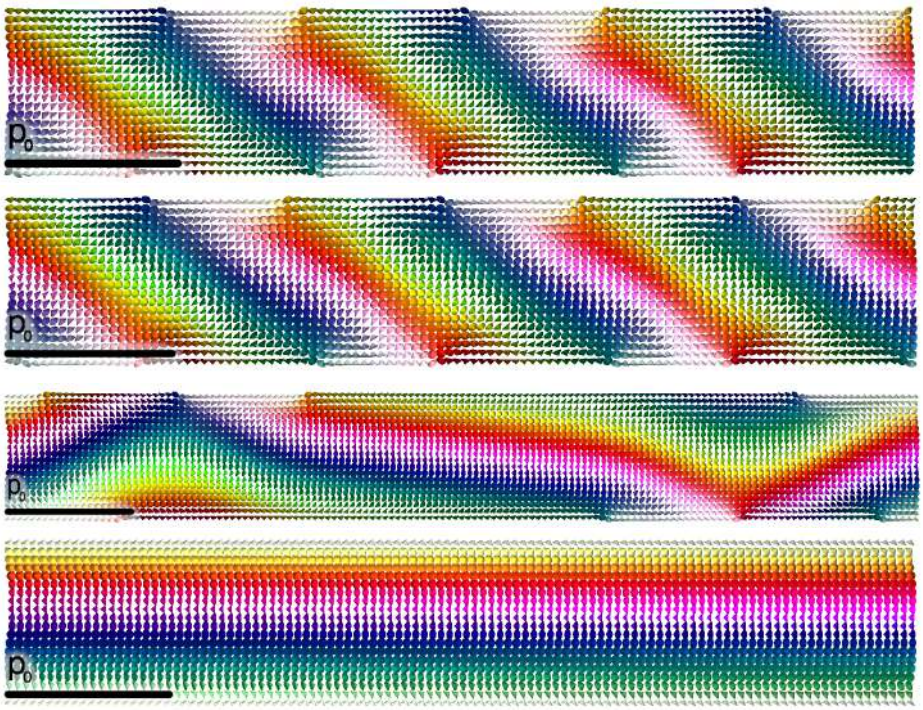

Figure 3.9. Evolution of the tilted helix with changing bulk anisotropy κ^b from 0 (top), through -0.2 and -0.8 to -2.4 (bottom) assuming constant surface anisotropy $\kappa^s = 11$.

3.3. Phase Diagram of Chiral Magnets and Liquid Crystals in Thin Films

The calculation of the energy of magnetic/LC configurations in a chiral medium within thin films allows us to construct a state diagram depending on the anisotropy parameters inside the film κ^b and on its surface κ^s. Such a diagram is shown in Figure 3.10.

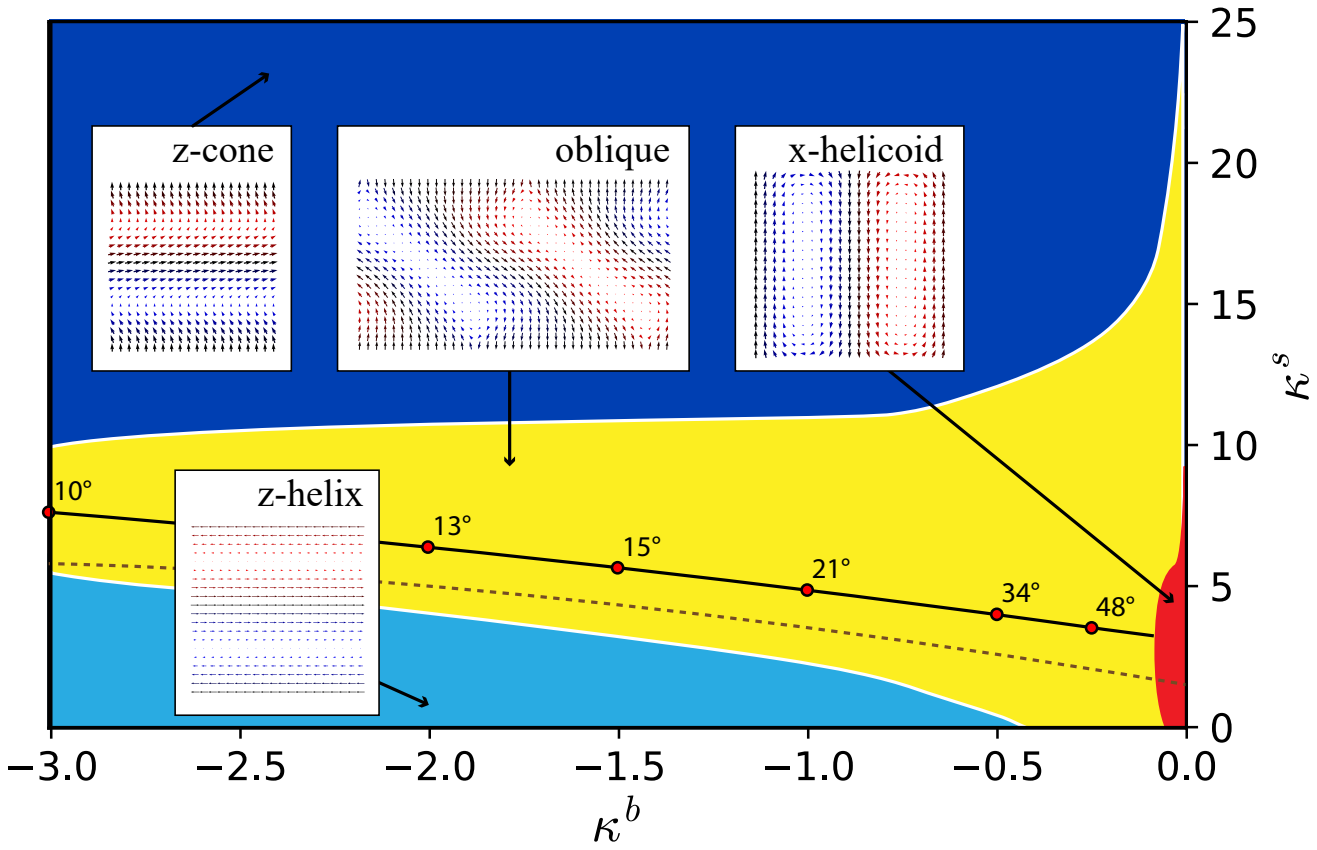

Figure 3.10. Phase diagram of the chiral medium in the κ^b-κ^s plane, calculated for a film thickness of $d = p_0$. The magnetic system/LC configurations are shown in the insets. The equal energy curve for the z-helix and z-cone is marked with a dashed line. The black solid line marks states with the maximum tilt angle α of the tilted helix axis.

In the entire region $\kappa^b \leqslant 0$ and $\kappa^s \geqslant 0$ shown in Figure 3.10, the z-helix and cone I states exist as either ground or metastable states. The areas where the z-helix and cone I have the lowest energy are marked in blue and dark blue on the diagram, respectively. Examples of configurations at the points indicated by arrows are shown in the insets. The black dashed line corresponds to the curve on the κ^b-κ^s plane where the energies of these states become equal. Note that for a given value of κ^b, the transition from the z-helix to cone I occurs when the surface anisotropy κ^s exceeds a threshold value. This value is a monotonically increasing function of $|\kappa^b|$. The transition itself is realized through an intermediate state—a tilted helix, which is the ground state in the region marked in yellow on the phase diagram.

The tilt angle α of the tilted helix axis from the film normal, introduced above

((3.6)), first increases from zero to a maximum value, marked on the phase diagram by a black line, and then decreases to zero as the tilted helix transforms into cone I. Since the tilted helix exists only in a limited region of the phase diagram, at larger values of κ^b (this area with higher fields is not shown on the phase diagram), the transition between the z-helix and cone I occurs without the tilted helix as an intermediate state.

With small bulk anisotropy, in the region marked in red on the phase diagram, the ground state is the x-helix. It was previously noted that such a configuration is stabilized by boundary conditions in the absence of κ^b. Increasing κ^s transforms the x-helix into a tilted helix.

Figure 3.11 shows the dependence of the tilt angle α of the tilted helix on bulk and surface anisotropy. The left plot shows the dependence of α on anisotropy inside the sample at various values of surface anisotropy. It can be seen that the angle α is a decreasing function of the anisotropy inside the sample $|\kappa^b|$. The maximum value of this angle is close to $\pi/2$ and is reached at a κ^s value less than 10. The angle approaches zero in the limit of large fields.

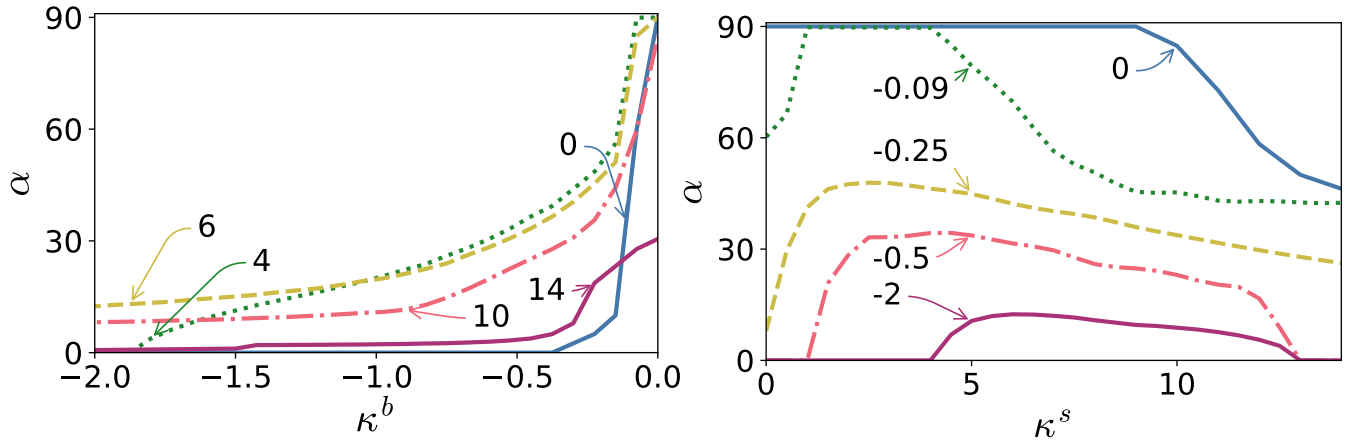

Figure 3.11. Tilt angle α (in degrees) of the tilted helix as a function of bulk anisotropy κ^b (left) and surface anisotropy κ^s (right). The limiting cases with $\alpha = 0$ and $\alpha = 90°$ correspond to the z-cone and x-helix, respectively.

The right plot in Figure 3.11 shows the dependence of α on the anisotropy on

the surface of the sample at various values of anisotropy inside the sample. When $|\kappa^b|$ is small, the maximum angle is $\pi/2$, which corresponds to the x-helix. As $|\kappa^b|$ increases, the maximum tilt angle decreases, in accordance with the phase diagram (Figure 3.10).

3.4. Localized States in Chiral Liquid Crystals and Magnets

Localized structures in chiral media, sometimes called "topological solitons," can arise in different parts of the phase diagram. Their stability, mutual transformations, and dynamics are of great interest from both fundamental physics and application perspectives.

Figure 3.12 shows three types of localized magnetic configurations, referred to as a skyrmion tube, a leech, and a toron. The orientation of the magnetic moments differs from the directions of the moments in the surrounding matrix by more than 15°. Similar structures, called "baby skyrmions," have been experimentally observed in homeotropically oriented LC cells [68].

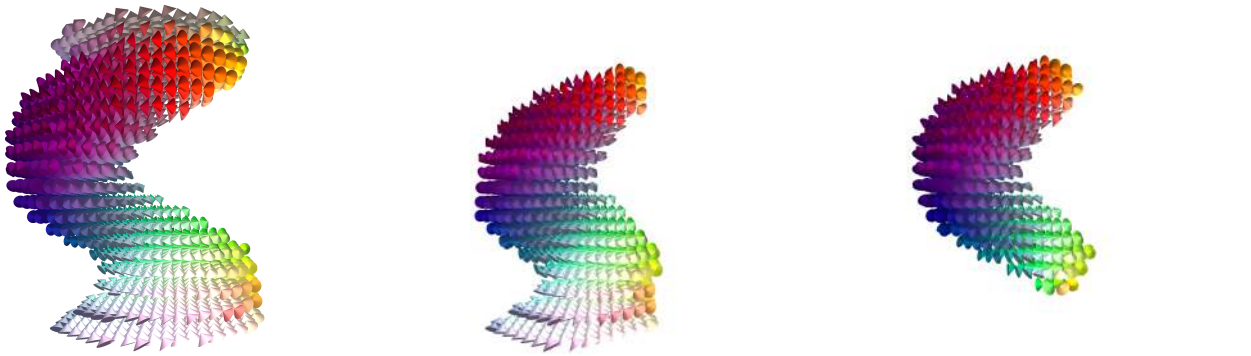

(a) (b) (c)

Figure 3.12. Topological structures found in the conical phase: skyrmion tube (a), leech (b), toron (c). Spins oriented the same as in the cone are not shown.

The magnetic configuration known as the skyrmion tube is shown in Figure 3.12*a*. This structure in the film resembles vertical skyrmion tubes in bulk chiral magnets in a magnetic field [58, 69]. It is known that in a relatively small magnetic

field, the magnetically induced conical phase exerts a twisting effect on the tube, leading to a crankshaft-like structure.

Another configuration, shown in Figure 3.12*c*, is called a toron according to the terminology introduced in [31]. It is located in the volume of the film and touches the boundary surfaces. Such structures have been observed in LC and magnetic systems [70]. The magnetic moments on the surfaces of the film with a toron hardly change orientation, while in the horizontal cross-section in the middle of the film, the structure is similar to a skyrmion tube. Although the toron in Figure 3.12*c* resembles the one described in [31], in this case, the torons are surrounded by the conical phase, which, like in the case of the skyrmion tube, causes the torons to twist.

The structure shown in Figure 3.12*b* represents an intermediate case between the skyrmion tube and the toron: it is attached to only one of the boundaries and, like the toron, has a tail 3.12*c*. This structure is called a leech. Note that leech-like structures forming in asymmetric LC cells were previously described in [31, 71] as skyrmion/toron hybrids. Unlike hybrids, our structures form in symmetric cells and are twisted due to the presence of the surrounding conical phase.

In addition to topological solitons touching or adjacent to both surfaces of the film, structures localized near one of the boundary surfaces were discovered. Similar structures, called chiral bobbers, were predicted and observed in thick magnetic films [30, 70]. The bobber structure is shown in Figure 3.13. The isosurface for m_z is shown on the right side of Figure 3.13. The colors of this surface code the orientation of the spins in the xy plane, which is set by the azimuthal angle. The coding is similar to that presented in 3.1.

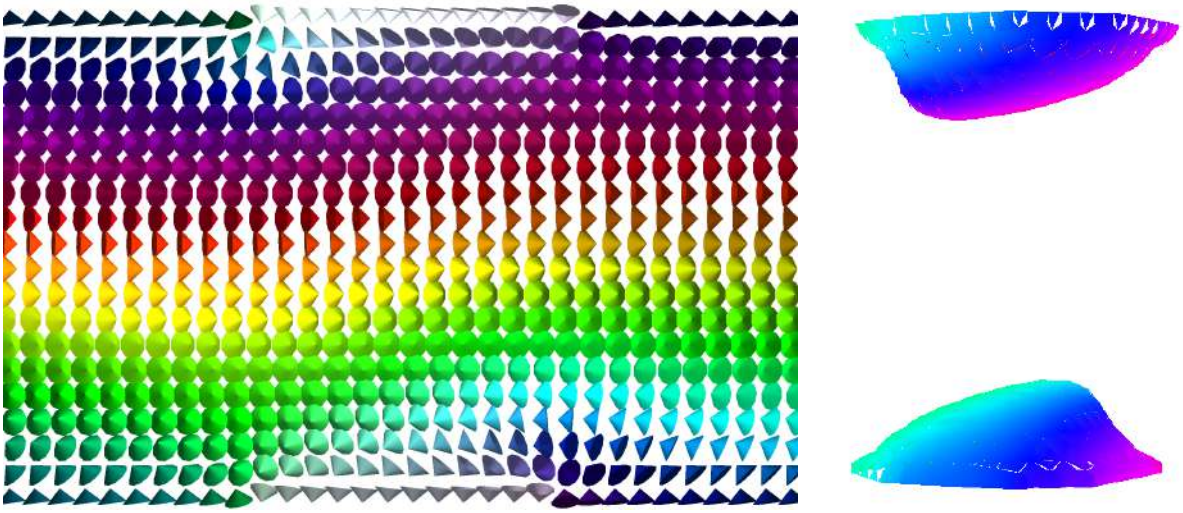

Figure 3.13. Bobber in the conical phase, yz projection, left: all spins of one layer are shown, right: isosurface of constant $m_z = 0.85$.

Figure 3.14 shows the regions of local stability for various localized topological states on the phase diagram. It can be seen that in the conical phase there is a region where all the above states coexist: 3.12-3.13.

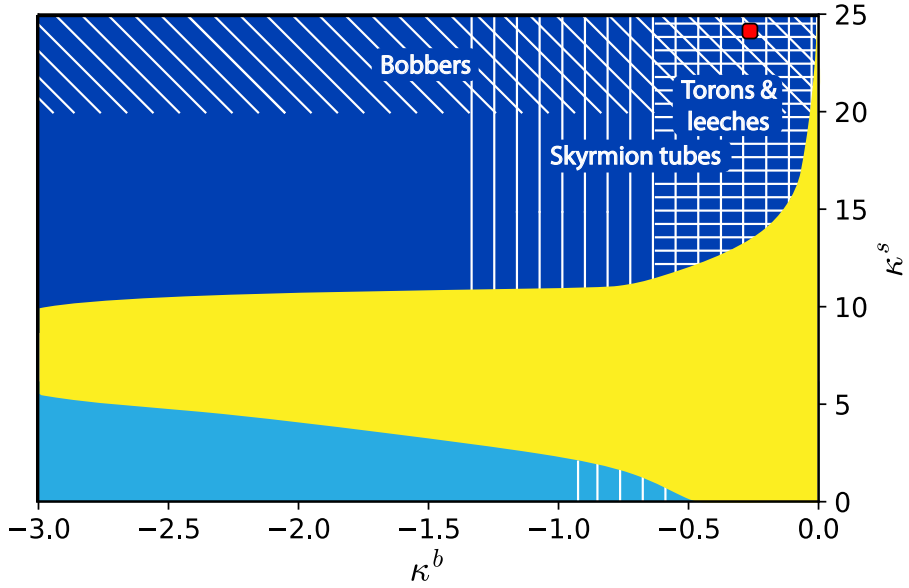

Figure 3.14. Regions where different types of metastable topological states exist: skyrmion tubes - vertically shaded area; torons and leeches - horizontally shaded area; bobbers - diagonally shaded area.

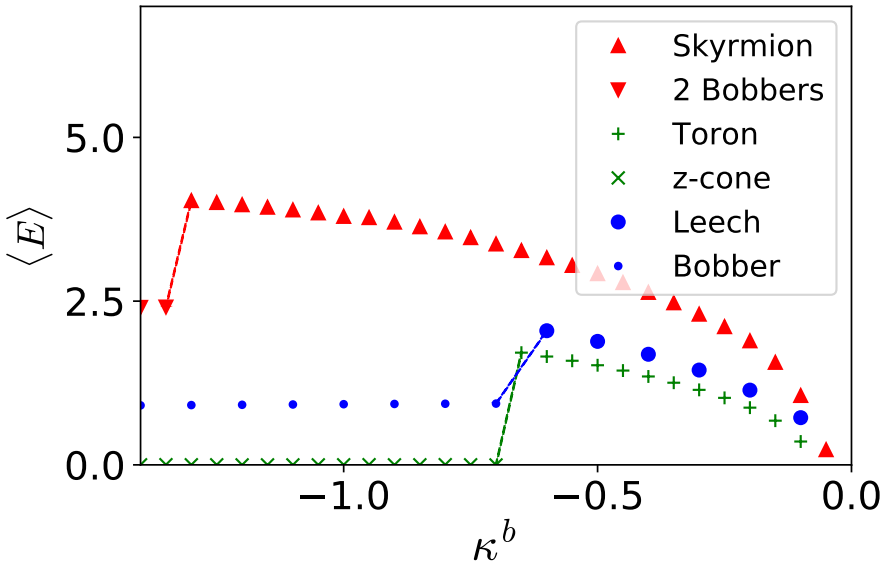

Figure 3.15. Energy dependence of various topological solitons on bulk anisotropy κ^b at $\kappa^s = 24$. As the absolute value of κ^b increases, the energy of localized states increases until the old state collapses and a new one with lower energy forms.

Figure 3.15 shows the energies of various topological solitons as a function of the parameter κ^b. For $\kappa^b > -0.6$, the toron has the lowest energy among the considered quasiparticles. The energy of the toron increases with $|\kappa^b|$, and the transverse size decreases, leading to its elongation along the z-axis. At approximately $\kappa^b = -0.6$, the toron becomes unstable and transitions into the conical phase. Despite the energy of the skyrmion tube being higher than that of the toron, it remains locally stable up to higher values of $|\kappa^b|$. With further increases in $|\kappa^b|$, its central part becomes thinner. The tube loses stability at approximately $\kappa^b = -1.45$ and breaks down into a pair of chiral bobbers located near the upper and lower boundary surfaces.

Leeches and torons have the same threshold value $|\kappa^b|$ above which they become unstable. Above this threshold, leeches transform into single bobbers, whereas torons disappear.

It should be noted that, as shown in Figure 3.15, the doubled energy of a single chiral bobber is significantly less than the energy of a pair of bobbers formed by the decay of the skyrmion tube. It can be shown that the energy of a pair of bobbers

as a function of the distance separating them has two local minima. One of the minima at a cell thickness d corresponds to a metastable state, while the energy minimum at a greater distance (estimated to be approximately $3.6d$) is lower than the doubled energy of a single bobber.

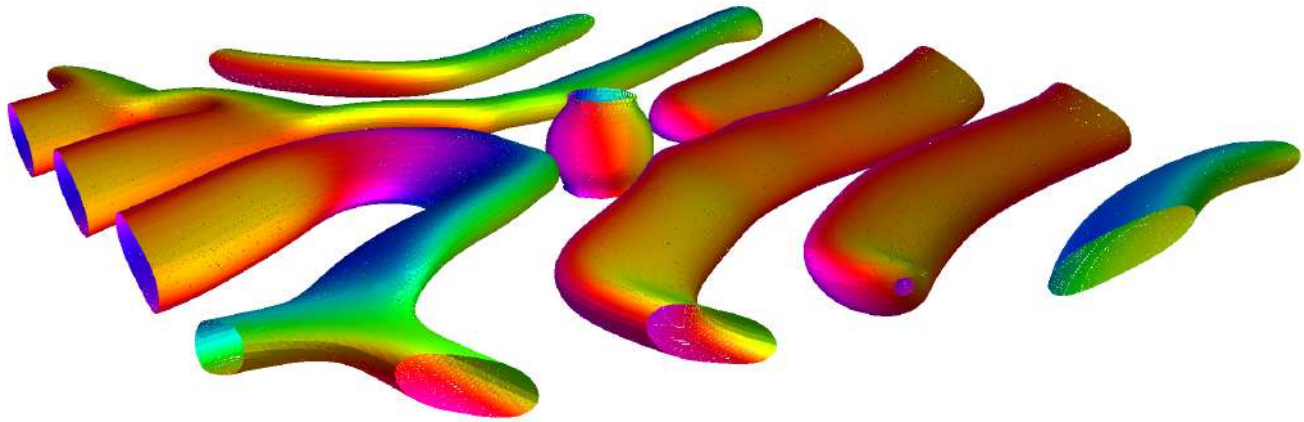

Figure 3.16. Skyrmion embedded in the structure of an oblique fingerprint. The surface corresponds to the value $m_z = 0$. $\kappa^b = 0$, $\kappa^s = 18$. The orientation of the magnetic moments in the xy plane is color-coded.

In the region of the phase diagram where the ground state is the tilted helix (marked in yellow in Figure 3.14), localized topological structures can be embedded in the fingerprint structures. Examples of such configurations for the skyrmion tube and the toron are shown in Figures 3.16 and 3.17, respectively. The figures show surfaces where $m_z = const$. The color codes the azimuthal angle. When the skyrmion tube and the toron are surrounded by the ferromagnetic phase, their structure is entirely analogous to the corresponding configurations in a homeotropic LC cell.

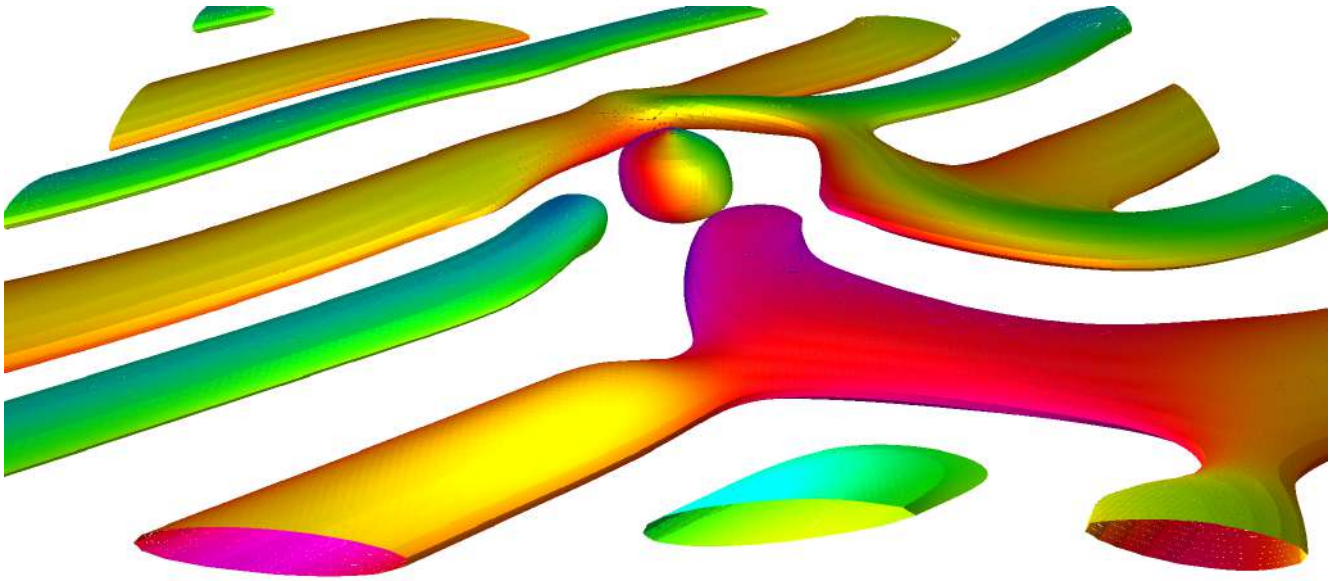

Figure 3.17. Toron embedded in the structure of an oblique fingerprint. The surface corresponds to constant $m_z = -0.1$. $\kappa^b = -0.05$, $\kappa^s = 24$. The color codes the direction of the magnetic moment projection in the xy plane.

Conclusions for Chapter 3. In LC and magnetic systems under confined geometry conditions, such as thin films, it is possible to form various equilibrium and metastable phases, including helical and conical structures, tilted helical states, as well as localized topological solitons. The phase diagram of states of magnetic and LC configurations as a function of internal and surface anisotropy was studied. It was shown that topological solitons can be embedded in larger domain patterns and transform from one type to another under changing external conditions and system parameters.

Chapter 4

Skyrmion States in Thin Films of Cubic Helimagnets

Topologically protected three-dimensional magnetic structures discovered in MnSi and other helimagnets are of interest for numerous technological applications, including magnetic memory and data processing devices. This chapter presents the results of research on the stability and properties of chiral magnetic skyrmions in thin films of cubic helimagnets, the influence of external fields, and the geometry of the sample. Unlike the system studied in Chapter 3, the Zeeman contribution to the energy (1.3) will be explicitly included here. The effect of anisotropy and the presence of surfaces on the formation of skyrmion lattices will be considered.

There are two mechanisms that can be associated with the stability of skyrmion structures in the systems under consideration. In the first mechanism, the anisotropy of the ground state (conical phase) and small anisotropic deformations play a key role in stabilizing skyrmions. In the second mechanism, changes caused by surface layers and interfaces play an important role.

The differences in the phase diagrams of thin films and bulk samples of MnSi will be discussed, with an emphasis on the influence of uniaxial anisotropy of the "easy-plane" type. This allows for the identification of conditions under which it is possible to have skyrmion tubes in the plane, as well as orthogonal to the plane of the film, and to evaluate their stability and the ability to control states using magnetic fields.

In addition, theoretical studies of the tilted helix introduced in Section 3.2 for systems without the Zeeman contribution to the energy will be presented. This structure can exist in thin films but is absent in bulk cubic helimagnets. The tilted helix state will be considered in terms of its equilibrium parameters and the possibility of

transitioning to other magnetic configurations.

4.1. Phase Diagram of a Helimagnet Film. States in an In-Plane Magnetic Field

To describe the orientation of magnetization in the system, we introduce, as before, the unit vector $\mathbf{m} = (\sin\theta\cos\phi, \sin\theta\sin\phi, \cos\theta)$ along the magnetization, $\mathbf{M} = \mathbf{m}M$. To the energy functional ((1.1)), we add the contribution related to the presence of a magnetic field $\mathbf{H}$, $-\mu_0 M(\mathbf{m}\cdot\mathbf{H})$. Both orientations of the applied field will be investigated: orthogonal to the plane ($\mathbf{H} \parallel z$) and in the plane ($\mathbf{H} \perp z$).

We introduce the characteristic length $L_D = \mathcal{A}/|\mathcal{D}|$. The value $4\pi L_D$ represents the helical period for bulk helimagnets in the absence of an external magnetic field and anisotropy. For bulk $MnSi$, this period is about 18 nm. We will measure all lengths in units of L_D. We define the critical field $\mu_0 H_D = \mathcal{D}^2/(\mathcal{A}M)$. For the conical phase in bulk helimagnets, the saturation field, at which all magnetic moments align along the field, is $H_D/2$. The dimensionless governing parameters on which the magnetic configurations depend will be the reduced magnetic field $h = H/H_D$ and the magnitude of the dimensionless uniaxial anisotropy $k_u = \mathcal{K}\mathcal{A}/\mathcal{D}^2$.

We neglect the effects caused by the spatial inhomogeneity of the induced anisotropy. The film will be considered infinite in the x and y directions, using periodic boundary conditions. The film thickness will be chosen as $L = 1.2L_D$, allowing us to work with only one row of skyrmions in the plane. We introduce coordinates such that the film is bounded by parallel planes at $z = \pm 0.6L_D$.

By analogy with the method used in Chapter 3, phase diagrams of states can be constructed based on the equilibrium energies of one-dimensional helical states, two-dimensional skyrmion lattices, and polarized ferromagnetic (FM) states depending on the values of (k_u, h_x) (Figure 4.1(a)) and (k_u, h_z) (Figure 4.1(b)). Regions of modulated states corresponding to the global minimum of the energy functional

are marked with different colors. Note that the FM state, with magnetization along the magnetic field in the plane (white area in Figure 4.1(a)), acquires an in-plane twist (colored plot for $h_x = 0.4$ in Figure 4.2(a)), which never fully saturates [72]. For a magnetic field orthogonal to the plane of the film, the FM state becomes fully saturated [73] (white area in Figure 4.1(b)) as a result of the transition from the conical state at the critical field $h_{z_0} = \frac{1+4k_u}{2}$.

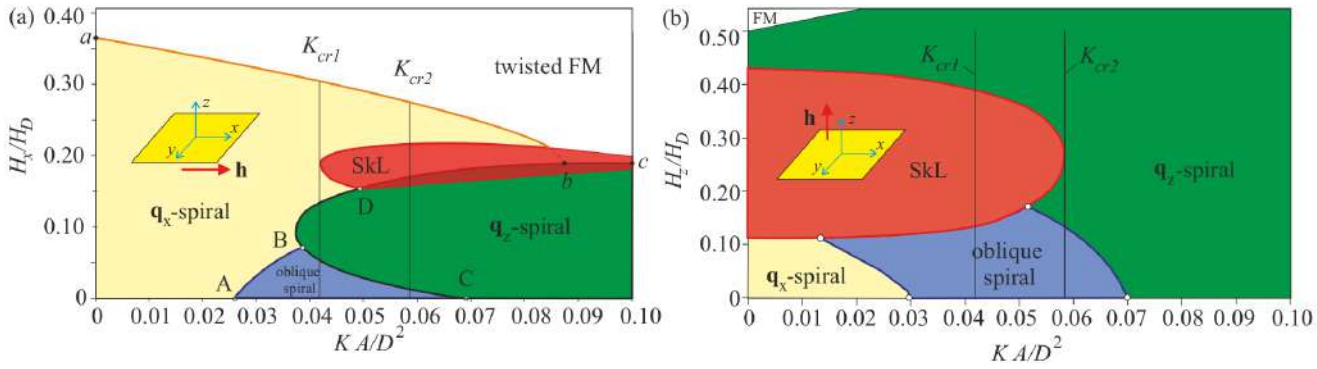

Figure 4.1. Phase diagrams of states on the (k_u, h_x) (a) and (k_u, h_z) (b) planes. Regions of different colors correspond to the skyrmion lattice (red), q_x-helices (yellow), q_z-helices (green), and the oblique helix (blue). The white area in (a) denotes the FM state with in-plane twists, while in (b) it denotes the FM state fully saturated by the field. Critical anisotropy values indicate the overlap interval $[K_{cr1}, K_{cr2}]$ with coexisting skyrmions in the plane and orthogonal to the plane.

In Figure 4.1(a), q_x-helices occupy the yellow-colored region of the phase diagram. For $h_x = k_u = 0$, due to additional twists in the magnetic structure in the surface plane, such helices have lower energy than q_z-helices. Thus, a distinguishing feature of the phase diagram in the 0–A region is the balance of energy associated with the "easy-plane" uniaxial anisotropy and the energy of surface twists, making this structure preferable to other one-dimensional states. For bulk helimagnets, point A shifts to zero on the phase diagram, as shown in Figure 2 in [74].

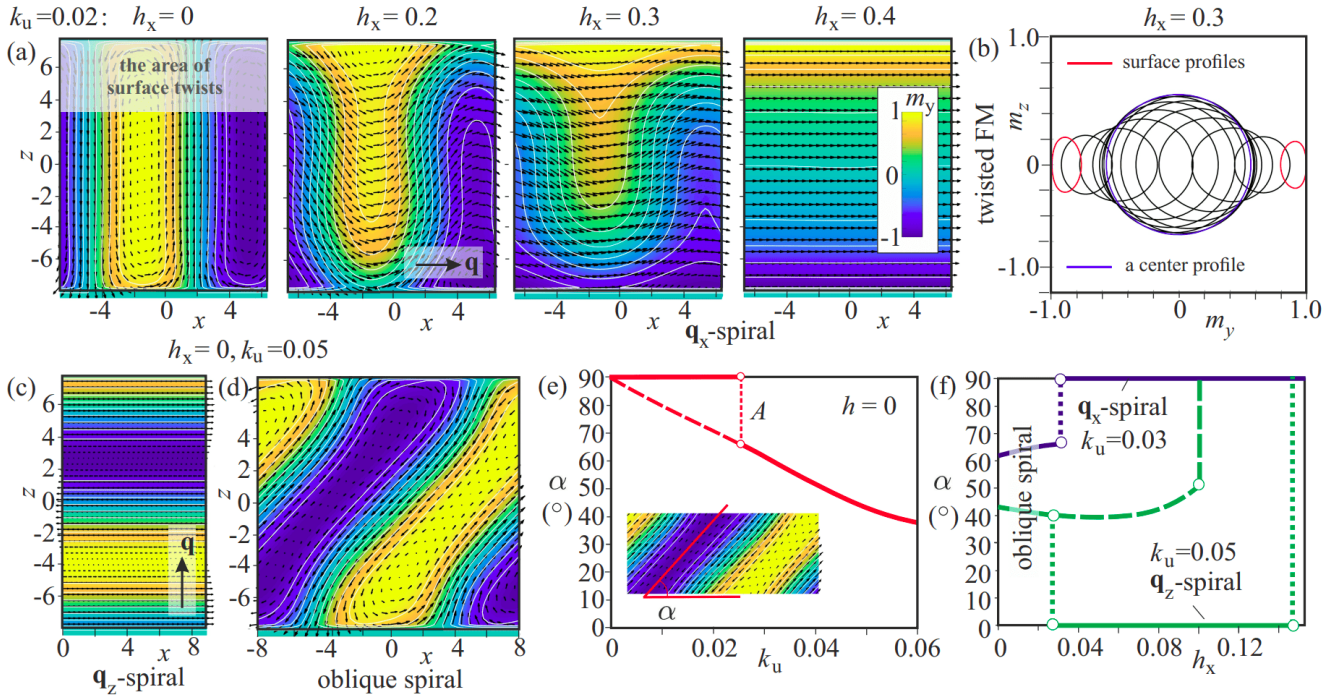

Figure 4.2. One-dimensional helical states for a magnetic field in the plane of the film. The m_y-component of magnetization is color-coded; m_x and m_z are shown with thin black arrows. (a): Field-induced transformation of the q_x-helix into a twisted FM state. (b): A set of m_y-m_z profiles through the film thickness: the blue line represents the profile in the middle layer ($z = 0$), and the red curves at both surfaces ($z = \pm L/2$). (c): The q_z-helix has only one loop of magnetization rotation, which unwinds through a transition into a twisted FM state (line b – c in Figure 4.1(a) or into a q_x-helix (line B-D-b on the phase diagram). At $h_x = 0$ (at point A in Figure (e), the q_x-helix forms an oblique helix (d) with a defined tilt angle α (e), which smoothly decreases with k_u up to the transition into a q_z-helix. (f): Evolution of the oblique helix under the field for $k_u = 0.03$ (blue curves) and $k_u = 0.05$ (green curves) with transitions into conventional conical and helical states.

The transformation of the q_x-helix into a twisted FM state along the line a - b (Figure 4.1(a)) under the influence of the field is shown in Figure 4.2 with the q-vector. In addition to such a twisted structure in the xz plane, which includes conical rotation in the middle of the film with distortions caused by the presence of a surface, uniaxial anisotropy causes slight elliptical deformations of the q_x-helices in the yz plane.

In Figure 4.2(b), the magnetization rotation when moving from the middle layer (blue curve) to the limiting surfaces (red curves) is visible. In this geometry, q_z-helices oriented perpendicular to the field are energetically preferred in the green region of the phase diagram (Figure 4.1(a)). Since the film thickness is usually not

a multiple of the helix wavelength (in our case $1.2L_D$), the magnetization of the q_z-helix has an uncompensated value even in a zero magnetic field. Solutions for this field-twisted helix can be obtained from the known differential equations for a nonlinear pendulum [75, 76]. Experimentally, a set of first-order phase transitions associated with the unwinding processes of helical loops in an applied magnetic field has been identified [72]. The line b – c indicates the corresponding transition between the q_z-helix (Figure 4.2(c)) and the twisted FM state. In the rest of the green region of the phase diagram, such phase transitions are absent. However, along the transition line B – D – b, the twisted FM state should acquire a texture and transform into the q_x-helix shown in Figure 4.2(a) (contour plots for $h_x = 0.2, 0.3$). Along the line B – C, at the first-order phase transition, the q_z-helix acquires a tilt.

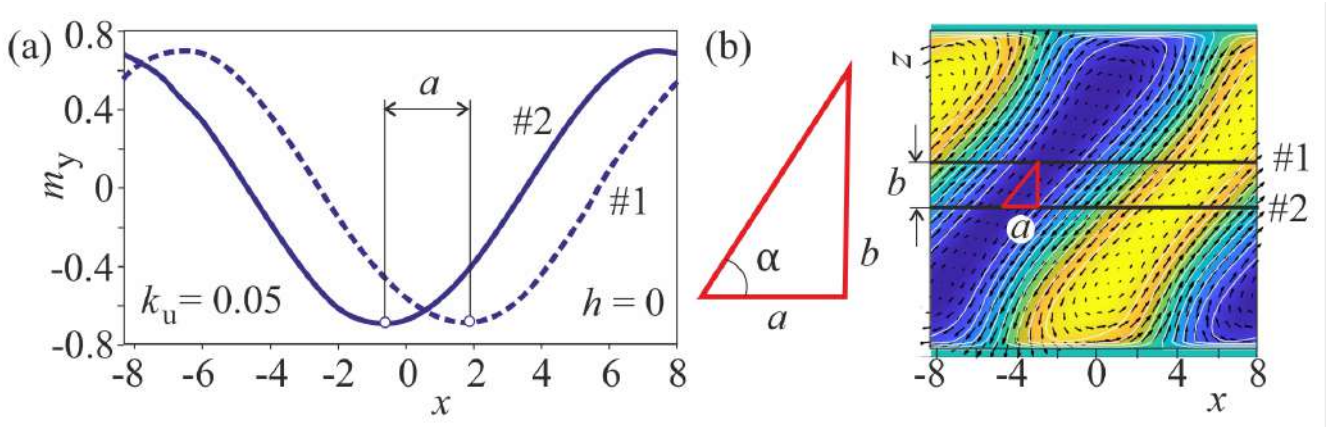

Figure 4.3. Procedure for determining the tilt angle for the oblique helix state.

The thin-film geometry also allows for a stable oblique helix (Figure 4.2(d)), the tilt of which is determined by the energy of surface twists and the contribution of "easy-plane" anisotropy. While the negative energy associated with surface effects remains almost unchanged, the tilt leads to a reduction in anisotropy energy. The tilt angle α at $h_x = 0$ (Figure 4.2(d)) decreases monotonically with increasing uniaxial anisotropy. The angle α is determined in Figure 4.3. However, up to point A (dashed line), the oblique helix is a metastable solution compared to the "straight" helix (solid line). At $k_u = 0.069$, the oblique helix transforms into the q_z-helix

with $\alpha = 0$. Figure 4.2(e) shows the evolution of the tilt angle under the field for $k_u = 0.03$ (blue curves) and $k_u = 0.05$ (green curves), which demonstrates sharp jumps between the corresponding stable helical states (solid lines).

Moreover, for $k_u = 0.05$, the field-driven evolution can occur along two different paths. The first option is shown by the dashed and solid green lines: the oblique helix jumps to the q_z-helix with $\alpha = 0$, which eventually transforms into the q_x-helix with $\alpha = 90°$. All transitions occur at the boundaries of the corresponding stability regions on the phase diagram (Figure 4.1(a)). However, in the second option (shown by the green dashed line), the oblique helix can persist as a metastable state and then directly transition into the q_x-helix, bypassing the q_z-helix region. For both field directions, the stability region of this helix is quite large and located in close proximity to other helical states. This may be the reason why such a state has not yet been identified experimentally: the first-order phase transition of this helix to the conical state can be easily misinterpreted as a magnetization process associated with the q_z-helix.

4.2. Skyrmion-Type Magnetic States in a Helimagnet Film in a Magnetic Field

In the case of an in-plane magnetic field, skyrmions are confined by the boundaries that stabilize them. In such a geometry, surface vortex states have little effect on the internal structure of the skyrmions.

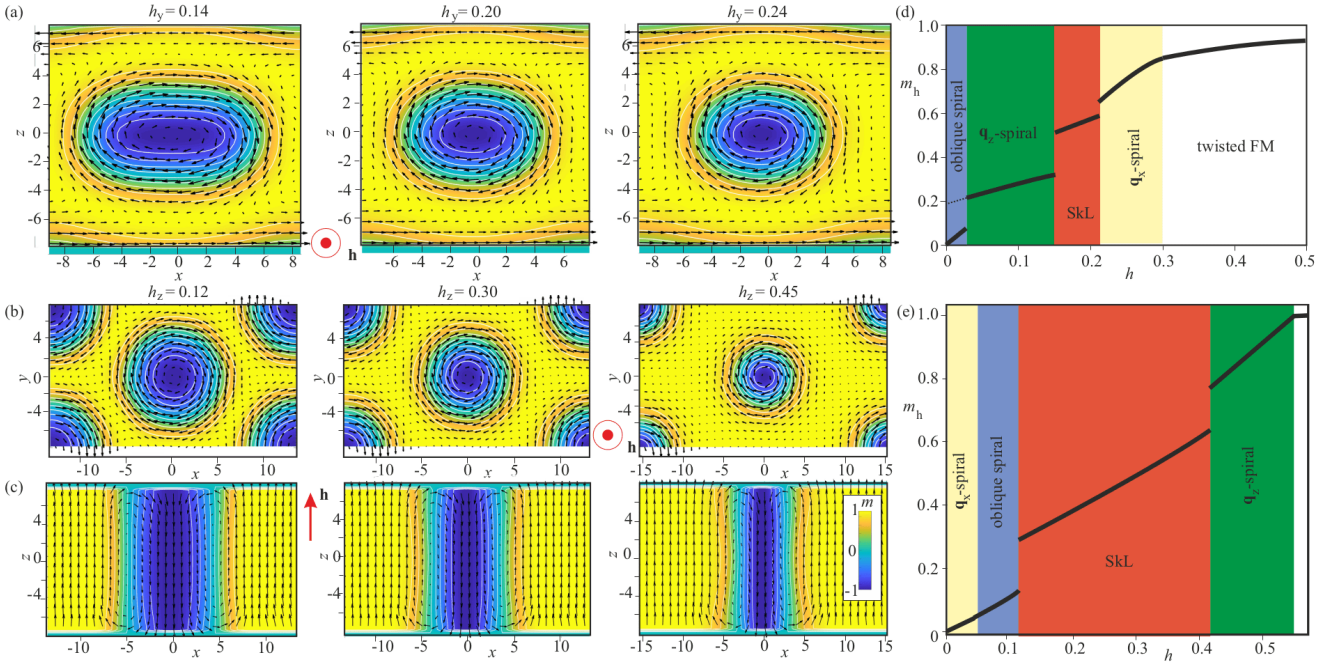

Figure 4.4. The magnetic structure of skyrmions with $k_u = 0.05$ in the plane of the film (a) is characterized by elliptical instability in a magnetic field. Skyrmion lattices consisting of skyrmion tubes orthogonal to the plane of the film with $k_u = 0.025$ (b), (c) exhibit an increase in period with increasing field. Their internal structure is illustrated in two mutually perpendicular planes: xy (b) and xz (c). Magnetization curves as a function of the applied magnetic field $\mathbf{m} - h$ for in-plane (d) and out-of-plane (e) fields show jumps at phase transition lines, corresponding to phase boundaries in Figure 4.1.

Due to the "easy-plane" xy anisotropy, skyrmions experience elliptical instability (Figure 4.4(a)). As a result, they are stable only within a rather narrow range of parameters (red region in Figure 4.1(a)). Typically, skyrmions arranged in several rows occupy the cross-section of the film [77]. Thus, with changes in the magnetic field in the skyrmion phase, the system will exhibit a cascade of first-order phase transitions between states with different numbers of skyrmions [77].

In the case of a magnetic field perpendicular to the plane, the appearance of skyrmions and q_x-helices is characteristic [78, 79]. These solutions can be considered as a superposition of the corresponding solutions in bulk helimagnets and specific twist changes near the surfaces.

At $k_u = 0$, the following first-order phase transitions were identified on theoretical phase diagrams for thin layers of cubic helimagnets: from q_x-helix to skyrmion

lattice, from skyrmion lattice to q_z-helix, and from q_z-helix to ferromagnetic (FM) state [79, 80]. We will not consider the areas of phase diagrams related to various surface states such as chiral bobbers and/or stacked helices [80]. At $k_u = 0.02$, there are two additional transitions: from oblique helix to skyrmion lattice and from q_x-helix to oblique helix. However, the latter transition is hardly identifiable on the magnetization curves (Figure 4.4(d)).

It was predicted that in freestanding layers, skyrmion lattices exist up to very large film thicknesses ($L/4\pi L_D \simeq 8$) [79, 81]. However, experimentally, in wedge-shaped FeGe samples, skyrmion lattices were observed only at thicknesses less than 130 nm, which is less than 2 in units of $4\pi L_D$. The reduction in surface effects was explained by the temperature dependence of the material parameters. In epitaxial MnSi(111)/Si(111) systems, on the contrary, good agreement was observed between numerical modeling taking surface effects into account and experimental implementation [72]. Thus, the influence of surface effects on skyrmion tubes orthogonal to the film planes can also contribute to their stability [79, 81].

The overlap interval $[K_{\mathrm{cr1}}, K_{\mathrm{cr2}}]$ also indicates that skyrmions can exist in the presence of tilted magnetic fields. This suggests an experimental strategy for observing skyrmions that are not in the plane of the film: gradually change the direction of the magnetic field while maintaining its magnitude. If in-plane skyrmion states are stable for an in-plane field, changing the field direction will lead to a transition to the "out-of-plane" states. It is also possible to form skyrmion clusters with mutually orthogonal skyrmion tubes, similar to structures recently described in chiral liquid crystals [69, 81].

Thermodynamically stable skyrmions can also be induced under conditions where the magnetic field is not in the plane of the film. To suppress the influence of the surface, relatively large values of the "easy-plane" anisotropy ($k_u > 0.058$, i.e., greater than the critical value K_{cr2}) are required, compared to, for example, the anisotropy necessary for the stability of elliptically distorted in-plane skyrmions

($k_u > 0.042$, i.e., greater than the critical value K_{cr1}). Thus, both types of skyrmion lattices can coexist within a certain range of anisotropy parameters $[K_{\text{cr1}}, K_{\text{cr2}}] = [0.042, 0.058]$. However, further analysis is required to understand the evolution of phase diagrams with changing film thickness.

As the thickness of the film increases, the influence of surface twists decreases, which can lead to a reduction in the stability region of skyrmions for magnetic fields not in the plane of the sample, and the value of K_{cr2}. At the same time, the value of k_u due to tensile deformation may also decrease, making the realization of "out-of-plane" skyrmions possible even at relatively large film thicknesses. The influence of demagnetizing fields, which was neglected in the calculations presented above, should also be considered, especially for cases of magnetic field orientation orthogonal to the film.

In conclusion, the calculations showed the existence of a new spiral magnetic configuration at low field values, located between the usual conical and helicoidal states, stable in a wide range of parameters. This oblique helix differs from previously known magnetic structures present in the phase diagrams of bulk helimagnets. Its detailed study, control, and development of methods for managing the tilt of the helix may allow for the creation of new topological magnetic defects, such as isolated skyrmions, possessing unique static and dynamic properties.

The obtained results emphasize the important role of magnetic anisotropy and vortex magnetic surface states in stabilizing skyrmion configurations of various orientations and can be used to control the structure and properties of skyrmions in real experiments, such as in epitaxial thin films MnSi(111)/Si(111). Recent experiments with mechanically stressed helimagnets FeGe [82] with collectivized electronic states demonstrate the potential role of tensile deformation in creating and managing magnetic solitonic textures, providing an opportunity to test the theoretical concepts presented in this chapter in this system.

Conclusions for Chapter 4. The study of thin films of cubic helimagnets showed

that the stabilization of skyrmion and spiral structures depends on anisotropy and the orientation of the magnetic field. When the magnetic field is oriented in the plane of the film, skyrmions exhibit elliptical instability and exist only in a narrow range of parameters. When the field is oriented perpendicular to the surface, various magnetic structures, including skyrmion tubes with an axis out of the plane, can exist at significantly greater film thicknesses.

Conclusion

In the course of the work, systems of magnets and liquid crystals with energies that are functionals dependent on one, two, and three coordinates were considered. For the case where the energy functional can be reduced to a one-dimensional form, tasks related to studying the influence of boundary conditions on the state of the system were considered: a method for determining the Frank modules of liquid crystals based on lanthanoid complexes was found from the dependence of the dielectric permittivity of a liquid crystal cell on the applied magnetic field, under the condition of soft boundary conditions and a nontrivial initial anchoring angle. The hysteresis in the transition between states in a chiral system was found and explained, and the types of anchoring break were studied. For the two-dimensional case, the behavior of a thin layer of liquid crystal/multilayer magnetic system was studied, and the main states of such a system were found depending on the parameters of the applied field and the strength of the anchoring to the surface of the cell/anisotropy in the volume and on the surface of the magnet. Both previously known states, such as cones and spirals along the x and z axes, and a new state—a tilted spiral: a spiral with an axis deviating from the z axis by an angle α—were found and described.

Acknowledgements

The author expresses deep gratitude to his scientific advisor, Prof. Uzdin V.M. The author also expresses gratitude to Lobanov I.S. and Aksyonova E.V. for fruitful cooperation. The author thanks his parents and wife for their support.

Bibliography

1. The 2020 Skyrmionics Roadmap / C. Back, V. Cros, H. Ebert [at al.] // Journal of Physics D: Applied Physics. 2020. . T. 53, № 36. C. 363001.
2. Control of Light by Topological Solitons in Soft Chiral Birefringent Media / Andrew J. Hess, Guilhem Poy, Jung-Shen B. Tai [at al.] // Physical Review X. 2020. . T. 10, № 3. C. 031042.
3. Kos Žiga, Dunkel Jörn. Nematic Bits and Universal Logic Gates // Science Advances. 2022. . T. 8, № 33. C. eabp8371.
4. Wu Jin-Sheng, Smalyukh Ivan I. Hopfions, Heliknotons, Skyrmions, Torons and Both Abelian and Nonabelian Vortices in Chiral Liquid Crystals // Liquid Crystals Reviews. 2022. . T. 10, № 1-2. C. 34–68.
5. Editorial: Nucleation and Stability of Exotic Solitons in Condensed Matter / Valery M. Uzdin, Danny Thonig, Börge Göbel [at al.] // Frontiers in Physics. 2023. . T. 11.
6. Lifetime of Skyrmions in Discrete Systems with Infinitesimal Lattice Constant / M. N. Potkina, I. S. Lobanov, H. Jónsson [at al.] // Journal of Magnetism and Magnetic Materials. 2022. . T. 549. C. 168974.
7. Stability of Magnetic Skyrmions: Systematic Calculations of the Effect of Size from Nanometer Scale to Microns / M. N. Potkina, I. S. Lobanov, H. Jónsson [at al.] // Physical Review B. 2023. . T. 107, № 18. C. 184414.
8. Лобанов И. С., Поткина М. Н., Уздин В. М. УСТОЙЧИВОСТЬ И ВРЕМЕНА ЖИЗНИ МАГНИТНЫХ СОСТОЯНИЙ НАНО- И МИКРОСТРУКТУР (МИНИОБЗОР) // ПИСЬМА В ЖУРНАЛ ЭКСПЕРИМЕНТАЛЬНОЙ И ТЕОРЕТИЧЕСКОЙ ФИЗИКИ. 2021. Т. 113, № 11-12(6). С. 833–847.
9. Bessarab Pavel F, Uzdin Valery M, Jónsson Hannes. Harmonic Transition-State Theory of Thermal Spin Transitions // Physical Review B. 2012. Т. 85, № 18. С. 184409.

10. Energy Surface and Minimum Energy Paths for Fréedericksz Transitions in Bistable Cholesteric Liquid Crystals / A. V. Ivanov, P. F. Bessarab, E. V. Aksenova [at al.] // Physical Review E. 2016. Т. 93, № 4. С. 042708.
11. Multiple Minimum-Energy Paths and Scenarios of Unwinding Transitions in Chiral Nematic Liquid Crystals / Semen S Tenishchev, Alexei D Kiselev, Aleksei V Ivanov [at al.] // Physical Review E. 2019. Т. 100, № 6. С. 062704.
12. Electric-Field-Induced Nematic-Cholesteric Transition and Three-Dimensional Director Structures in Homeotropic Cells / Ivan I Smalyukh, BI Senyuk, P Palffy-Muhoray [at al.] // Physical Review E. 2005. Т. 72, № 6. С. 061707.
13. Topological Structures in Chiral Media: Effects of Confined Geometry / IM Tambovtsev, AO Leonov, IS Lobanov [at al.] // Physical Review E. 2022. Т. 105, № 3. С. 034701.
14. Stability of In-Plane and out-of-Plane Chiral Skyrmions in Epitaxial MnSi(111)/Si(111) Thin Films: Surface Twists versus Easy-Plane Anisotropy / Andrey O. Leonov, Ivan M. Tambovtcev, Igor S. Lobanov [at al.] // Phys. Rev. B. 2020. . Т. 102, № 17. С. 174415.
15. Hysteresis and Fréedericksz Thresholds for Twisted States in Chiral Nematic Liquid Crystals: Minimum-energy Path Approach / Semen S Tenishchev, Ivan M Tambovtcev, Alexei D Kiselev [at al.] // Journal of Molecular Liquids. 2021. Т. 325. С. 115242.
16. Magnetic Field-Induced Macroscopic Alignment of Liquid-Crystalline Lanthanide Complexes / Elena Aksenova, Liliya Dobrun, Alexander Kovshik [at al.] // Crystals. 2019. Т. 9, № 10. С. 499.
17. Frank Constants Calculation Method for Erbium-Based Liquid Crystal / I Tambovtcev, E Aksenova, L Dobrun [at al.] // Journal of Physics: Conference Series. Т. 1560. IOP Publishing, 2020. С. 012036.
18. Тамбовцев И.М. Добрун Л.А. Ковшик А.П. Аксенова Е.В. Рюмцев Е.И. МЕТОД РАСЧЁТА МОДУЛЕЙ ФРАНКА ЖИДКОКРИСТАЛЛИЧЕСКОГО

КОМПЛЕКСА НА ОСНОВЕ ЭРБИЯ // Вестник МГОУ. 2020. Т. 3. С. 6–12.

19. The Physics of Liquid Crystals / P. G. de Gennes, J. Prost, P. G. de Gennes [at al.]. International Series of Monographs on Physics. Second Edition, Second Edition изд. Oxford, New York: Oxford University Press, 1995. .
20. Lobanov I. S., Potkina M. N., Uzdin V. M. Stability and Lifetimes of Magnetic States of Nano- and Microstructures (Brief Review) // JETP Letters. 2021. . Т. 113, № 12. С. 801–813.
21. Mesomorphic Behaviour and Luminescent Properties of Mesogenic-Diketonate Lanthanide Adducts with 5, 5'-Di (Heptadecyl)-2, 2'-Bipyridine / Andrey A Knyazev, Elena Yu Molostova, Aleksandr S Krupin [at al.] // Liquid Crystals. 2013. Т. 40, № 7. С. 857–863.
22. Hakemi H, Jagodzinski EF, DuPre DB. The Determination of the Elastic Constants of a Series of N-Alkylcyanobiphenyls by Anisotropy of Turbidity // The Journal of Chemical Physics. 1983. Т. 78, № 3. С. 1513–1518.
23. Bogi A, Faetti Sandro. Elastic, Dielectric and Optical Constants of 4'-Pentyl-4-Cyanobiphenyl // Liquid crystals. 2001. Т. 28, № 5. С. 729–739.
24. Bradshaw MJ, Raynes EP. Pre-Transitional Effects in the Electric Permittivity of Cyano Nematics // Molecular Crystals and Liquid Crystals. 1981. Т. 72, № 2-3. С. 73–78.
25. Determination of the Frank Elastic Constant Ratios in Nematic Liquid Crystals (nCB) by Observing Angular Dependence of Rayleigh Light Scattering Intensity / Masahiko Hara, Jun-Ichi Hirakata, Takehiro Toyooka [at al.] // Molecular Crystals and Liquid Crystals. 1985. Т. 122, № 1. С. 161–168.
26. Srivastava Amit, Singh Shri. Elastic Constants of Nematic Liquid Crystals of Uniaxial Symmetry // Journal of Physics: Condensed Matter. 2004. Т. 16, № 41. С. 7169.
27. Deuling Heinz J. Deformation of Nematic Liquid Crystals in an Electric Field // Molecular Crystals and Liquid Crystals. 1972. Т. 19, № 2. С. 123–131.

28. Cheng Julian, Thurston RN, Berreman DW. Boundary-Layer Model of Field Effects in a Bistable Liquid-Crystal Geometry // Journal of Applied Physics. 1981. T. 52, № 4. C. 2756–2765.
29. Oswald P, Baudry J, Pirkl S. Static and Dynamic Properties of Cholesteric Fingers in Electric Field // Physics Reports. 2000. T. 337, № 1-2. C. 67–96.
30. New Type of Stable Particlelike States in Chiral Magnets / F. N. Rybakov, A. B. Borisov, S. Blügel [at al.] // Physical Review Letters. 2015. T. 115. C. 117201.
31. Tai Jung-Shen B, Smalyukh Ivan I [at al.]. Surface Anchoring as a Control Parameter for Stabilizing Torons, Skyrmions, Twisted Walls, Fingers, and Their Hybrids in Chiral Nematics // Physical Review E. 2020. T. 101, № 4. C. 042702.
32. Polarized Luminescence from Aligned Samples of Nematogenic Lanthanide Complexes / Yury G Galyametdinov, Andrey A Knyazev, Vagif I Dzhabarov [at al.] // Advanced materials. 2008. T. 20, № 2. C. 252–257.
33. Mulet Xavier, Boyd Ben J, Drummond Calum J. Advances in Drug Delivery and Medical Imaging Using Colloidal Lyotropic Liquid Crystalline Dispersions // Journal of colloid and interface science. 2013. T. 393. C. 1–20.
34. Dzhabarov V. I. Synthesis, Phase Behavior, Magnetic and Optical Properties of Tris(Beta-Diketonates) Lanthanum Nematic Adducts with the Lewis Bases. Ph.D. thesis: Thesis for the degree of candidate of chemical sciences. 2009.
35. Magnetic Alignment Study of Rare-Earth-Containing Liquid Crystals / Yury G Galyametdinov, Wolfgang Haase, Bart Goderis [at al.] // The Journal of Physical Chemistry B. 2007. T. 111, № 50. C. 13881–13885.
36. Anisotropy of the Magnetic Susceptibility of Mesogeneous Lanthanide Complexes / VI Dzhabarov, AA Knyazev, VF Nikolaev [at al.] // Russian Journal of Physical Chemistry A. 2011. T. 85, № 8. C. 1450–1453.
37. Meyerhofer D. Field Induced Distortions of a Liquid Crystal with Various Surface Alignments // Physics Letters A. 1975. T. 51, № 7. C. 407–408.

38. Effect of an Electric Field on the Orientation of a Liquid Crystal in a Cell with a Nonuniform Director Distribution / EV Aksenova, AA Karetnikov, NA Karetnikov [at al.] // Journal of Experimental and Theoretical Physics. 2016. T. 122, № 5. C. 942–949.
39. Pikin S. A. Structural Transformations in Liquid Crystals. Gordon and Breach Science Publishers, 1991.
40. Stewart Iain W. The Static and Dynamic Continuum Theory of Liquid Crystals: A Mathematical Introduction. Crc Press, 2019.
41. Brown CV, Mottram NJ. Influence of Flexoelectricity above the Nematic Fréedericksz Transition // Physical Review E. 2003. T. 68, № 3. C. 031702.
42. Laser Trapping of Low Refractive Index Colloids in a Nematic Liquid Crystal / M Škarabot, M Ravnik, D Babič [at al.] // Physical Review E. 2006. T. 73, № 2. C. 021705.
43. Structural Changes in the 6CHBT Liquid Crystal Doped with Spherical, Rodlike, and Chainlike Magnetic Particles / Peter Kopčanskỳ, Natalia Tomašovičová, Martina Koneracká [at al.] // Physical Review E. 2008. T. 78, № 1. C. 011702.
44. Light-and Electric-Field-Induced First-Order Orientation Transitions in a Dendrimer-Doped Nematic Liquid Crystal / EA Babayan, IA Budagovsky, SA Shvetsov [at al.] // Physical Review E. 2010. T. 82, № 6. C. 061705.
45. Makarov DV, Zakhlevnykh AN. Tricritical Phenomena at the Fréedericksz Transition in Ferronematic Liquid Crystals // Physical Review E. 2010. T. 81, № 5. C. 051710.
46. Bevilacqua Giuseppe, Napoli Gaetano. Periodic Splay-Twist Fréedericksz Transition for Nematics Confined between Two Concentric Cylinders // Physical Review E. 2010. T. 81, № 3. C. 031707.
47. Shelestiuk Sergii M, Reshetnyak Victor Yu, Sluckin Timothy J. Frederiks Transition in Ferroelectric Liquid-Crystal Nanosuspensions // Physical Review

E. 2011. T. 83, № 4. C. 041705.

48. Chernyshuk SB, Tovkach OM, Lev BI. Theory of Elastic Interaction between Colloidal Particles in a Nematic Cell in the Presence of an External Electric or Magnetic Field // Physical Review E. 2012. T. 85, № 1. C. 011706.
49. Rapini A, Papoular M. Distorsion d'une Lamelle Nématique Sous Champ Magnétique Conditions d'ancrage Aux Parois // Le Journal de Physique Colloques. 1969. T. 30, № C4. C. C4–54.
50. Thurston RN, Berreman DW. Equilibrium and Stability of Liquid-Crystal Configurations in an Electric Field // Journal of Applied Physics. 1981. T. 52, № 1. C. 508–509.
51. Berreman DW, Heffner WR. New Bistable Liquid-Crystal Twist Cell // Journal of Applied Physics. 1981. T. 52, № 4. C. 3032–3039.
52. Thurston RN. Exact Solutions for Liquid Crystal Configurations and an Improved Boundary Layer Model // Journal of applied physics. 1983. T. 54, № 9. C. 4966–4988.
53. Threshold Behavior and Electro-Optical Properties of Twisted Nematic Layers with Weak Anchoring in the Tilt and Twist Angle / Ralf Hirning, Werner Funk, H-R Trebin [at al.] // Journal of applied physics. 1991. T. 70, № 8. C. 4211–4216.
54. Val'kov A. Yu., Aksenova E. V., Romanov V. P. First-Order and Continuous Fréedericksz Transitions in Cholesteric Liquid Crystals // Phys. Rev. E. 2013. T. 87. C. 022508.
55. Kiselev AD, Sluckin TJ. Twist of Cholesteric Liquid Crystal Cells: Stability of Helical Structures and Anchoring Energy Effects // Physical Review E. 2005. T. 71, № 3. C. 031704.
56. Lobanov IS, Uzdin VM. The Lifetime of Micron Scale Topological Chiral Magnetic States with Atomic Resolution // Computer Physics Communications. 2021. T. 269. C. 108136.
57. Skyrmions and Anomalous Hall Effect in a Dzyaloshinskii-Moriya Spiral

Magnet / Su Do Yi, Shigeki Onoda, Naoto Nagaosa [at al.] // Physical Review B. 2009. . T. 80, № 5. C. 054416.

58. Leonov Andrey O, Bogdanov Alex N, Inoue Katsuya. Toggle-Switch-like Crossover between Two Types of Isolated Skyrmions within the Conical Phase of Cubic Helimagnets // Physical Review B. 2018. T. 98, № 6. C. 060411.
59. Electric-Field Induced Transitions in a Cholesteric Liquid-Crystal Film with Negative Dielectric Anisotropy / EC Gartland, H Huang, OD Lavrentovich [at al.] // Journal of Computational and Theoretical Nanoscience. 2010. T. 7, № 4. C. 709–725.
60. Helicoids in Chiral Liquid Crystals under External Fields / G De Matteis, L Martina, C Naya [at al.] // Physical Review E. 2019. T. 100, № 5. C. 052703.
61. Afghah Sajedeh, Selinger Jonathan V. Theory of Helicoids and Skyrmions in Confined Cholesteric Liquid Crystals // Physical Review E. 2017. T. 96, № 1. C. 012708.
62. Leonov Andrey O, Pappas Catherine, Kézsmárki Istvan. Field and Anisotropy Driven Transformations of Spin Spirals in Cubic Skyrmion Hosts // Physical Review Research. 2020. T. 2, № 4. C. 043386.
63. Bessarab Pavel F, Uzdin Valery M, Jónsson Hannes. Method for Finding Mechanism and Activation Energy of Magnetic Transitions, Applied to Skyrmion and Antivortex Annihilation // Computer Physics Communications. 2015. T. 196. C. 335–347.
64. Truncated Minimum Energy Path Method for Finding First Order Saddle Points / I. S. Lobanov, M. N. Potkina, H. Jónsson [at al.] // Nanosyst. Phys. Chem. Math. 2017. T. 8, № 5. C. 586.
65. Duplication, Collapse, and Escape of Magnetic Skyrmions Revealed Using a Systematic Saddle Point Search Method / Gideon P Müller, Pavel F Bessarab, Sergei M Vlasov [at al.] // Physical review letters. 2018. T. 121, № 19. C. 197202.
66. Lobanov Igor S, Jónsson Hannes, Uzdin Valery M. Mechanism and Activation

Energy of Magnetic Skyrmion Annihilation Obtained from Minimum Energy Path Calculations // Physical Review B. 2016. T. 94, № 17. C. 174418.

67. Energy Surface and Lifetime of Magnetic Skyrmions / Valery M Uzdin, Maria N Potkina, Igor S Lobanov [at al.] // Journal of Magnetism and Magnetic Materials. 2018. T. 459. C. 236–240.
68. Two-Dimensional Skyrmions and Other Solitonic Structures in Confinement-Frustrated Chiral Nematics / Paul J Ackerman, Rahul P Trivedi, Bohdan Senyuk [at al.] // Physical Review E. 2014. T. 90, № 1. C. 012505.
69. Vlasov Sergei M, Uzdin Valery M, Leonov Andrey O. Skyrmion Flop Transition and Congregation of Mutually Orthogonal Skyrmions in Cubic Helimagnets // Journal of Physics: Condensed Matter. 2020. T. 32, № 18. C. 185801.
70. Leonov AO, Inoue K. Homogeneous and Heterogeneous Nucleation of Skyrmions in Thin Layers of Cubic Helimagnets // Physical Review B. 2018. T. 98, № 5. C. 054404.
71. Smalyukh Ivan I. Knots and Other New Topological Effects in Liquid Crystals and Colloids // Reports on Progress in Physics. 2020. T. 83, № 10. C. 106601.
72. Surface Twist Instabilities and Skyrmion States in Chiral Ferromagnets / SA Meynell, MN Wilson, H Fritzsche [at al.] // Physical Review B. 2014. T. 90, № 1. C. 014406.
73. Stabilization of Skyrmion Textures by Uniaxial Distortions in Noncentrosymmetric Cubic Helimagnets / AB Butenko, AA Leonov, UK Rößler [at al.] // Physical Review B. 2010. T. 82, № 5. C. 052403.
74. Chiral Modulations and Reorientation Effects in MnSi Thin Films / EA Karhu, UK Rößler, AN Bogdanov [at al.] // Physical Review B. 2012. T. 85, № 9. C. 094429.
75. Extended Elliptic Skyrmion Gratings in Epitaxial MnSi Thin Films / MN Wilson, EA Karhu, AS Quigley [at al.] // Physical Review B. 2012. T. 86, № 14. C. 144420.

76. Dzyaloshinskii IE. Phys. JETP-USSR 19, 960 (1964) // J. Sov. Phys. JETP-USSR. 1965. T. 20. C. 223.
77. Degeneracies and Fluctuations of Néel Skyrmions in Confined Geometries / Rick Keesman, AO Leonov, P van Dieten [at al.] // Physical Review B. 2015. T. 92, № 13. C. 134405.
78. Rybakov FN, Borisov AB, Bogdanov AN. Three-Dimensional Skyrmion States in Thin Films of Cubic Helimagnets // Physical Review B. 2013. T. 87, № 9. C. 094424.
79. Chiral Surface Twists and Skyrmion Stability in Nanolayers of Cubic Helimagnets / AO Leonov, Yoshihiko Togawa, TL Monchesky [at al.] // Physical review letters. 2016. T. 117, № 8. C. 087202.
80. New Spiral State and Skyrmion Lattice in 3D Model of Chiral Magnets / Filipp N Rybakov, Aleksandr B Borisov, Stefan Blügel [at al.] // New Journal of Physics. 2016. T. 18, № 4. C. 045002.
81. Real-Space Observation of Skyrmion Clusters with Mutually Orthogonal Skyrmion Tubes / Hayley RO Sohn, Sergei M Vlasov, Valeriy M Uzdin [at al.] // Physical Review B. 2019. T. 100, № 10. C. 104401.
82. Metastable Solitonic States in the Strained Itinerant Helimagnet FeGe / Victor Ukleev, Yuichi Yamasaki, Oleg Utesov [at al.] // Physical Review B. 2020. T. 102, № 1. C. 014416.

Appendix

Energy and its variation for liquid crystal systems

Frank's free energy is defined as the integral of the energy density ω over the volume V of the considered liquid crystal (LC):

$$E[\mathbf{n}] = \int_V \omega[\mathbf{n}]\, d\mathbf{x}. \tag{4.1}$$

The variation $\delta E/\delta \mathbf{n}$ of the free energy plays an important role in the dynamics of LCs:

$$E[\mathbf{n} + \varepsilon\delta\mathbf{n}] = E[\mathbf{n}] + \varepsilon \int_V \delta E[\mathbf{n}] \cdot \delta\mathbf{n}\, d\mathbf{x} + o(\varepsilon), \text{ as } \varepsilon \to 0. \tag{4.2}$$

Further, all quantities are assumed to implicitly depend on the spatial coordinates $\mathbf{x}$. The notation a_i is used for the i-th coordinate of the vector $\mathbf{a} = (a_1, a_2, a_3)$, and partial derivatives with respect to the components $\mathbf{x} = (x_1, x_2, x_3)$ are denoted by a comma in the lower indices:

$$a_{i,j} = \frac{\partial a_i}{\partial x_j}. \tag{4.3}$$

The energy E can be represented as the sum of several contributions of the form:

$$F[\mathbf{n}] = \int_V f(\mathbf{n}, \nabla\mathbf{n})\, d\mathbf{x}, \tag{4.4}$$

First, we derive a general rule for the variation of the functional F of the given form:

$$\begin{aligned} F[\mathbf{n} + \varepsilon\delta\mathbf{n}] = \int_V f(\mathbf{n} + \varepsilon\delta\mathbf{n}, \nabla\mathbf{n} + \varepsilon\nabla\delta\mathbf{n})\, d\mathbf{x} = \\ = F[\mathbf{n}] + \varepsilon \int_V \left[\frac{\partial f}{\partial n_i}\delta n_i + \frac{\partial f}{\partial n_{i,j}}\delta n_{i,j}\right] d\mathbf{x} + o(\varepsilon). \end{aligned} \tag{4.5}$$

Summation over repeated indices is implied unless otherwise stated. Integrating

by parts and discarding the integrals over the boundary (appropriate boundary conditions must be established), we get:

$$F[\mathbf{n}+\varepsilon\delta\mathbf{n}]-F[\mathbf{n}]=\varepsilon\int_V\left[\frac{\partial f}{\partial n_i}-\frac{\partial}{\partial x_j}\frac{\partial f}{\partial n_{i,j}}\right]\delta n_i\,d\mathbf{x}+o(\varepsilon). \tag{4.6}$$

Thus, for the variation of F, we have:

$$\delta F_i=\delta\int_V f d\mathbf{x}=\frac{\partial f}{\partial n_i}-\frac{\partial}{\partial x_j}\frac{\partial f}{\partial n_{i,j}}. \tag{4.7}$$

Now, we calculate the variation for each of the terms included in the energy E, then restore the constant factors and write the result by summing all contributions.

We are interested in the variation of $\mathbf{n}$ under the condition $\mathbf{n}(x)^2=1$, which imposes restrictions on the variations $\delta\mathbf{n}$:

$$1=(\mathbf{n}+\varepsilon\delta\mathbf{n})^2=\mathbf{n}^2+2\varepsilon\mathbf{n}\cdot\delta\mathbf{n}+\varepsilon^2\delta\mathbf{n}^2=1+2\varepsilon\mathbf{n}\cdot\delta\mathbf{n}+O(\varepsilon^2). \tag{4.8}$$

Since the variations are small, $\varepsilon\to 0$, the perturbations $\mathbf{n}$ must lie in the tangent space to the constraining manifold:

$$\mathbf{n}(x)\cdot\delta\mathbf{n}(x)=0\ \forall x. \tag{4.9}$$

This means that any component of the variation δE, parallel to $\mathbf{n}$, does not contribute and can be omitted. Moreover, the dynamics of liquid crystals are determined by relaxation, i.e., $d\mathbf{n}/dt=\dot{\mathbf{n}}$ must be antiparallel to $\delta E[\mathbf{n}]$ in the tangent space of the configuration space. Considering that $\mathbf{n}$ is always normalized: $\mathbf{n}^2(x)=1$, δE in the dynamics must be projected onto the tangent space:

$$\lambda\dot{\mathbf{n}}=\delta E-(\delta E\cdot\mathbf{n})\mathbf{n}\ \forall x, \tag{4.10}$$

where λ is some constant ensuring proper time scaling.

The energy of the system is defined in the entire multidimensional state space but has physical meaning only on the constraining manifold $\mathbf{n}(x)^2 = 1$. If the problem is formulated correctly, the dynamics of the system should remain unchanged regardless of how the energy is defined outside the manifold. To check this assumption, consider the addition $\tilde{E} = (1 - \mathbf{n}^2)G(\mathbf{n}, \nabla\mathbf{n})$ to the system's energy, where the vector $\mathbf{n}$ squared is calculated component-wise as $\mathbf{n}^2(x) = \mathbf{n}(x) \cdot \mathbf{n}(x)$, and the function G is smooth. Such an addition $\tilde{E}$ to the energy includes all smooth transformations of the energy that do not change the value of the energy on the constraining manifold.

The variation of the addition $\tilde{E}$ is given as

$$\delta\tilde{E} = -2\mathbf{n}G + (1 - \mathbf{n}^2)\delta G, \tag{4.11}$$

where the first term disappears when projected onto the tangent space, and the second is zero on the constraining manifold. Therefore, changes in energy outside the configuration space do not affect the system's dynamics, which corresponds to expectations. Thus, the formula for the energy can be simplified using arbitrary expressions that preserve the energy values for $\mathbf{n}(x)^2 = 1$.

Energy Calculation

Some contributions to the energy are squares of simpler functions. We derive the variation for the squares $f(\mathbf{n}, \nabla\mathbf{n}) = g(\mathbf{n}, \nabla\mathbf{n})^2$, where g can be a vector function:

$$f = g_p g_p, \quad \frac{\partial f}{\partial n_i} = 2g_p\frac{\partial g_p}{\partial n_i}, \quad \frac{\partial f}{\partial n_{i,j}} = 2g_p\frac{\partial g_p}{\partial n_{i,j}},$$
$$\frac{\partial}{\partial x_j}\frac{\partial f}{\partial n_{i,j}} = 2\frac{dg_p}{dx_j}\frac{\partial g_p}{\partial n_{i,j}} + 2g_p\frac{\partial}{\partial x_j}\frac{\partial g_p}{\partial n_{i,j}}. \tag{4.12}$$

$$\frac{dg_p}{dx_j} = \sum_i \frac{\partial g_p}{\partial n_i} n_{i,j} + \sum_{i,k} \frac{\partial g_p}{\partial n_{i,k}} n_{i,kj}. \tag{4.13}$$

Thus, the variation of the square of a function can be expressed through the variation of the function itself:

$$\delta_i \int_V g^2 \, d\mathbf{x} = 2 g_p \, \delta_i \int_V g_p \, d\mathbf{x} - 2 \sum_j \frac{dg_p}{dx_j} \frac{\partial g_p}{\partial n_{i,j}}. \tag{4.14}$$

In this expression, we used the product rule for differentiation and summation over repeated indices.

(I) Consider $f = \|\nabla \mathbf{n}\|^2 = \sum_{ij} n_{i,j}^2$ and obtain the following derivatives:

$$\frac{\partial f}{\partial n_i} = 0, \quad \frac{\partial f}{\partial n_{k,j}} = 2 n_{k,j}, \quad \sum_j \frac{\partial}{\partial x_j} \frac{\partial f}{\partial n_{k,j}} = 2 \sum_j n_{k,jj}. \tag{4.15}$$

Thus, the variation of the energy functional is expressed as

$$\delta_k \int_V \|\nabla \mathbf{n}\|^2 \, d\mathbf{x} = -2 \sum_j n_{k,jj}, \tag{4.16}$$

or, using vector notation, we can write

$$\delta \int_V \|\nabla \mathbf{n}\|^2 \, d\mathbf{x} = -2 \Delta \mathbf{n}, \tag{4.17}$$

where Δ denotes the Laplacian acting on each component of the vector $\mathbf{n}$.

(II) Consider $g = \nabla \times \mathbf{n}$. The coordinates of the cross product and the curl can be expressed using the Levi-Civita symbols ε_{ijk}:

$$(\mathbf{a} \times \mathbf{b})_k = \varepsilon_{ijk} a_i b_j = \varepsilon_{kij} a_i b_j, \quad (\nabla \times \mathbf{a})_k = \varepsilon_{klm} \frac{\partial}{\partial x_l} a_m = \varepsilon_{klm} a_{m,l}. \tag{4.18}$$

Using the contraction property of the Levi-Civita symbols:

$$\varepsilon_{ijk}\varepsilon_{imn} = \delta_{jm}\delta_{kn} - \delta_{jn}\delta_{km}. \tag{4.19}$$

The first derivatives of the curl are constants, hence its variation is zero:

$$\frac{\partial g_p}{\partial n_k} = 0, \quad \frac{\partial g_p}{\partial n_{i,j}} = \varepsilon_{pji}, \quad \frac{d}{dx_j}\frac{\partial g_p}{\partial n_{i,j}} = 0, \quad \Rightarrow \quad \delta \int_V (\nabla \times \mathbf{n})\, d\mathbf{x} = 0. \tag{4.20}$$

However, the variation of the square of the curl does not vanish:

$$\frac{dg_p}{dx_j} = \frac{\partial g_p}{\partial n_{i,k}} n_{i,kj} = \varepsilon_{pkl} n_{l,kj}, \tag{4.21}$$

$$\begin{aligned} \delta_i \int_V (\nabla \times \mathbf{n})^2\, d\mathbf{x} = -2\frac{dg_p}{dx_j}\frac{\partial g_p}{\partial n_{i,j}} &= -2\varepsilon_{pkl} n_{l,kj}\varepsilon_{pji} \\ &= -2(\delta_{kj}\delta_{li} - \delta_{ki}\delta_{lj}) n_{l,kj} = -2(n_{i,kk} - n_{j,ij}). \end{aligned} \tag{4.22}$$

Thus, the vector form of the variation is:

$$\delta \int_V (\nabla \times \mathbf{n})^2\, d\mathbf{x} = -2(\Delta \mathbf{n} - \nabla(\nabla \cdot \mathbf{n})). \tag{4.23}$$

This expression shows how the energy of the system changes with respect to variations in the field $\mathbf{n}$.

(III) Let $g = \mathbf{n} \cdot (\nabla \times \mathbf{n})$ or in coordinate form:

$$g = n_p \varepsilon_{plm} n_{m,l}. \tag{4.24}$$

This time we are dealing with a quadratic form g of $\mathbf{n}$, hence the partial derivatives

do not vanish:

$$\frac{\partial g}{\partial n_i} = \varepsilon_{ilm} n_{m,l}, \quad \frac{\partial g}{\partial n_{i,j}} = n_p \varepsilon_{pji}, \quad \frac{d}{dx_j}\frac{\partial g}{\partial n_{i,j}} = n_{p,j}\varepsilon_{pji}. \tag{4.25}$$

Thus, the variation of g itself represents the following linear transformation of $\mathbf{n}$:

$$\begin{aligned}\delta_i \int_V (\mathbf{n}\cdot(\nabla\times\mathbf{n}))\,d\mathbf{x} = \frac{\partial g}{\partial n_i} - \frac{\partial}{\partial x_j}\frac{\partial g}{\partial n_{i,j}} &= \varepsilon_{ilm} n_{m,l} - n_{p,j}\varepsilon_{pji} \\ &= \varepsilon_{ilm} n_{m,l} - n_{m,l}\varepsilon_{mli} = 2\varepsilon_{ilm} n_{m,l},\end{aligned} \tag{4.26}$$

or in vector notation:

$$\delta \int_V (\mathbf{n}\cdot(\nabla\times\mathbf{n}))\,d\mathbf{x} = 2(\nabla\times\mathbf{n}). \tag{4.27}$$

Now we can derive the variation of the square of g. Using the expression

$$\delta_i \int_V (\mathbf{n}\cdot(\nabla\times\mathbf{n}))^2\,d\mathbf{x} = 2g\,\delta_i \int_V g\,d\mathbf{x} - 2\frac{dg}{dx_j}\frac{\partial g}{\partial n_{i,j}}, \tag{4.28}$$

and applying the derived relationship, the second term can be rewritten as:

$$\frac{dg}{dx_j}\frac{\partial g}{\partial n_{i,j}} = g_{,j} n_p \varepsilon_{pji} = (\mathbf{n}\times\nabla g)_i. \tag{4.29}$$

Thus, we get:

$$\delta \int_V (\mathbf{n}\cdot(\nabla\times\mathbf{n}))^2\,d\mathbf{x} = 4(\mathbf{n}\cdot(\nabla\times\mathbf{n}))(\nabla\times\mathbf{n}) - 2\mathbf{n}\times\nabla(\mathbf{n}\cdot(\nabla\times\mathbf{n})). \tag{4.30}$$

(IV) Let $f = qg$, where $g = \mathbf{n}\cdot(\nabla\times\mathbf{n})$ and q is a function depending only on $\mathbf{x}$. Then the partial derivatives of f are expressed as follows:

$$\frac{\partial f}{\partial n_i} = q\frac{\partial g}{\partial n_i}, \quad \frac{\partial f}{\partial n_{i,j}} = q\frac{\partial g}{\partial n_{i,j}}, \quad \frac{d}{dx_j}\frac{\partial f}{\partial n_{i,j}} = \frac{\partial q}{\partial x_j}\frac{\partial g}{\partial n_{i,j}} + q\frac{d}{dx_j}\frac{\partial g}{\partial n_{i,j}}. \tag{4.31}$$

Therefore, the variation of f is expressed as:

$$\delta_i \int_V f \, d\mathbf{x} = \frac{\partial f}{\partial n_i} - \sum_j \frac{\partial}{\partial x_j} \frac{\partial f}{\partial n_{i,j}} = q\delta_i \int_V g \, d\mathbf{x} - \frac{\partial q}{\partial x_j} \frac{\partial g}{\partial n_{i,j}}. \tag{4.32}$$

Using

$$\frac{\partial g}{\partial n_{i,j}} = n_p \varepsilon_{pji} \quad \Rightarrow \quad \frac{\partial q}{\partial x_j} \frac{\partial g}{\partial n_{i,j}} = \frac{\partial q}{\partial x_j} n_p \varepsilon_{pji} = (\mathbf{n} \times \nabla q)_i, \tag{4.33}$$

we have:

$$\delta \int_V q(\mathbf{n} \cdot (\nabla \times \mathbf{n})) \, d\mathbf{x} = q\delta \int_V (\mathbf{n} \cdot (\nabla \times \mathbf{n})) \, d\mathbf{x} - \mathbf{n} \times \nabla q = 2q(\nabla \times \mathbf{n}) - \mathbf{n} \times \nabla q. \tag{4.34}$$

Finally, for the complete variation of energy, we obtain:

$$\begin{aligned} \delta E = &-K_1 \Delta \mathbf{n} - (K_3 - K_1)[\Delta \mathbf{n} - \nabla(\nabla \cdot \mathbf{n})] + \\ &+ (K_2 - K_3)[2(\mathbf{n} \cdot (\nabla \times \mathbf{n}))(\nabla \times \mathbf{n}) - \mathbf{n} \times \nabla(\mathbf{n} \cdot (\nabla \times \mathbf{n}))] + \\ &+ K_2[2q(\nabla \times \mathbf{n}) - \mathbf{n} \times \nabla q] = -K_1 \nabla(\nabla \cdot \mathbf{n}) - K_3[\Delta \mathbf{n} - \nabla(\nabla \cdot \mathbf{n})] + \\ &+ (K_2 - K_3)[2(\mathbf{n} \cdot (\nabla \times \mathbf{n}))(\nabla \times \mathbf{n}) - \mathbf{n} \times \nabla(\mathbf{n} \cdot (\nabla \times \mathbf{n}))] + \\ &+ K_2[2q(\nabla \times \mathbf{n}) - \mathbf{n} \times \nabla q]. \end{aligned} \tag{4.35}$$

For numerical calculations, we use a discrete square lattice with energy, including summation over all nodes:

$$\begin{aligned} E = \frac{1}{2} \sum_{i,j,k} C^{\{ijk\}} \Big[&K_1 (\nabla \mathbf{n}^{\{ijk\}})^2 + (K_3 - K_1)(\nabla \times \mathbf{n}^{\{ijk\}})^2 + \\ &+ (K_2 - K_3)(\mathbf{n}^{\{ijk\}} \cdot (\nabla \times \mathbf{n}^{\{ijk\}}))^2 + \\ &+ 2K_2 q_0 (\mathbf{n}^{\{ijk\}} \cdot (\nabla \times \mathbf{n}^{\{ijk\}})) - \Delta\chi (\mathbf{n}^{\{ijk\}} \cdot \mathbf{H}^{\{ijk\}})^2 \Big]. \end{aligned} \tag{4.36}$$

Indices $\{ijk\}$ correspond to the positions of the cells along the x, y, z axes, respectively. For the introduction of differential operations, we use local indexing within

each cube $\{ijk\}$ (see Figure 4.5).

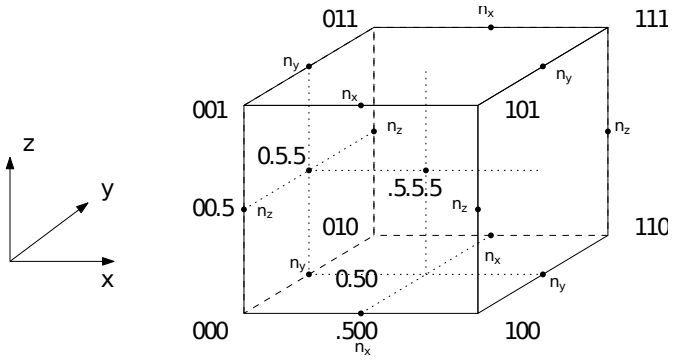

Figure 4.5. Local indexing

To simplify numerical calculations, the following indexing is introduced:

$$n_x^{i+\frac{1}{2},j,k} = n_x^{\{ijk\}}, \quad n_y^{i,j+\frac{1}{2},k} = n_y^{\{ijk\}}, \quad n_z^{i,j,k+\frac{1}{2}} = n_z^{\{ijk\}}, \tag{4.37}$$

$$n_x^{\frac{1}{2},\frac{1}{2},0} = \left[n_x^{0,0,0} + n_x^{0,1,0} + n_x^{0,0,1} + n_x^{0,1,1} + n_x^{1,0,0} + n_x^{1,1,0} + n_x^{1,0,1} + n_x^{1,1,1}\right]/8, \tag{4.38}$$

and notation:

$$\partial_y^{\frac{1}{2},\frac{1}{2},0} n_z = n_z^{0,1,\frac{1}{2}} - n_z^{0,0,\frac{1}{2}}, \tag{4.39}$$

with the remaining components determined by similar transformations.

The volume of the system is defined as:

$$V = [0, l_x N_x] \times [0, l_y N_y] \times [0, l_z N_z]. \tag{4.40}$$

Consider the question of the error associated with placing the **n** grids at different points for each energy component.

If we replace the integral over the variable x with the corresponding finite sum with coefficients corresponding to the trapezoidal method, we get:

$$\int_0^{l_x N_x} f(x)\,dx = \sum_{i=0}^{N_x} C_t^i f(i l_x) l_x + O(l_x^2),$$

$$l_x \to 0, \quad l_x N_x = L_x = \text{const},$$

$$C_t^0 = C_t^{N_x} = \frac{1}{2}, \quad C_t^j = 1 \text{ for } j \neq 0, N_x. \quad (4.41)$$

Similarly for the rectangle method:

$$\int_0^{l_x N_x} f(x)\,dx = \sum_{i=0}^{N_x - 1} C_r^i f\left(\left(i + \frac{1}{2}\right) l_x\right) l_x + O(l_x), \quad C_r^i = 1. \quad (4.42)$$

Repeating the procedure for integration over three-dimensional space:

$$\iiint_V f(x,y,z)\,dx\,dy\,dz = \sum_{i=0}^{N_x}\sum_{j=0}^{N_y}\sum_{k=0}^{N_z} f(i l_x, j l_y, k l_z) C_t^i C_t^j C_t^k l_x l_y l_z +$$

$$+ O(l_x^2) + O(l_y^2) + O(l_z^2). \quad (4.43)$$

Thus, the error of this replacement does not exceed the square of the partition along each axis. We check that the differentiation operations do not worsen the approximation accuracy:

$$(\partial_x n_x)^{i,j,k} = \frac{n_x^{i+0.5,j,k} - n_x^{i-0.5,j,k}}{l_x} + O(l_x^2), \quad (4.44)$$

$$\iiint_V (\partial_x n_x)^2 \, dx \, dy \, dz = \\ = \sum_{i=0}^{N_x} \sum_{j=0}^{N_y} \sum_{k=0}^{N_z} l_x^{-2} (n_x^{i+0.5,j,k} - n_x^{i-0.5,j,k})^2 C_t^i C_t^j C_t^k l_x l_y l_z + \\ + O(l_x^2) + O(l_y^2) + O(l_z^2). \quad (4.45)$$

It can be shown that such an order of error is maintained for all similar replacements. This procedure was applied to all energy components.

The contribution $(\nabla \mathbf{n})^2$ can be represented as a sum:

$$\int_V (\nabla \mathbf{n})^2 \, dV = \sum_{i=0}^{N_x} \sum_{j=0}^{N_y} \sum_{k=0}^{N_z} C_t^i C_t^j C_t^k \left[(\partial_x n_x)^2 + (\partial_y n_y)^2 + (\partial_z n_z)^2 \right]^{ijk} l_x l_y l_z + \\ + \sum_{i=0}^{N_x-1} \sum_{j=0}^{N_y-1} \sum_{k=0}^{N_z} C_r^i C_r^j C_t^k \left[(\partial_x n_y)^2 + (\partial_y n_x)^2 \right]^{i+\frac{1}{2},j+\frac{1}{2},k} l_x l_y l_z + \\ + \sum_{i=0}^{N_x-1} \sum_{j=0}^{N_y} \sum_{k=0}^{N_z-1} C_r^i C_t^j C_r^k \left[(\partial_x n_z)^2 + (\partial_z n_x)^2 \right]^{i+\frac{1}{2},j,k+\frac{1}{2}} l_x l_y l_z + \\ + \sum_{i=0}^{N_x} \sum_{j=0}^{N_y-1} \sum_{k=0}^{N_z-1} C_t^i C_r^j C_r^k \left[(\partial_y n_z)^2 + (\partial_z n_y)^2 \right]^{i,j+\frac{1}{2},k+\frac{1}{2}} l_x l_y l_z. \quad (4.46)$$

The operation $\mathbf{n} \cdot (\nabla \times \mathbf{n})$ for each lattice cell is expressed as:

$$\mathbf{n} \cdot (\nabla \times \mathbf{n}) = n_x \left(\partial_y n_z - \partial_z n_y \right) + \\ n_y \left(\partial_z n_x - \partial_x n_z \right) + n_z \left(\partial_x n_y - \partial_y n_x \right). \quad (4.47)$$

Thus, the contribution to the energy containing $\mathbf{n} \cdot (\nabla \times \mathbf{n})$ is represented as

a sum:

$$\int_V \mathbf{n}\cdot(\nabla\times\mathbf{n})\,dV = \sum_{i=0}^{N_x}\sum_{j=0}^{N_y}\sum_{k=0}^{N_z}\left[\mathbf{n}\cdot(\nabla\times\mathbf{n})\right]^{ijk} C_t^i C_t^j C_t^k l_x l_y l_z. \tag{4.48}$$

The contribution to the energy proportional to $(\mathbf{n}\cdot\mathbf{H})^2$ can be expressed as follows:

$$\int_V (\mathbf{n}\cdot\mathbf{H})^2\,dV = \sum_{i=0}^{N_x}\sum_{j=0}^{N_y}\sum_{k=0}^{N_z}\left[(\mathbf{n}\cdot\mathbf{H})^2\right]^{ijk} C_t^i C_t^j C_t^k l_x l_y l_z. \tag{4.49}$$

Calculating the Energy Variation

In the lattice model, the gradient with respect to $\mathbf{n}$ is analogous to the energy variation in the continuous model. To derive the corresponding expression, we calculate the gradient of each component of energy in the lattice model in the direction of $\mathbf{n}$.

(VI.1) Consider the gradient of the component $(\nabla\mathbf{n})^2$ at the lattice node $\{ijk\}$:

$$\begin{aligned}\partial_{\mathbf{n}^{\{ijk\}}}\Bigg[\sum_{j=0}^{N_y}\sum_{k=0}^{N_z} C_t^i C_t^j C_t^k\Big[&(n_x^{\{ijk\}}-n_x^{\{i-1jk\}})^2+(n_y^{\{ijk\}}-n_y^{\{ij-1k\}})^2+\\ &+(n_z^{\{ijk\}}-n_z^{\{ijk-1\}})^2\Big]\Bigg]=\\ =2\begin{bmatrix} C_t^i C_t^j C_t^k(n_x^{\{ijk\}}-n_x^{\{i-1jk\}}) - C_r^{i+1} C_r^j C_t^k(n_x^{\{i+1jk\}}-n_x^{\{ijk\}})\\ C_t^i C_t^j C_t^k(n_y^{\{ijk\}}-n_y^{\{ij-1k\}}) - C_r^i C_r^{j+1} C_t^k(n_y^{\{ij+1k\}}-n_y^{\{ijk\}})\\ C_t^i C_t^j C_t^k(n_z^{\{ijk\}}-n_z^{\{ijk-1\}}) - C_r^i C_r^j C_t^{k+1}(n_z^{\{ijk+1\}}-n_z^{\{ijk\}})\end{bmatrix},\end{aligned} \tag{4.50}$$

$$\partial_{\mathbf{n}^{\{ijk\}}}\left[\sum_{i=0}^{N_x-1}\sum_{j=0}^{N_y-1}\sum_{k=0}^{N_z} C_r^i C_r^j C_t^k\left[(n_y^{\{i+1jk\}}-n_y^{\{ijk\}})^2+(n_x^{\{ij+1k\}}-n_x^{\{ijk\}})^2\right]\right]=$$

$$=2\begin{bmatrix} C_r^i C_r^{j-1} C_t^k(n_x^{\{ijk\}}-n_x^{\{ij-1k\}})-C_r^i C_r^j C_t^k(n_x^{\{ij+1k\}}-n_x^{\{ijk\}}) \\ C_r^{i-1} C_r^j C_t^k(n_y^{\{ijk\}}-n_y^{\{i-1jk\}})-C_r^i C_r^j C_t^k(n_y^{\{i+1jk\}}-n_y^{\{ijk\}}) \\ 0 \end{bmatrix}, \quad (4.51)$$

$$\partial_{\mathbf{n}^{\{ijk\}}}\left[\sum_{i=0}^{N_x-1}\sum_{j=0}^{N_y}\sum_{k=0}^{N_z-1} C_r^i C_t^j C_r^k\left[(n_z^{\{i+1jk\}}-n_z^{\{ijk\}})^2+(n_x^{\{ijk+1\}}-n_x^{\{ijk\}})^2\right]\right]=$$

$$=2\begin{bmatrix} C_r^i C_t^j C_r^{k-1}(n_x^{\{ijk\}}-n_x^{\{ijk-1\}})-C_r^i C_t^j C_r^k(n_x^{\{ijk+1\}}-n_x^{\{ijk\}}) \\ 0 \\ C_r^{i-1} C_t^j C_r^k(n_z^{\{ijk\}}-n_z^{\{i-1jk\}})-C_r^i C_t^j C_r^k(n_z^{\{i+1jk\}}-n_z^{\{ijk\}}) \end{bmatrix}, \quad (4.52)$$

$$\partial_{\mathbf{n}^{\{ijk\}}}\left[\sum_{i=0}^{N_x}\sum_{j=0}^{N_y-1}\sum_{k=0}^{N_z-1} C_t^i C_r^j C_r^k[(n_z^{\{ij+1k\}}-n_z^{\{ijk\}})^2+(n_y^{\{ijk+1k\}}-n_y^{\{ijk\}})^2]\right]=$$

$$=2\begin{bmatrix} 0 \\ C_t^i C_r^j C_r^{k-1}(n_y^{\{ijk\}}-n_y^{\{ijk-1\}})-C_t^i C_r^j C_r^k(n_y^{\{ijk+1\}}-n_y^{\{ijk\}}) \\ C_t^i C_r^{j-1} C_r^k(n_z^{\{ijk\}}-n_z^{\{ij-1k\}})-C_t^i C_r^j C_r^k(n_z^{\{ij+1k\}}-n_z^{\{ijk\}}) \end{bmatrix}. \quad (4.53)$$

(VI.2) Consider the gradient of each component $(\nabla\times\mathbf{n})^2$ at the lattice node $\{ijk\}$:

$$\partial_{\mathbf{n}^{\{ijk\}}}\left[\sum_{i=0}^{N_x}\sum_{j=0}^{N_y-1}\sum_{k=0}^{N_z-1}C_t^iC_r^jC_r^k\left[(n_z^{\{ij+1k\}}-n_z^{\{ijk\}})-(n_y^{\{ijk+1\}}-n_y^{\{ijk\}})\right]^2\right]=$$

$$=2\begin{bmatrix}0\\D_{1,ijk}-D_{1,ijk-1}\\-D_{1,ijk}+D_{1,ij-1k}\end{bmatrix}, \quad (4.54)$$

$$\partial_{\mathbf{n}^{\{ijk\}}}\left[\sum_{i=0}^{N_x-1}\sum_{j=0}^{N_y}\sum_{k=0}^{N_z-1}C_r^iC_t^jC_r^k\left[(n_x^{\{ijk+1\}}-n_x^{\{ijk\}})-(n_z^{\{i+1jk\}}-n_z^{\{ijk\}})\right]^2\right]=$$

$$=2\begin{bmatrix}-D_{2,ijk}+D_{2,ijk-1}\\0\\D_{2,ijk}+D_{2,i-1jk}\end{bmatrix}, \quad (4.55)$$

$$\partial_{\mathbf{n}^{\{ijk\}}}\left[\sum_{i=0}^{N_x-1}\sum_{j=0}^{N_y-1}\sum_{k=0}^{N_z}C_r^iC_r^jC_t^k\left[(n_y^{\{i+1jk\}}-n_y^{\{ijk\}})-(n_x^{\{ij+1k\}}-n_x^{\{ijk\}})\right]^2\right]=$$

$$=2\begin{bmatrix}D_{3,ijk}-D_{3,ij-1k}\\-D_{3,ijk}+D_{3,i-1jk}\\0\end{bmatrix}, \quad (4.56)$$

$$\partial_{\mathbf{n}^{\{ijk\}}}\left[\sum_{i=0}^{N_x-1}\sum_{j=0}^{N_y}\sum_{k=0}^{N_z-1} C_r^i C_t^j C_r^k \left[(n_x^{\{ijk+1\}}-n_x^{\{ijk\}})-(n_z^{\{i+1jk\}}-n_z^{\{ijk\}})\right]^2\right]= \\ = 2\begin{bmatrix} -D_{4,ijk}+D_{4,ijk-1} \\ 0 \\ D_{4,ijk}+D_{4,i-1jk}\end{bmatrix}, \quad (4.57)$$

where:

$$D_{1,ijk} = C_t^i C_r^j C_r^k \left[(n_z^{\{ij+1k\}}-n_z^{\{ijk\}})-(n_y^{\{ijk+1\}}-n_y^{\{ijk\}})\right],$$
$$D_{1,ijk-1} = C_t^i C_r^j C_r^{k-1} \left[(n_z^{\{ij+1k-1\}}-n_z^{\{ijk-1\}})-(n_y^{\{ijk\}}-n_y^{\{ijk-1\}})\right],$$
$$D_{1,ij-1k} = C_t^i C_r^{j-1} C_r^k \left[(n_z^{\{ijk\}}-n_z^{\{ij-1k\}})-(n_y^{\{ij-1k+1\}}-n_y^{\{ij-1k\}})\right],$$
$$D_{2,ijk} = C_r^i C_t^j C_r^k \left[(n_x^{\{ijk+1\}}-n_x^{\{ijk\}})-(n_z^{\{i+1jk\}}-n_z^{\{ijk\}})\right],$$
$$D_{2,ijk-1} = C_r^i C_t^j C_r^{k-1} \left[(n_x^{\{ijk\}}-n_x^{\{ijk-1\}})-(n_z^{\{i+1jk-1\}}-n_z^{\{ijk-1\}})\right],$$
$$D_{2,i-1jk} = C_r^{i-1} C_t^j C_r^k \left[(n_x^{\{i-1jk+1\}}-n_x^{\{i-1jk\}})-(n_z^{\{ijk\}}-n_z^{\{i-1jk\}})\right],$$
$$D_{3,ijk} = C_r^i C_r^j C_t^k \left[(n_y^{\{i+1jk\}}-n_y^{\{ijk\}})-(n_x^{\{ij+1k\}}-n_x^{\{ijk\}})\right],$$
$$D_{3,ij-1k} = C_r^i C_r^{j-1} C_t^k \left[(n_y^{\{i+1j-1k\}}-n_y^{\{ij-1k\}})-(n_x^{\{ijk\}}-n_x^{\{ij-1k\}})\right],$$
$$D_{3,i-1jk} = C_r^{i-1} C_r^j C_t^k \left[(n_y^{\{ijk\}}-n_y^{\{i-1jk\}})-(n_x^{\{i-1j+1k\}}-n_x^{\{i-1jk\}})\right],$$
$$D_{4,ijk} = D_{2,ijk}, \quad D_{4,ijk-1} = D_{2,ijk-1}, \quad D_{4,i-1jk} = D_{2,i-1jk}.$$

(VI.3) Consider each of the gradient components of $\mathbf{n}\cdot(\nabla\times\mathbf{n})$ at the lattice node $\{ijk\}$:

$$\partial_{n_x^{\{ijk\}}}\Bigg[\frac{1}{8}\sum_{i=0}^{N_x}\sum_{j=0}^{N_y-1}\sum_{k=0}^{N_z-1}C_t^iC_r^jC_r^k\Big[n_x^{\{ijk\}}+n_x^{\{ij+1k\}}+n_x^{\{ijk+1\}}+n_x^{\{ij+1k+1\}}+$$
$$+n_x^{\{i-1jk\}}+n_x^{\{i-1j+1k\}}+n_x^{\{i-1jk+1\}}+n_x^{\{i-1j+1k+1\}}\Big]$$
$$\Big[(n_z^{\{ij+1k\}}-n_z^{\{ijk\}})-(n_y^{\{ijk+1\}}-n_y^{\{ijk\}})\Big]\Bigg]=$$
$$=\frac{1}{8}\Bigg[C_t^iC_r^jC_r^k\Big[(n_z^{\{ij+1k\}}-n_z^{\{ijk\}})-(n_y^{\{ijk+1\}}-n_y^{\{ijk\}})\Big]+$$
$$+C_t^iC_r^{j-1}C_r^k\Big[(n_z^{\{ijk\}}-n_z^{\{ij-1k\}})-(n_y^{\{ij-1k+1\}}-n_y^{\{ij-1k\}})\Big]+$$
$$+C_t^iC_r^jC_r^{k-1}\Big[(n_z^{\{ij+1k-1\}}-n_z^{\{ijk-1\}})-(n_y^{\{ijk\}}-n_y^{\{ijk-1\}})\Big]+$$
$$+C_t^iC_r^{j-1}C_r^{k-1}\Big[(n_z^{\{ijk-1\}}-n_z^{\{ij-1k-1\}})-(n_y^{\{ij-1k\}}-n_y^{\{ij-1k-1\}})\Big]+$$
$$+C_t^{i+1}C_r^jC_r^k\Big[(n_z^{\{i+1j+1k\}}-n_z^{\{i+1jk\}})-(n_y^{\{i+1jk+1\}}-n_y^{\{i+1jk\}})\Big]+$$
$$+C_t^{i+1}C_r^{j-1}C_r^k\Big[(n_z^{\{i+1jk\}}-n_z^{\{i+1j-1k\}})-(n_y^{\{i+1j-1k+1\}}-n_y^{\{i+1j-1k\}})\Big]+$$
$$+C_t^{i+1}C_r^jC_r^{k-1}\Big[(n_z^{\{i+1j+1k-1\}}-n_z^{\{i+1jk-1\}})-(n_y^{\{i+1jk\}}-n_y^{\{i+1jk-1\}})\Big]+$$
$$+C_t^{i+1}C_r^{j-1}C_r^{k-1}\Big[(n_z^{\{i+1jk-1\}}-n_z^{\{i+1j-1k-1\}})-(n_y^{\{i+1j-1k\}}-n_y^{\{i+1j-1k-1\}})\Big]\Bigg],\tag{4.58}$$

$$\partial_{n_y^{\{ijk\}}}\Bigg[\frac{1}{8}\sum_{i=0}^{N_x}\sum_{j=0}^{N_y-1}\sum_{k=0}^{N_z-1}C_t^iC_r^jC_r^k\Big[n_x^{\{ijk\}}+n_x^{\{ij+1k\}}+n_x^{\{ijk+1\}}+n_x^{\{ij+1k+1\}}+$$
$$+n_x^{\{i-1jk\}}+n_x^{\{i-1j+1k\}}+n_x^{\{i-1jk+1\}}+n_x^{\{i-1j+1k+1\}}\Big]$$
$$\Big[(n_z^{\{ij+1k\}}-n_z^{\{ijk\}})-(n_y^{\{ijk+1\}}-n_y^{\{ijk\}})\Big]\Bigg]=$$
$$=-\frac{1}{8}\Bigg[C_t^iC_r^jC_r^{k-1}\big[n_x^{\{ijk-1\}}+n_x^{\{ij+1k-1\}}+n_x^{\{ijk\}}+n_x^{\{ij+1k\}}+$$
$$n_x^{\{i-1jk-1\}}+n_x^{\{i-1j+1k-1\}}+n_x^{\{i-1jk\}}+n_x^{\{i-1j+1k\}}\big]-$$
$$-C_t^iC_r^jC_r^k\big[n_x^{\{ijk\}}+n_x^{\{ij+1k\}}+n_x^{\{ijk+1\}}+n_x^{\{ij+1k+1\}}+$$
$$n_x^{\{i-1jk\}}+n_x^{\{i-1j+1k\}}+n_x^{\{i-1jk+1\}}+n_x^{\{i-1j+1k+1\}}\big]\Bigg],\quad(4.59)$$

$$\partial_{n_z^{\{ijk\}}}\Bigg[\frac{1}{8}\sum_{i=0}^{N_x}\sum_{j=0}^{N_y-1}\sum_{k=0}^{N_z-1}C_t^iC_r^jC_r^k\Big[n_x^{\{ijk\}}+n_x^{\{ij+1k\}}+n_x^{\{ijk+1\}}+n_x^{\{ij+1k+1\}}+$$
$$+n_x^{\{i-1jk\}}+n_x^{\{i-1j+1k\}}+n_x^{\{i-1jk+1\}}+n_x^{\{i-1j+1k+1\}}\Big]$$
$$\Big[(n_z^{\{ij+1k\}}-n_z^{\{ijk\}})-(n_y^{\{ijk+1\}}-n_y^{\{ijk\}})\Big]\Bigg]=$$
$$=\frac{1}{8}\Bigg[C_t^iC_r^{j-1}C_r^k\Big[n_x^{\{ij-1k\}}+n_x^{\{ijk\}}+n_x^{\{ij-1k+1\}}+n_x^{\{ijk+1\}}+$$
$$n_x^{\{i-1j-1k\}}+n_x^{\{i-1j-1k\}}+n_x^{\{i-1j-1k+1\}}+n_x^{\{i-1jk+1\}}\Big]-$$
$$-C_t^iC_r^jC_r^k\Big[n_x^{\{ijk\}}+n_x^{\{ij+1k\}}+n_x^{\{ijk+1\}}+n_x^{\{ij+1k+1\}}+$$
$$n_x^{\{i-1jk\}}+n_x^{\{i-1j+1k\}}+n_x^{\{i-1jk+1\}}+n_x^{\{i-1j+1k+1\}}\Big]\Bigg],\quad(4.60)$$

$$\partial_{n_x^{\{ijk\}}}\Bigg[\frac{1}{8}\sum_{i=0}^{N_x-1}\sum_{j=0}^{N_y}\sum_{k=0}^{N_z-1}C_r^iC_t^jC_r^k\Big[n_y^{\{ijk\}}+n_y^{\{i+1jk\}}+n_y^{\{ijk+1\}}+n_y^{\{i+1jk+1\}}+$$
$$+n_y^{\{ij-1k\}}+n_y^{\{i+1j-1k\}}+n_y^{\{ij-1k+1\}}+n_y^{\{i+1j-1k+1\}}\Big]$$
$$\Big[(n_x^{\{ijk+1\}}-n_x^{\{ijk\}})-(n_z^{\{i+1jk\}})-n_z^{\{ijk\}})\Big]\Bigg]=$$
$$=\frac{1}{8}\Bigg[C_r^iC_t^jC_r^{k-1}\big[n_y^{\{ijk-1\}}+n_y^{\{i+1jk-1\}}+n_y^{\{ijk\}}+n_y^{\{i+1jk\}}+$$
$$n_y^{\{ij-1k-1\}}+n_y^{\{i+1j-1k-1\}}+n_y^{\{ij-1k\}}+n_y^{\{i+1j-1k\}}\big]-$$
$$-C_r^iC_t^jC_r^k\big[n_y^{\{ijk\}}+n_y^{\{i+1jk\}}+n_y^{\{ijk+1\}}+n_y^{\{i+1jk+1\}}+$$
$$n_y^{\{ij-1k\}}+n_y^{\{i+1j-1k\}}+n_y^{\{ij-1k+1\}}+n_y^{\{i+1j-1k+1\}}\big]\Bigg],\quad(4.61)$$

$$\partial_{n_y^{\{ijk\}}}\Bigg[\frac{1}{8}\sum_{i=0}^{N_x-1}\sum_{j=0}^{N_y}\sum_{k=0}^{N_z-1}C_r^iC_t^jC_r^k\Big[n_y^{\{ijk\}}+n_y^{\{i+1jk\}}+n_y^{\{ijk+1\}}+n_y^{\{i+1jk+1\}}+$$
$$+n_y^{\{ij-1k\}}+n_y^{\{i+1j-1k\}}+n_y^{\{ij-1k+1\}}+n_y^{\{i+1j-1k+1\}}\Big]$$
$$\Big[(n_x^{\{ijk+1\}}-n_x^{\{ijk\}})-(n_z^{\{i+1jk\}})-n_z^{\{ijk\}})\Big]\Bigg]=$$
$$=\frac{1}{8}\Bigg[C_r^iC_t^jC_r^k\Big[(n_x^{\{ijk+1\}}-n_x^{\{ijk\}})-(n_z^{\{i+1jk\}})-n_z^{\{ijk\}})\Big]+$$
$$+C_r^{i-1}C_t^jC_r^k\Big[(n_x^{\{i-1jk+1\}}-n_x^{\{i-1jk\}})-(n_z^{\{ijk\}})-n_z^{\{i-1jk\}})\Big]+$$
$$+C_r^iC_t^jC_r^{k-1}\Big[(n_x^{\{ijk\}}-n_x^{\{ijk-1\}})-(n_z^{\{i+1jk-1\}})-n_z^{\{ijk-1\}})\Big]+$$
$$+C_r^{i-1}C_t^jC_r^{k-1}\Big[(n_x^{\{i-1jk\}}-n_x^{\{i-1jk-1\}})-(n_z^{\{ijk-1\}})-n_z^{\{i-1jk-1\}})\Big]+$$
$$+C_r^iC_t^{j+1}C_r^k\Big[(n_x^{\{ij+1k+1\}}-n_x^{\{ij+1k\}})-(n_z^{\{i+1j+1k\}})-n_z^{\{ij+1k\}})\Big]+$$
$$+C_r^{i-1}C_t^{j+1}C_r^k\Big[(n_x^{\{i-1j+1k+1\}}-n_x^{\{i-1j+1k\}})-(n_z^{\{ij+1k\}})-n_z^{\{i-1j+1k\}})\Big]+$$
$$+C_r^iC_t^{j+1}C_r^{k-1}\Big[(n_x^{\{ij+1k-1\}}-n_x^{\{ij+1k-1\}})-(n_z^{\{i+1j+1k-1\}})-n_z^{\{ij+1k-1\}})\Big]+$$
$$+C_r^{i-1}C_t^{j+1}C_r^{k-1}\Big[(n_x^{\{i-1j+1k\}}-n_x^{\{i-1j+1k-1\}})-(n_z^{\{ij+1k-1\}}-n_z^{\{i-1j+1k-1\}})\Big]\Bigg],\tag{4.62}$$

$$\partial_{n_z^{\{ijk\}}}\Bigg[\frac{1}{8}\sum_{i=0}^{N_x-1}\sum_{j=0}^{N_y}\sum_{k=0}^{N_z-1}C_r^iC_t^jC_r^k\Big[n_y^{\{ijk\}}+n_y^{\{i+1jk\}}+n_y^{\{ijk+1\}}+n_y^{\{i+1jk+1\}}+$$
$$+n_y^{\{ij-1k\}}+n_y^{\{i+1j-1k\}}+n_y^{\{ij-1k+1\}}+n_y^{\{i+1j-1k+1\}}\Big]$$
$$\Big[(n_x^{\{ijk+1\}}-n_x^{\{ijk\}})-(n_z^{\{i+1jk\}})-n_z^{\{ijk\}})\Big]\Bigg]=$$
$$=-\frac{1}{8}\Bigg[C_r^{i-1}C_t^jC_r^k\big[n_y^{\{i-1jk\}}+n_y^{\{ijk\}}+n_y^{\{i-1jk+1\}}+n_y^{\{ijk+1\}}+$$
$$+n_y^{\{i-1j-1k\}}+n_y^{\{ij-1k\}}+n_y^{\{i-1j-1k+1\}}+n_y^{\{ij-1k+1\}}\big]-$$
$$-C_r^iC_t^jC_r^k\big[n_y^{\{ijk\}}+n_y^{\{i+1jk\}}+n_y^{\{ijk+1\}}+n_y^{\{i+1jk+1\}}+$$
$$n_y^{\{ij-1k\}}+n_y^{\{i+1j-1k\}}+n_y^{\{ij-1k+1\}}+n_y^{\{i+1j-1k+1\}}\big]\Bigg],\quad(4.63)$$

$$\partial_{n_x^{\{ijk\}}}\Bigg[\frac{1}{8}\sum_{i=0}^{N_x-1}\sum_{j=0}^{N_y-1}\sum_{k=0}^{N_z}C_r^iC_r^jC_t^k\Big[n_z^{\{ijk\}}+n_z^{\{ij+1k\}}+n_z^{\{i+1jk\}}+n_z^{\{i+1j+1k\}}+$$
$$+n_z^{\{ijk-1\}}+n_z^{\{ij+1k-1\}}+n_z^{\{i+1jk-1\}}+n_z^{\{i+1j+1k-1\}}\Big]$$
$$\Big[(n_y^{\{i+1jk\}}-n_y^{\{ijk\}})-(n_x^{\{ij+1k\}}-n_x^{\{ijk\}})\Big]\Bigg]=$$
$$=-\frac{1}{8}\Bigg[C_r^iC_r^{j-1}C_t^k\Big[n_z^{\{ij-1k\}}+n_z^{\{ijk\}}+n_z^{\{i+1j-1k\}}+n_z^{\{i+1jk\}}+$$
$$n_z^{\{ij-1k-1\}}+n_z^{\{ijk-1\}}+n_z^{\{i+1j-1k-1\}}+n_z^{\{i+1jk-1\}}\Big]-$$
$$-C_r^iC_r^jC_t^k\Big[n_z^{\{ijk\}}+n_z^{\{ij+1k\}}+n_z^{\{i+1jk\}}+n_z^{\{i+1j+1k\}}+$$
$$+n_z^{\{ijk-1\}}+n_z^{\{ij+1k-1\}}+n_z^{\{i+1jk-1\}}+n_z^{\{i+1j+1k-1\}}\Big]\Bigg],\quad(4.64)$$

$$\partial_{n_y^{\{ijk\}}}\Bigg[\frac{1}{8}\sum_{i=0}^{N_x-1}\sum_{j=0}^{N_y-1}\sum_{k=0}^{N_z}C_r^iC_r^jC_t^k\Big[n_z^{\{ijk\}}+n_z^{\{ij+1k\}}+n_z^{\{i+1jk\}}+n_z^{\{i+1j+1k\}}+$$
$$+n_z^{\{ijk-1\}}+n_z^{\{ij+1k-1\}}+n_z^{\{i+1jk-1\}}+n_z^{\{i+1j+1k-1\}}\Big]$$
$$\Big[(n_y^{\{i+1jk\}}-n_y^{\{ijk\}})-(n_x^{\{ij+1k\}}-n_x^{\{ijk\}})\Big]\Bigg]=$$
$$=\frac{1}{8}\Bigg[C_r^{i-1}C_r^jC_t^k\Big[n_z^{\{i-1jk\}}+n_z^{\{i-1j+1k\}}+n_z^{\{ijk\}}+n_z^{\{ij+1k\}}+$$
$$n_z^{\{i-1jk-1\}}+n_z^{\{i-1j+1k-1\}}+n_z^{\{ijk-1\}}+n_z^{\{ij+1k-1\}}\Big]-$$
$$-C_r^iC_r^jC_t^k\big[n_z^{\{ijk\}}+n_z^{\{ij+1k\}}+n_z^{\{i+1jk\}}+n_z^{\{i+1j+1k\}}+$$
$$n_z^{\{ijk-1\}}+n_z^{\{ij+1k-1\}}+n_z^{\{i+1jk-1\}}+n_z^{\{i+1j+1k-1\}}\big]\Bigg],\quad(4.65)$$

$$\partial_{n_z^{\{ijk\}}}\Bigg[\frac{1}{8}\sum_{i=0}^{N_x-1}\sum_{j=0}^{N_y-1}\sum_{k=0}^{N_z}C_r^iC_r^jC_t^k\Big[n_z^{\{ijk\}}+n_z^{\{ij+1k\}}+n_z^{\{i+1jk\}}+n_z^{\{i+1j+1k\}}+$$
$$+n_z^{\{ijk-1\}}+n_z^{\{ij+1k-1\}}+n_z^{\{i+1jk-1\}}+n_z^{\{i+1j+1k-1\}}\Big]$$
$$\Big[(n_y^{\{i+1jk\}}-n_y^{\{ijk\}})-(n_x^{\{ij+1k\}}-n_x^{\{ijk\}})\Big]\Bigg]=$$
$$=\frac{1}{8}\Bigg[C_r^iC_r^jC_t^k\Big[(n_y^{\{i+1jk\}}-n_y^{\{ijk\}})-(n_x^{\{ij+1k\}}-n_x^{\{ijk\}})\Big]+$$
$$+C_r^iC_r^{j-1}C_t^k\Big[(n_y^{\{i+1j-1k\}}-n_y^{\{ij-1k\}})-(n_x^{\{ijk\}}-n_x^{\{ij-1k\}})\Big]+$$
$$+C_r^{i-1}C_r^jC_t^k\Big[(n_y^{\{ijk\}}-n_y^{\{i-1jk\}})-(n_x^{\{i-1j+1k\}}-n_x^{\{i-1jk\}})\Big]+$$
$$+C_r^{i-1}C_r^{j-1}C_t^k\Big[(n_y^{\{ij-1k\}}-n_y^{\{i-1j-1k\}})-(n_x^{\{i-1jk\}}-n_x^{\{i-1j-1k\}})\Big]+$$
$$+C_r^iC_r^jC_t^{k+1}\Big[(n_y^{\{i+1jk+1\}}-n_y^{\{ijk+1\}})-(n_x^{\{ij+1k+1\}}-n_x^{\{ijk+1\}})\Big]+$$
$$+C_r^iC_r^{j-1}C_t^{k+1}\Big[(n_y^{\{i+1j-1k+1\}}-n_y^{\{ij-1k+1\}})-(n_x^{\{ijk+1\}}-n_x^{\{ij-1k+1\}})\Big]+$$
$$+C_r^{i-1}C_r^jC_t^{k+1}\Big[(n_y^{\{ijk+1\}}-n_y^{\{i-1jk+1\}})-(n_x^{\{i-1j+1k+1\}}-n_x^{\{i-1jk+1\}})\Big]+$$
$$+C_r^{i-1}C_r^{j-1}C_t^{k+1}\Big[(n_y^{\{ij-1k+1\}}-n_y^{\{i-1j-1k+1\}})-(n_x^{\{i-1jk+1\}}-n_x^{\{i-1j-1k+1\}})\Big]\Bigg]. \tag{4.66}$$

(VI.4) Consider the gradient $(\mathbf{n}\cdot\mathbf{H})^2$ at the lattice node $\{ijk\}$:

$$\partial_{\mathbf{n}^{\{ijk\}}}\Bigg[\sum_{k=0}^{N_z}C_r^iC_t^jC_t^k\left(n_x^{\{ijk\}}H_x^{\{ijk\}}\right)^2+\sum_{i=0}^{N_x}\sum_{j=0}^{N_y-1}\sum_{k=0}^{N_z}C_t^iC_r^jC_t^k\left(n_y^{\{ijk\}}H_y^{\{ijk\}}\right)^2+$$
$$\sum_{i=0}^{N_x}\sum_{j=0}^{N_y}\sum_{k=0}^{N_z-1}C_t^iC_t^jC_r^k\left(n_z^{\{ijk\}}H_z^{\{ijk\}}\right)^2\Bigg]=2\begin{bmatrix}C_r^iC_t^jC_t^k\left(n_x^{\{ijk\}}H_x^{\{ijk\}}\right)\\C_t^iC_r^jC_t^k\left(n_y^{\{ijk\}}H_y^{\{ijk\}}\right)\\C_t^iC_t^jC_r^k\left(n_z^{\{ijk\}}H_z^{\{ijk\}}\right)\end{bmatrix}. \tag{4.67}$$

After substituting expressions (V.1-V.4) into equation ((4.36)), an expression for the energy of the liquid crystal in the lattice approximation with the displacement

of the director components can be found. Using the same equation and expressions (VI.1-VI.4), an equation for the variation of energy can be obtained.